Industrielle Gemeinschaftsforschung

Schlussbericht vom 04.10.2022

zu IGF-Vorhaben Nr. 250 EN

Thema

Selektives Laserschmelzen von oberflächenbehandelten Pulvern aus Cu-Verbundwerkstoffen

Titel Gesamtprojekt: Product optimisation with New Additive Manufacturing Powders (PONAMP)

Berichtszeitraum

01.09.2019 - 28.02.2022

Forschungsvereinigung

Verein für das Forschungsinstitut für Edelmetalle und Metallchemie e.V. - FEM

Forschungseinrichtung(en)

Forschungsstelle 1 : Forschungsinstitut für Edelmetalle und Metallchemie

Katharinenstraße 17 - 73525 Schwäbisch Gmünd

Forschungsstelle 2 : Fraunhofer-Institut für Umwelt-, Sicherheits-

und Energietechnik UMSICHT - Institutsteil Sulzbach-Rosenberg

An der Maxhütte 1 - 92237 Sulzbach-Rosenberg

Forschungsnetzwerk Mittelstand

Gefördert durch:

Bundesministerium für Wirtschaft und Klimaschutz

aufgrund eines Beschlusses des Deutschen Bundestages

Content

1 Topic of research and summary

The joint research project PONAMP focused on the development of new material qualities for powder bed based *Additive Manufacturing (AM)* techniques. Actual shortcomings in the realization of parts with specific properties, which are a result of the lack of suitable materials compositions and/or of process inherent restrictions, were the target of the project. The goal was to develop new material combinations for parts with high mechanical strength and for specific applications that are not state-of-the-art by the preparation and investigation of specifically modified powder qualities.

AM technologies are one of the main technical routes in realizing production in an “industry 4.0” environment. Manufacturing is done directly from the designed part without the need of preparing supportive tools. AM is extremely flexible in generating complex shapes which are not or difficult to achieve with competing techniques and, it is the most competitive technique for the fabrication of single or low number series of complexly shaped or individually designed parts.

In the metallic sector, powder bed based AM techniques are most advanced and, over the past 5 years, the development of manufacturing machines has been more and more oriented to production. At present, only a limited number of metallic materials are qualified for AM parts manufacturing, concentrating on the most important base areas for applications, such as specific Al, Ti, Ni alloys and steels. Much research is done actually to enlarge the selection of materials for reaching demanded parts properties and for increasing the market volume. However, the specific production characteristics, such as local melting and rapid solidification and cooling, in combination with technical issues, such as laser light absorbance, make it difficult to use well-known alloy compositions for this purpose.

PONAMP investigated and developed material combinations that are suitable to achieve major enhancements in AM parts manufacturing and mechanical/functional parts properties. The technical approach was to combine materials in form of a base (alloy) powder with appropriate thin coatings which are alloyed during the manufacturing step. The new approach was based on the results of the forerunner project OpP3D [36] where promising results had been achieved with coatings on powders in order to improve the laser additive manufacturing of copper and aluminium, which are critical to work with due to low laser absorption and surface oxides, respectively. PONAMP used the knowledge generated in OpP3D by following the specific target to manipulate microstructures for enhanced mechanical and/or functional parts properties. Alloying and rapid cooling during manufacturing are key aspects of this very new and pre-competitive approach. By combining both aspects, the expected outcomes from PONAMP are better manufacturing conditions due to the coating properties (protective, laser absorption) and enhanced parts properties by the targeted manipulation of microstructures through alloying with the coating materials. AM is applied by a fast growing industrial community. Major contributions in the future industrial AM production environment will be provided by SME companies. New materials and manufacturing details generated by PONAMP will drive the development of this fast growing market and supports SME in the German, Belgian and European area.

The project was a co-operation between research institutes from Germany and Belgium that was funded under the framework of CORNET. A user committee from both countries accompanied and supported the project. On the German side, the **fem** Research Institute for Precious Metals + Metals Chemistry and the Fraunhofer **UMSICHT** institute were participating. The Belgium research partners were **SIRRIS**, **Uni Mons** and **Materia Nova**. **fem** had the role of overall project coordinator.

During the course of the project, fem investigated the processability of coated and uncoated Cu alloy powders with *laser beam melting (LBM)* (or *laser powder bed fusion* (*LPBF*)) also by using a quick screening method based on metal sheets instead of powder. Several powders were tested, including commercially available, uncoated CuNiSiCr and CuCrZr powder, coated CuNiSiCr and CuCrZr powder (both with Nb and Cr), and W-coated pure copper powder. Process parameters for an optimal processability with a laser power up to 380 W were developed for all of the above mentioned alloy powders. A coil for an innovative light-weight electric motor (designed by the SME Unicorn Engineering) was built both with the CuNiSiCr and CuCrZr alloy powders as a technology demonstrator.

Fraunhofer UMSICHT investigated and developed methods for the manufacturing of Cu-X composite powders. Three options have been investigated in depth, namely the composite powder manufacturing via suspension spraying (SPS), via mixing/mechanical “alloying” and via a newly implemented two-step atomization process. Prior to these investigations qualification processes for laser melting of single tracks on uncoated and PVD coated Cu, Cu alloy and Al alloy 7070 sheets have been performed in coordination with the project partners for evaluating basic parameter fields and performance characteristics. As a result, tungsten has been selected for the major acitivities in Cu composite powder manufacturing. Moreover, UMSICHT performed pilot melt atomization experiments for powder manufacturing from three different CuNi alloys and from pure Cu for its own activities and the further work at Materia Nova and fem. As a main result, it could be demonstrated that Cu-W composite powders can be manufactured via the mechanical route as well as through the newly established two-step atomization technique. The developed powder qualities enable one to process t dense parts (down to a porosity < 0.4 %) via LPBF at a laser power of 275 W (1064 nm wavelength) with a W content less than 3 vol.-%. This low laser power is clearly above the present state-of-the-art for manufacturing dense Cu parts via the presently used standard LPBF techniques.

The aim of the work at Materia Nova was to produce coatings on metallic powders based on the materials selection in WP1. Firstly, an optimisation of materials was started on flat substrates. A study of plasma parameters was realized to increase the economic profitability of the process. Finally, different metallic depositions were realized on metallic powders. For copper, deposition of Cr, W, Ta, Nb and Mo on the copper alloys Cu, CuCrZr, CuNiSiCr and CuNiAl. For aluminium, deposition of Zr, Ti, B, Mg on the aluminium alloys Al 7075 and Al 7020.

The main research activity of UMONS in the project was the detailed study of the parameters of the magnetron plasma deposition process in order to increase the economic efficiency of the process. The aim was to determine the relationship between the working parameters, the plasma characteristics and the film properties.

The project objective for Sirris was to modify two aluminium alloys: 7075, since it is prone to hot cracking during AM printing and 7020, which is a weldable alloy with low mechanical properties that could benefit from modification. Plates of 7075 and 7020 were coated with 100 nm and 200 nm thickness: Ti and Zr were used for 7075, and Mg and B were used for 7020). These plates were illuminated by the laser with several power levels and several scanning speeds. The aim was to identify and measure the meltpool depth and the presence of eventual cracks. The Al 7075 alloy powder was then coated with Ti and Zr, and the results were remarkable because of the absence of cracks in all processing conditions. The results showed also the extensive grain refinement introduced by the selected elements in the sample.

Sirris conducted also a study on the processability of pure Cu with *electron beam melting (EBM)*, established a parameter window for processing and built a demonstrator (copper winding from an electric motor).

2 Research approach and economic relevance for SMEs

2.1 Targeted Market Sector

PONAMP focuses on the emerging markets for the industrial production of parts by using powder bed based AM technologies with metals. These markets are currently experiencing a huge increase (approx. 30 %/a [1]) due the manifold potentials of manufacturing individually designed and/or complexly shaped parts which cannot be fabricated with other techniques in a comparable design. Optimum light weight construction, special functional and individually adopted parts can be provided by using the unique capabilities of these technologies. As a consequence, practically all manufacturing market sectors and their related surroundings (design, construction) are intensively involved in elaborating solutions for their specific needs and the additive manufacturing technologies will represent an important part in the near future industrial production. Key numbers for the manufacturing industry can be derived from [2] (EU 28 in 2015): 2.1 million enterprises with 29.9 million employees generate 7,320 billion Euro turnover. The value added by the manufacturing sector represents approx. 34 % of the total non-financial business sector in Germany and 26 % in Belgium which underlines its importance for both countries. Since PONAMP concentrates on the two materials systems “Cu” and “Al”, the main targeted sectors within the manufacturing can be expected to be automotive/transportation, machinery, electrical equipment and metal products which represent a share of approx. 35 % (employees) of the whole producing market sector. The share of SME in these areas (in terms of the number of employees) varies between 20 % (automotive) up to more than 50 % (fabricated metal products or repair/machinery installation) (all numbers derived from [2]). These numbers underline the importance of the research in this field, especially for SME, to be competitive in the future.

At present, there is only a limited number of materials available for metal AM due to restrictions in the workability of alternative materials by LBM/EBM and/or by specific materials properties that impair the parts qualities. Correspondingly, and due to its early stage of implementation in industrial parts manufacturing, the AM market share is very small so far, if compared to the established manufacturing routes for metal parts. However, the AM technologies are going to be competitive with them for the above mentioned reasons. The collective research in PONAMP is dedicated to improve the availability of suitable materials by new starting materials “metal/alloy powder” and to foster the relevant AM parts manufacturing abilities for an extended range of applications in the important market sectors for light weight and electrical/electronic applications. The research consortium and the accompanying industrial partners cover the complete value chain from the raw materials manufacturing, the additive manufacturing (LBM, EBM) up to the application. Therefore, an efficient treatment of all aspects and a close-to-market focus are ensured. The innovative character makes the performed research clearly pre-competitive.

2.1.1 Economic Impact

Additive Manufacturing is a technology with notable potentials in enhancing working conditions and resource efficiency due to its possible high grade of automation and the fact that only the material for the part is consumed and waste fractions can be very low. Developments for fostering the AM

techniques will affect a huge range of manufacturing industries that clearly exceeds the applications described in the section above. For example, new material compositions and part designs can be used to improve chemical reactors or catalytic devices. According to [2], the chemical industry has the highest value added in Germany and represents the most specialized industry in Belgium. Therefore, the economic impact of AM with new, enhanced material solutions is not restricted to the focus areas of application in PONAMP and can have side-effects, too. Nevertheless, it is not advisable to give numbers here except for the consequent fact that the annual market growth for AM presently exhibits and forecasts annual growth rates in the order of 30 % [1]. This describes the situation based on the presently available machine concepts and materials. However, it can be expected and, it is necessary that this market growth is considerably pushed by new developments in all involved disciplines such as part design, materials and industrial machine concepts. The availability of new materials and concepts for their generation and processing via AM plays a key role in developing parts or completely new designs by exhausting the potentials of AM.

The aim of PONAMP is to support the manufacturing industries and its SME structured suppliers by providing specific solutions on the base of aluminium and copper alloys which will be developed with new methods for enhanced applications in the automotive, aviation and aerospace (high strength, light weight, resistance to temperature and corrosion), and in the electric/electronic sector (high electric and thermal conductivity). Since AM creates a new market sector aside to established manufacturing techniques, the impact of the PONAMP research has a great potential to create new jobs and to safeguard them by providing a technological lead in view of the international competition race. In sum, the project´s economic impact can be considerable as well as its impact on a resource efficient production and on the level of highly qualified jobs.

2.1.2 **The Need**

In general, the relatively young AM technology has still a strong need for basic and applied research in all areas along the process chain (design, materials/powder, machine/process, application). The most relevant techniques for metal parts manufacturing, such as LBM (often also called selective laser melting (SLM®)) and EBM are continuously further developed in order to meet the market requirements in terms of increasing parts size, parts precision and automation of the complete process chain. However, only a limited number of materials is available on the market yet and, the workability of technically interesting materials by using LBM or EBM processes is restricted. Consequently, materials research is named as one of the most important areas forming the base for exhausting the capabilities of the AM techniques and the corresponding application potentials [3]. Many of the present materials solutions have been qualified and are provided by the AM machine manufacturers since the resulting parts qualities are strongly related to the AM machine capabilities and the necessary process conditions. Typical failure appearances or deficiencies of AM parts, such as delamination during the process, porosity or (hot) crack formation, can be avoided only by applying the available, qualified materials with the adopted process parameters. As a consequence, the industrial design and production specialists are bound to the primary properties of these available materials.

Today, the primary challenge for AM with regard to materials is the capability in the reliable manufacturing of high quality parts for a wide variety of materials. Only a few of the more than 5,500 alloys in use today cannot be additively manufactured because the melting and solidification dynamics during the printing process lead to intolerable microstructures with large columnar grains, high residual stress and/or periodic cracks. Therefore, it is of great industrial interest to determine novel approaches for processing an extended range of alloys. There is a clear need for parts with enhanced or superior mechanical and physical properties (electrical and thermal conductivity, optimized wear

properties, high strength and corrosion resistance, …) that are not reached by existing alloys available for AM.
PONAMP focuses its research on parts manufacturing for light weight applications (Al alloys) and for applications in the electric/electronics sectors (Cu alloys). Both applications are of great importance for developing new solutions in the manufacturing industry, especially in the automotive, aerospace, electrics/electronic and machinery industry. Each of these application areas and materials groups, respectively, has individual needs or deficits to perform reliably in the LBM/EBM processes and to achieve the demanded parts properties. These are described in more detail in chapter 2.2.
Briefly described, AM aluminium alloys are based on the binary Al–Si system and have reported yield strengths around approx. 200 MPa with a low ductility of 4%. In contrast, most aluminium alloys of the 2000, 5000, 6000 or 7000 series exhibit strengths exceeding 400 MPa with ductility values of more than 10%, but parts cannot be manufactured via AM due to hot cracking and inappropriate microstructure formation. Only a few solutions have been found so far by adopting the alloy compositions itself to the needs for the AM manufacturing of higher strength parts (e. g. Scalmalloy).
Pure copper cannot be reliably manufactured to form dense AM parts by using LBM due to its low absorption of laser energy at the presently available laser wavelength (typically 1060 nm) in combination with its high thermal conductivity. Presently, technically applied Cu parts are manufactured only via the more expensive EBM route. Alloying of Cu enhances the workability with laser, but it reduces electrical and thermal conductivity dramatically already at very low alloying levels. Therefore, only a compromise between both is presently possible. A solution for greatly enhancing this situation has been developed within the Cornet project OpP3D [36]: the Cu powder is coated by materials which enhance absorption of laser light and support melting. Another solution which is state-of-the-art in the manufacturing of electrical contacts is the use of elements with no or only a low solid solubility in copper such as Cr, Nb or W. These materials are used in current manufacturing methods for copper (pure or composite materials) via melting and casting metallurgy, cold drawing or powder metallurgical routes (pressing/sintering), each having their specific limits in terms of shape complexity. LBM could overcome these restrictions. However, so far, there is no way to produce mechanically stable parts via LBM methods.
In both materials sectors SME companies are strongly involved in parts production and, the industry partners contributing to PONAMP (UC members) are clearly expressing the strong need and interest in finding solutions for the respective application areas.

2.2 State of the art

The LBM process fully melts the powder particles, instead of just sintering them and nearly fully dense parts can be produced. However, any remaining porosity can severely deteriorate the part's mechanical properties, like ductility or crack propagation. Density is thus the main physical property to be optimized in this process, but reaching 100% is very difficult by just optimizing process parameters (laser power, scan speed, scan spacing) [4]. The materials and the processes need to be optimally matched to each other in order to get good results. Although this matching is understood for the few established materials, many other promising alloys are not workable satisfactorily. The following sections describe the present situation for the AM with Al alloys and Cu.

2.2.1 Al alloys

Al-alloys such as 2017A, 2219, 7075, 7020, 6061 and 5083 can't be acceptably processed today by LBM due to hot cracking. Hot cracks form during the solidification of the metal [5,6,4,7,8]. They can occur when the available supply of liquid metal is insufficient to fill the interdendritic spaces between

solidifying metal, which are opened by shrinkage. In contrast, fine equiaxed microstructures accommodate strain in the semi-solid state by suppressing coherency that locks the orientation of the dendrites and promotes cracking (Figure 1). Ideal equiaxed structures require a high degree of undercooling, which is difficult to realize in the additive processes where high thermal gradients and cooling rates up to 10^5 K/s arise [3].

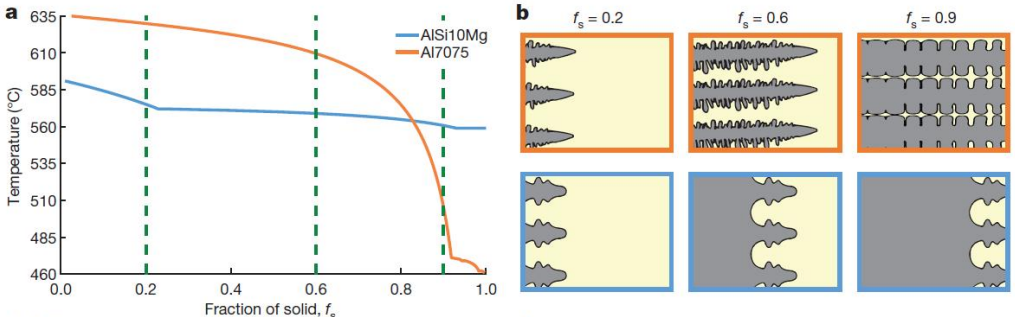

Figure 1: Solidification behaviour of AM aluminium alloys: (a) Solidification curves for 7075 and AlSi10Mg, (b) schematic representation of solidification [8].

Strong segregation up to enabling the formation of out-of-balance eutectics, significant shrinkage and, formation of unfavourable phases favour cracking. The main factor in an alloy's sensitivity to hot cracking is its chemical composition [5,6,7]. The curves in Figure 2 show the effects of different alloy additions (Si, Cu, Mg and Mg_2Si) on the crack sensitivity of aluminium. The addition of small amounts of alloying elements increases crack sensitivity, reaches a maximum and then drops to relatively low levels.

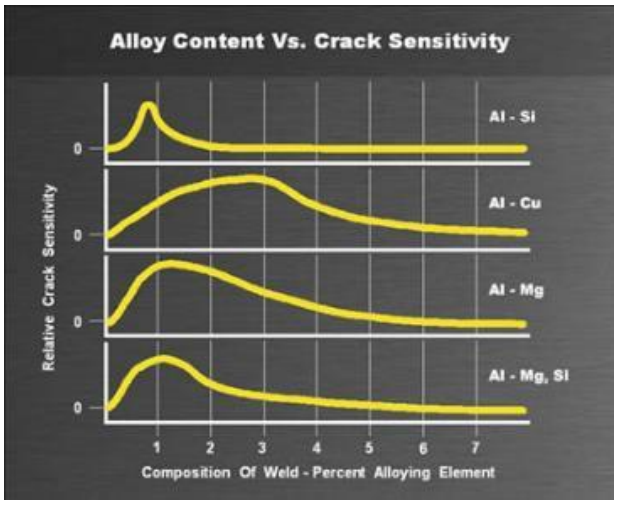

Figure 2: Effects of four different alloy additions on the crack sensitivity of aluminium [5].

The most common Al alloys for AM are the hardenable AlSi10Mg and the eutectic AlSi12. For the AlSi10Mg alloy, the very high Si content (10% by weight) avoids any hot cracking [7, 6]. Alloys in the 7000 series with copper, many alloys of the 6000 series and alloys of the 2000 series (with some rare exceptions) are well known for their high sensitivity to hot cracking. The 6xxx series of aluminium alloys are highly crack sensitive because the majority of these alloys contain approximately 1.0% Magnesium Silicide (Mg2Si), which falls close to the peak of the solidification crack sensitivity curve [5]. Alloys such as 7075 have small amounts of Cu added that, along with the Mg, increase the crack sensitivity. Moreover, the stress of solidification may cause cracking at the grain boundaries and/or establish the condition within the material promoting stress corrosion cracking at a later stage [5].

Solutions found in literature to avoid hot cracking are composed of lowering the temperature gradient during solidification (by lowering the scanning speed or increasing the preheating temperature of the building plate) or changing the composition of the alloy (by adding alloying elements or nucleants). Microstructural analysis shows that cracks are oriented in the direction of scanning. For reduction of hot cracking behaviour, lowering the scanning speed and, thus, lowering temperature gradients during solidification is a perspective [9]. Examples about actual work for solving the problems are given in Table 1. Results from tensile tests on AM parts from a nanoparticle modified Al 7075 alloy are shown in Figure 3 in comparison to pure 7075 and AlSi10Mg. The 7075 alloy with incorporation of Al_3Zr nucleant particles shows an 80% increase in strength over AlSi10Mg.

Table 1: Examples for research approaches to manufacture high strength Al parts

Solution approach	Effect	
	positive	**negative**
Al-Mg-Sc	Grain refinement and precipitation hardening (Al3Sc)	expensive alloy component Sc
Ti and Zr additions	Grain refinement	nn
Si in significant quantities	Decrease of the melting range, increase of cracking resistance	lowering strength
Elemental Si additions to 7075 alloy powder	No cracks for Si > 3-4 %, densities up to 98.9 %	less strength
mimicing 6061 alloy by powder mix Al/Si 99.4 %/0.6%	improved crack suppression	fluctuations in surface finish and fusion defects
General approach nano-particle grain refiners	low-energy barrier nucleations sites, necessary undercooling for equiaxed grain growth reduced, grain refinement, crack suppression	nn
1 Vol.-% hydrogen stabilized Zr nanoparticles, electrostatically assembled onto 7075 and 6061 alloys	favorable Al_3Zr phase formation, fine-grained, equiaxed and crack-free microstructure after heat treatment T6; mechanical strength comparable to wrought materials	nn

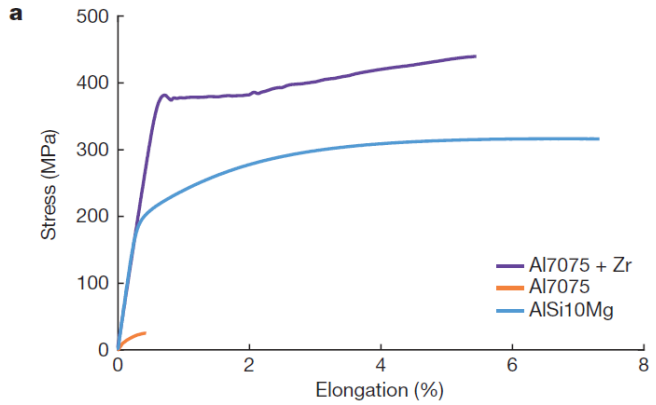

Figure 3: Stress-elongation curves of AM AlSi10Mg, Al7075, Al7075+Zr parts [5].

6xxx and 7xxx series aluminium alloys typically get their strength from precipitation hardening. However, they contain elements such as Mg and Zn that are highly volatile at higher temperatures due to a low vapour pressure. At the maximum temperature reached in the melt pool, these elements may vaporize during laser melting, leading to a variation in chemical composition and inducing turbulences in the melt pools, increase splatter formation and porosity and are, therefore, not suited to be used in AM [10,11].

2.2.2 Pure copper

The main benefit of using pure copper is its good thermal and electrical conductivity. However, the material is extremely difficult to process with laser melting at the presently used 1060 nm wavelengths (power normally required is around 800-1000W) [12,13,14]. The reflectivity of the pure copper prevents efficient energy absorption and material melting to form dense parts. Therefore, EBM is used for making Cu parts [15, 16, 17, 18] by accepting the disadvantages of mutually higher costs, less surface qualities and limits for the minimum possible structuring. The process requires a coarser powder particle size range than its LBM counterpart, and it is worth investigating how far this size range can be reduced to improve the surface state and minimum structure thickness.

To bypass the limitations with laser powder bed technology alloying elements that increase the laser absorption can be added which degrade the thermal and electrical conductivity not too much. However, the full advantage of pure copper is gone once alloying elements are added due to the steep decrease of conductivity at already very low alloy concentrations. Therefore, there is a lack of alternatives for making highly conductive AM parts. One possible way is the use of alloying elements with no or a low solid solution in the copper matrix.

2.2.3 Copper-based composite materials

The combination of copper with refractory materials (Nb, W, Ta, Cr) is essential for many applications in the electronics sector, since it offers an excellent compromise between tensile strength, wear resistance and electrical / thermal conductivity. The minimal solid solubility of additions such as Cr, Nb, Ta or W in Cu preserves the conductivity more, if compared to other systems with higher solid solubility. Simultaneously, the hard refractory metal particles support the copper matrix and increase tensile strength.

Tungsten-Copper is being employed as medium- and high-voltage circuit breaker, for electrical contacts, and welding and erosion electrodes. The classical production way follows either the sintering of a porous tungsten matrix with subsequent copper infiltration (10-40 w% Cu), or the liquid phase sintering of both components (> 50 w% Cu). Commercially available Cu-W with copper contents below 50 wt.-% reach hardness values of 120-180 HRB and an electrical conductivity in the range of 35-58 %IACS [19,20,21]. Copper-Chromium (>50 wt.-% Cu) reaches conductivities between 36 and 82 % IACS and hardness values between 85 and 110 HV30 [22]. For the production of Cu-Nb materials, which are for example used as conductor wires for pulsed high-field magnets, several time-consuming ways of production are described: hot extrusion, cold drawing of the solidified material and, powder metallurgical routes (Nb content in the copper matrix up to 10 wt-%). A tensile strength of up to 1 GPa at a conductivity of 55 % IACS results. [23,24,25,26,27].

The processing of composite materials via LBM is described in the literature, for example Cu-Cr [28, 27], WC-Cu [29, 28], and W-Cu [30, 31]. In [27] a mixture of Cu and non-spherical Cr particles was used. The obtained microstructure consists of segregated Cr with a wide size distribution in the Cu matrix (Figure 4a). A mixture of dendrite shaped Cu powder with an equiaxed WC powder a maximum relative density of 96 % could be achieved [29]. The processing of W-Cu with LBM [30] was not completely successful because of balling effects during processing and the maximum density was below 70 %. The processing with *direct metal laser sintering (DMLS)* of a similar alloy [31] allowed to obtain a microstructure with regular-shaped, chain-like structures of tungsten in the Cu matrix (see Figure 4b) and to increase the final density to 92 %. Plasma spheroidization has been used to treat W and Mo powders which feature an irregular morphology in order to provide a spherical shape of the particles for a better powder flowability [32,33,34,35]. After plasma spheroidization the absorption coefficient of tungsten powders for a laser with 1070 nm wavelength (used for LBM) was increased by 15% and

the powder flowability increased [34]. By summing up the literature review, no satisfying solutions are presently available for making dense and highly conductive Cu parts via LBM.

a) 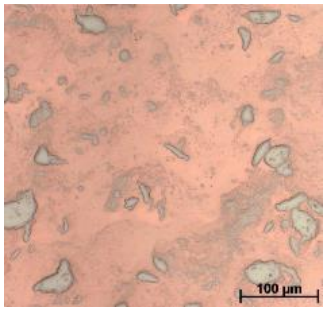

b) 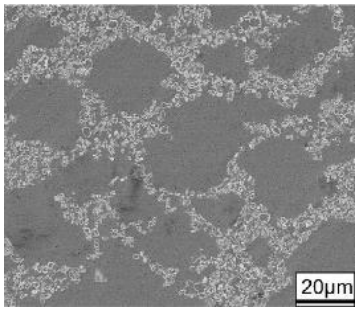

Figure 4: a) Microstructure of the Cu-Cr alloy processed by LBM [28] b) Microstructure of W-Cu alloy processed by DMLS [31]

Within PONAMP the introduction of refractory metals has been performed via coatings on Cu powders and via composite powder manufacturing using mechanical alloying, suspension plasma spraying techniques (SPS) and a two-step atomization method. Mechanical alloying is closest to the state-of-the-art and has potentially to be combined with a plasma spheroidization step in order to get good powder flowabilities and packing densities. The composite manufacturing via SPS might be nearest to the electrostatically assembled Zr nano-particles on Al alloy described by [5]. The difference is that SPS will use particles up to 5 µm which meet the Cu powders as liquid droplets and thus will have a mechanical bonding. The development focus with coatings on the powder particles is also new for such material groups and AM. Only in the CORNET project OpP3D [36] such coatings have successfully been applied in order to enhance laser absorption and to foster the achievement of dense parts. In Figure 5 a LBM test part made from pure Cu powder and from a Ti coated Cu powder are compared. The density increase for these low power treated samples (100 W) is evident. The coated powder was employed to build a coil for highly efficient electric motors with light-weight design for mobile applications (see Figure 6). After a solution heat treatment, the produced parts had an electrical conductivity of 31% IACS and a hardness of 74HV1.The results show the great improvement in the processability of the powders and, therefore, demonstrate the validity of the respective research approach in PONAMP.

a) 

b) 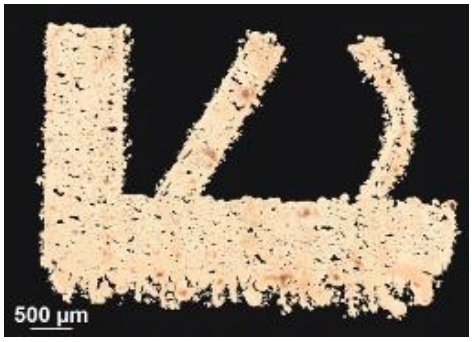

Figure 5: Effect of coating on copper powder for LBM process a) Pure Cu powder (25% porosity) and b) Cu powder with Ti coating (3,5% Porosity)

Figure 6: Coil for highly efficient electric motors (Design by Unicorn Engineering GmbH): (left) CAD Design / (right) Part additively manufactured by LBM employing Ti-coated powder.

3 Description of the project results

3.1 Results of the single workpackages

Based on the working hypothesis (surface treated powders allow for improved production) and the derived four-step process (powder procurement and/or development, powder surface treatment, fabrication of test parts, characterization of test parts), the project's overall work is divided into six work packages (WPs, see Table 2). WP0 is devoted to project management, while WP1 to WP4 cover the technical development aspects according to the four-step process flow and, WP5 covers all aspects of dissemination. Table 2 gives an overview about the single work packages and planned time intervals. A project prolongation of 6 months has been granted in order to fulfil all research aspects successfully due to delays caused by the Corona pandemy.

The results achieved by each research performer are presented separately under the relevant chapters..

Table 2: Overview on workload and (originally planned) time schedule

work package	activity/task	time period (project months)																						
		1	2	3	4	5	6	7	8	9	10	11	12	13	14	15	16	17	18	19	20	21	22	23	24
WP 0	**Project management**	D0.1					D0.2						D0.2						D0.2						D0.2 D0.3
	SC and UC Meetings (national/international)																								
	Project coordination/WP coordination																								
WP 1	**Materials and powder development**																								
1.1	Application and testing protocol description		D1.1																						
1.2	coatings, composites), materials identification and approval									D1.2			D1.3												
1.3	Development of Cu and Al alloy powders												M1.1						M1.2						
1.4	Development of composite manufacturing routes												M1.1								M1.2				
WP2	**Surface modification of powder materials**																								
2.1	Coatings on flat substrates by magnetron sputtering																								
2.2	Processing of coatings on flats substrates by laser												D2.1												
2.3	Optimization of the deposition rate with hot magnetron																		D2.2						
2.4	Optimization of the coatings on powders by hot magnetron																			M2.1	D2.3				
2.5	Coated powder for partners																				M2.2				
WP 3	**Processing of Al-alloys by LBM**																								
3.1	Processing of coated Al-alloys powders by LBM																								
3.2	Thermal treatment of built parts																D3.1								
3.3	Characterization of produced samples																								
3.4	Feedback to partners																								
3.5	Manufacturing of demonstrators																							D3.2	
WP 4	**Processing of Cu and Cu-alloys by LBM/EBM**																								
4.1	Processing of Cu and coated Cu alloys by LBM and EBM												D4.1												
4.2	Investigation on the parts / Comparison EBM-LBM																		D4.2				D4.3		
4.3	Feedback to partners																		M4.1						
4.4	Manufacturing of demonstrators																							D4.4	
WP 5	**Dissemination activities**																								
5.1	Workshops for industry																								
5.2	Internet presence																								
5.3	Presentation at scientific conferences and industry fairs																								
5.4	Publications																								D5.2

3.1.1 WP0: Project Management

The project partners met regularly during the course of the project. A kick-off meeting and four further steering committee meetings were coordinated and held every six months. In coordination with all research partners, also four SME user committee meetings took place (on a respective national level), and a public final workshop with all the industry partners was organized at the end of the project (see Table 3 for a detailed list). The project meetings served essentially to present and discuss the research results, as well as to discuss further steps. The project coordinator at fem kept contact via phone with the other partners during the course of the whole project.

The final meeting has been organized a joint online meeting open to all the Belgian and German industry partners, in order to present the project results to all the participants.

Table 3: List of the conducted project meetings

Steering committee meetings		SME committee meetings	
Date	*Place*	*Date*	*Place*
05.09.2019	fem, Schwäbisch Gmünd	10.09.2019	fem, Schwäbisch Gmünd
17.03.2020	Online	16.09.2020	Online
08.09.2020	Online	04.05.2021	Online
03.03.2021	Online	11.11.2021	Online
09.09.2021	Online	17.02.2022	Online (Final joint meeting)
30.11.2021	Online		
20.01.2022	Online		

3.1.2 WP1: Materials and Powder Development

3.1.2.1 Performed activities – fem / UMSICHT

- Establishing of a quick screening method for choosing material pairs

In order to quickly assess the potential of suitable material pairings, a simple test method with coated sheets was established in this work package. The coated sheets are exposed once in the LPBF system and the melt traces produced are evaluated metallographically (melt zone width, depth and alloy formation/precipitation). Uncoated sheet metals have been treated identically as a reference in each case. This screening method allowed a quick evaluation of the effect of the coatings and served to select the most suitable material pairings for subsequent powder coatings.

Figure 7 shows the selected exposure pattern for the Cu and Cu alloys: the exposure is carried out with 95 W (at fem) and 270 W (at Umsicht) laser power while varying the laser scanning speed (numerical values in Figure 7**Fehler! Verweisquelle konnte nicht gefunden werden.**) for three arrays each. The main difference of both laser systems has been the available laser focus area (∅35 µm at fem, ∅70 µm at UMSICHT). For facilitating the comparability of the results from both systems, UMSICHT used identical scanning speeds. Consequently, the areal energy inputs are slightly higher than the ones realized at fem and reach nearly identical energy levels for 250 mm/s (UMSICHT) and 200 mm/s (fem) (see Figure 7**Fehler! Verweisquelle konnte nicht gefunden werden.**). The PVD coatings have been applied by Materia Nova in using Cr, Mo, Nb, Ta and W as coating materials on the different Cu and Cu alloy sheets.

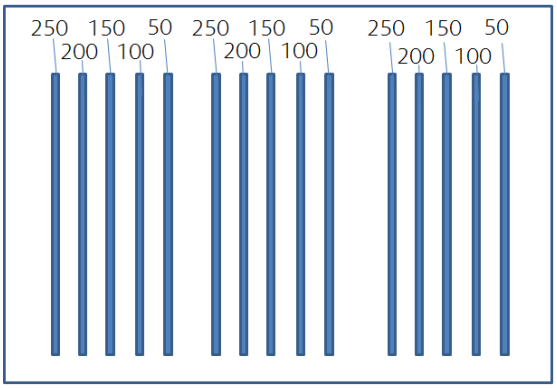

scan speed	fem	UMSICHT
mm/s	J/mm²	J/mm²
250	12,7	**15,4**
200	**15,8**	19,3
150	21,1	25,7
100	31,7	38,6
50	63,3	77,1

Figure 7: Selected pattern for the single track melting on pure and PVD coated Cu and Cu alloy sheets with the table of applied scanning speeds and areal energy densities realized at fem and UMSICHT.

Simliar investigations have been performed at UMSICHT in coordination with Sirris for uncoated and Zr and Ti coated Al 7075 alloy sheets. The respective track and areal melt zones with the applied parameter fields in terms of areal energy densities are depicted in Figure 8**Fehler! Verweisquelle konnte nicht gefunden werden.**. Sirris used a laser system with 350 W laser power max and ∅70 µm focus area for these experiments.

The results of these investigations are summarized under the section 3.1.3 (Cu) and 3.1.4 (Al).

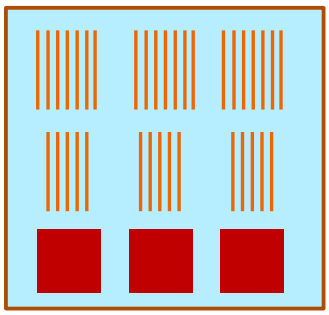

Areal energy density E = P/d·v

P = Laser power, d = beam diameter, v = scan speed

Energy density according to scanning parameters for Al alloy sheets

Laser scan speed v [mm/s]	Sirris	360	320	280	240	200	Focus diameter [µm]	Laser power [W]
	UMSICHT	275	250	215	185	155		
Energy density E per unit area [J/mm²]	Sirris	13,9	15,6	17,9	20,8	25,0	70	350
	UMSICHT	14,0	15,4	17,9	20,8	24,9		270

Figure 8: Selected line and areal pattern for the laser melting on pure and coated Al 7075 alloy sheets with the table of applied scanning speeds and areal energy densities realized at Sirris and UMSICHT.

3.1.2.2 Performed activities – UMSICHT

- Manufacturing of powders via melt atomization

Four melt atomization experiments with CuNiAl alloys and Cu have been performed by using a standard close-coupled atomization nozzle system and a pilot atomization unit (melt capacity up to 100 kg per batch, see Figure 9). Melting and atomization have been undertaken under nitrogen atmosphere.

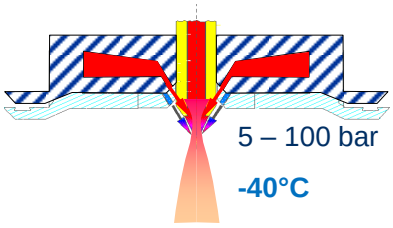

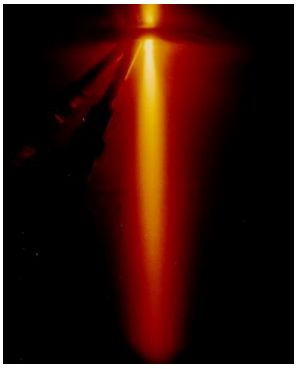

Figure 9: Pilot atomization unit (left picture, right tower), sketch of a close-**coupled atomization nozzle (upper right) and atomized molten particle jet (lower right).**

The main goal for those manufacturing procedures is the achievement of a particle size distribution that has its main particle mass inside the demanded size range. For the present laser based AM techniques, this range has been specified to be within 10 µm to 40 µm or 30 µm, respectively. Figure 10 and Figure 11 display the achieved results and show an increasingly better performance in yield with progressing optimization of the atomization parameters from 25 wt.-% up to 35 wt.-%. The powder particles are mainly spherical and ensure a good flowability.

The powders have then be classified via inert sifting into the demanded size fractions. The CuNiAl alloy powders have been handed out to fem for further investigations and AM processing of the powders. 4 kg of the pure Cu powder was sent to Materia Nova for PVD coating and subsequent further AM processing at fem. The rest of the Cu powder has been used for the composite powder manufacturing at UMSICHT (see section 3.1.3.1)

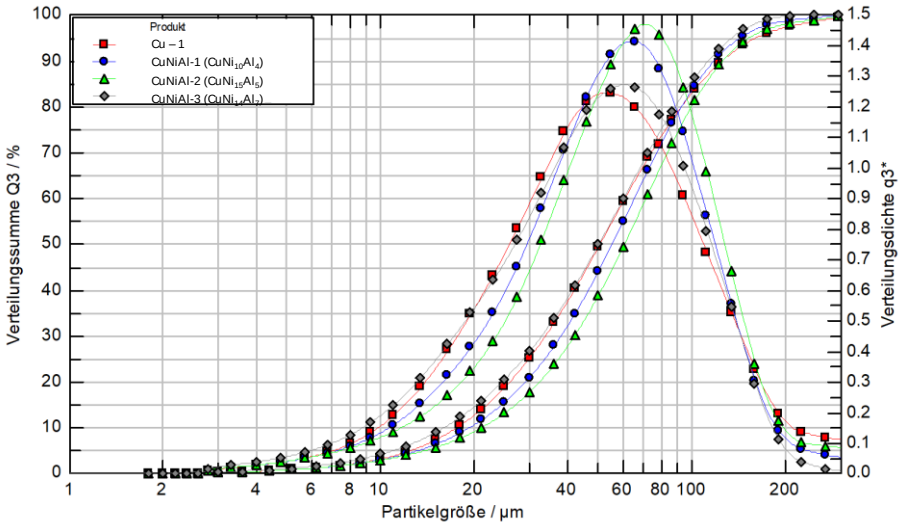

Figure 10: Particle size distributions of the as-atomized Cu and CuNiAl powders.

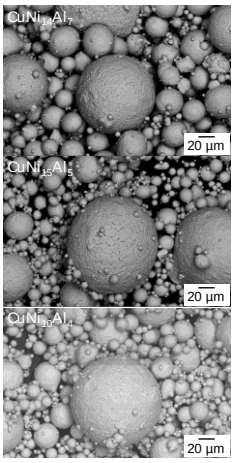

Cu and Cu alloy powder manufacturing							
Composition (at.-%)	Cu (wt.-%)	Ni (wt.-%)	Al (wt.-%)	batch no.	d_{50} [µm]	yield	
						kg overall	% in 10-40 µm
Cu_{100}	100			Cu-1	50,2	59,2	35 %
$CuNi_{14}Al_7$	83.24	13.62	3.13	CuNiAl - 3	50,5	29,9	35 %
$CuNi_{15}Al_5$	83.38	14.43	2.21	CuNiAl - 2	55,5	24,5	30 %
$CuNi_{10}Al_4$	88.72	9.53	1.75	CuNiAl - 1	60,7	14,3	25 %

Figure 11: Morphologies of the as-atomized CuNiAl powders and table of alloy compositions, batch no. with achieved values for $d_{50,3}$ and yield in the size fraction 10 µm to 40 µm.

3.1.3 WP2: Surface modification of powder materials

3.1.3.1 Performed activities – UMSICHT

- Preparation of composite powders

The research work in the OpP3D project has clearly shown that thin coatings on powders are strongly supporting the manufacturability of critical materials like copper (high reflectivity) through the LPBF technique. The aim of this working package at UMSICHT was the investigation of an alternative surface modification for these powders by using particulate second materials that at least partially cover the Cu surfaces. Mechanical mixing routes and the technique of suspension plasma spraying (SPS) on Cu powder have been suggested for the preparation of such powders (figure 12). In the course of the project, a third method has been developed and investigated, a two-step atomization process that forms such Cu-X composites directly during the Cu powder manufacturing. Hereby, the "X"-component is co-injected directly into the gas atomization jet (= first step) and hits the atomized particles (= second step) while they are still liquid or at least pasty (Figure 12). As described before, fine tungsten powders (d_{50} < 1.7 µm) have been chosen for the mechanical route as well as for the co-injection process. For the SPS process Al_2O_3 suspensions have been used. The single results are summarized below.

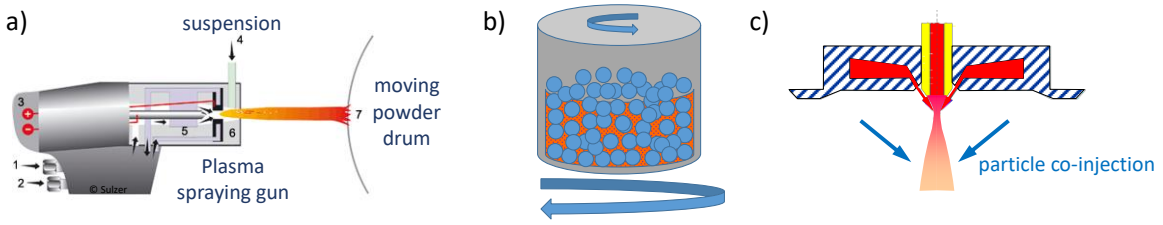

Figure 12: Schematic illustration of the investigated methods a) suspension plasma spraying, b) mixing/"mechanical alloying" and c) two-step atomization.

i) Suspension plasma spraying

The goal by using this technique was to direct a fine particle jet (< 1.5 µm Al_2O_3) in the liquid (molten) state onto a moving powder bed. The feeding of such fine particles into the hot zone of the plasma jet is only feasible by using suspensions. Intense trial campaigns have been performed with this set-up. However, no parameter set could be found that allowed a permanent bonding of the Al_2O_3 particles onto the Cu powder particles. The identified main reasons were:

- The process is characterized by the fact that the fine molten Al_2O_3 particles are solidifying rapidly after leaving the hot plasma zone due to their low volume that is equivalent to the stored heat inside those particles. In order to avoid premature solidification before their impact onto the Cu powder, very short distances (around 100 mm) have to be realized. Under these conditions, the plasma jet blew the Cu particles out from the reservoir.
- By increasing the distance the Al_2O_3 particles are already solidified and no adherence onto the Cu particle surfaces can be achieved

ii) Mechanical route

The mechanical route was realized by mixing Cu powder with a $d_{50,3}$ = 18 µm with fine W powder (finally $d_{50,3}$ = 7 µm). A series of experiments has been performed by varying the volume percentage of the W addition and the mixing/milling ("mechanical alloying") energy in terms of the rotation speed and the duration of the mixing/milling process (1 to 10 minutes). The results can be summarized as follows:

- The technique is feasible for generating a Cu-W composite powder where the tungsten particles are permanently bonded onto the Cu particle surfaces.
- The fraction of bonding W particle increases with milling energy and reaches a nearly > 90 % fraction for mixing times above 3 min

- Heat is generated during the mixing process and the Cu powder deform visibly with increasing milling energy (Figure 13). Simultaneously, the fraction of agglomerated particles increases.
- Under optimized conditions, a good joint between Cu and W particles can be realized with low particle deformation and agglomeration (< 20 wt.-%).

This latter point can be clearly demonstrated by comparing the particle size distributions in the original and the treated states (Figure 14). The fraction of detaching W particles during the dry dispenser of the particle sizer (Sympatec HELOS) is only around 1 vol.-%.

The powders produced under the estimated optimum conditions with a W content of 3 vol.-% have been processed via LPBF on a 3D Systems ProX200 unit by using various parameter sets. The generated test cubes have then been investigated in terms of porosity and surface roughness (see section 3.1.5.2).

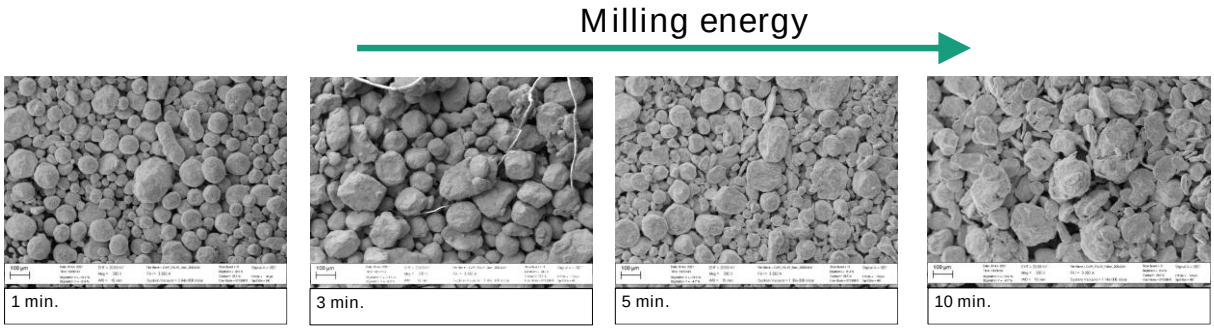

Figure 13: Increasing particle deformation with milling time.

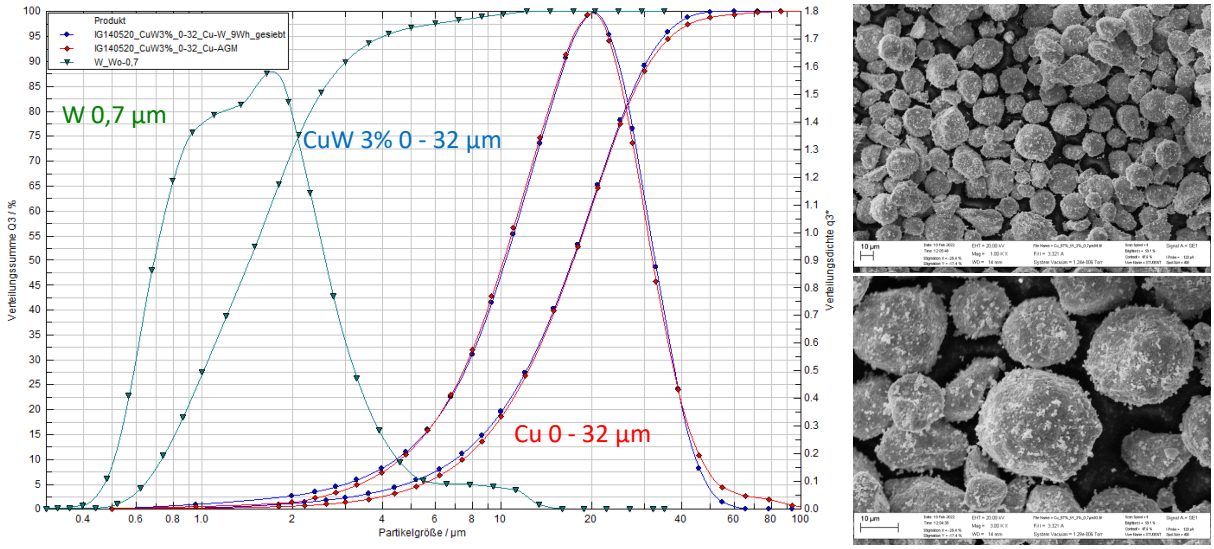

Figure 14: Particle size distributions of the starting powders ($d_{50,3}$ Cu 18 µm, W 0.7 µm) and the milled Cu-W powder with permanent bonding of W particles on the Cu particle surfaces.

iii) Two-step atomization

For setting up the two-step atomization mainly several technical aspects had to be solved:

1. The fine tungsten powders are flammable and are prone to form explosive mixtures with oxygen containing atmospheres. Consequently, the experiment had to be performed by using a special atomization equipment respecting safety requirements

2. The mass ratio of liquid (atomized) copper and co-injected W has to be adjusted. This has been realized by adopting a pressurized powder feeding system that transports the W powder with adjustable feeding rates between 25 g/min up to 140 g/min.
3. An atomization nozzle had to be designed (see Figure 12 c) that allows the injection of W powder
    a. at a location as close as possible to the atomization jet for hitting liquid Cu droplets
    b. without causing detrimental effects on the atomization process itself.

Due to these complex challenges the set-up of the system was time-consuming and, finally, only one experiment could be realized successfully within the project duration. This experiment has been performed with a melt flow rate of approx. 2.2 kg/min Cu and a W feeding rate of approx. 70 g/min, equivalent to a volume percentage ratio Cu/W of 98.5/1.5. Figure 15 shows the generated powder. The results can be summarized as follows:

- The atomized Cu particles are quite regularly covered by the fine W particles. The coverage is much less, if compared to the ones achieved via the mechanical route.
- The atomization efficiency is not impaired remarkably. The Cu powder particles are mainly spherical. A slight increase in agglomeration might be present.
- The microscopic evaluation shows that only a fraction of the injected W powder is bonded at the Cu surfaces

The feasibility of producing Cu-W composite powders via a two-step atomization process could successfully be demonstrated. Process conditions and nozzle set-up have still to be optimized in order to increase the bonding efficiency of W on Cu.
The atomized Cu-W powder has been processed via LPBF by using identical parameter sets to the ones applied during the test cube manufacturing of the mechanically generated Cu-W 3 % powder. In both cases, the particle size fractions 10 µm to 32 µm were used. The generated test cubes have then been investigated in terms of porosity and surface roughness (see section 3.1.5.2).

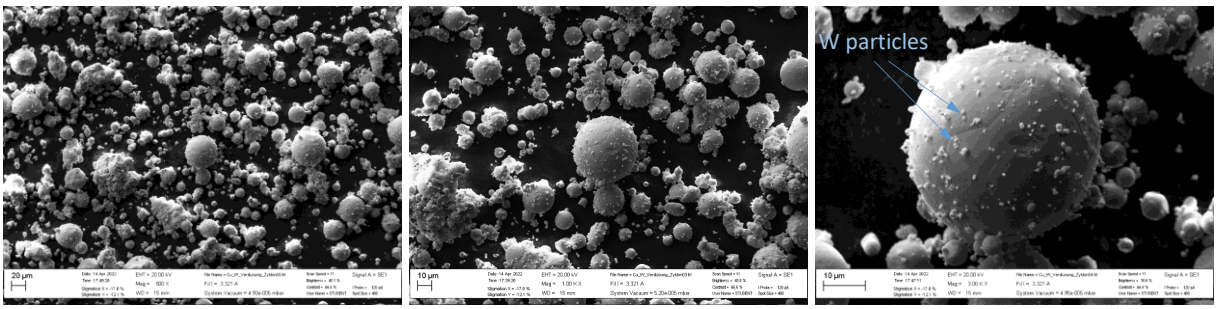

Figure 15: Cu-W composite powders in the as-atomized state, generated via two-step atomization.

3.1.3.2 Performed activities – Materia Nova (I)

The aim of this WP was to produce coatings on metallic powders based on the materials selection in WP1. Firstly, an optimisation of materials was started on flat substrates. A study of plasma parameters was realized to increase the economic profitability of the process. Finally, the metal powders were treated based on the previous tasks.

Coatings on flat substrates by sputtering magnetron

To identify the materials to be deposited on the metal powders (Al and Cu alloys), a first development was done on flat substrates in accordance with WP1. For this step, the deposits were carried out by conventional magnetron sputtering. Morphology (SEM) and chemical composition (XPS and SEM-EDX) were realized before sending the samples to our partners to study. Depositions on flat substrates were realized on the vacuum chamber presented in Figure 16.

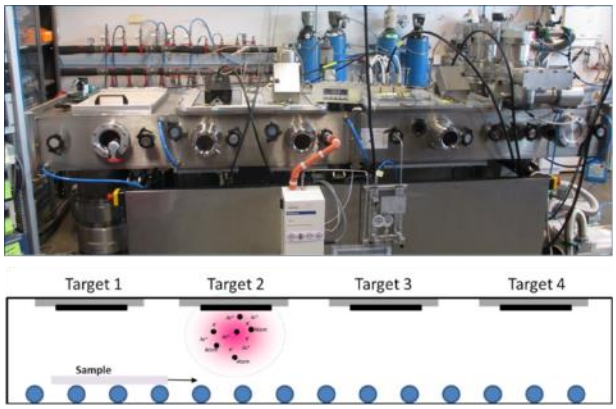

Figure 16: Inline sputtering system

Deposition of copper alloys on a flat substrate

For this work, different metallic deposits on copper alloys were carried out as illustrated in Figure 17:

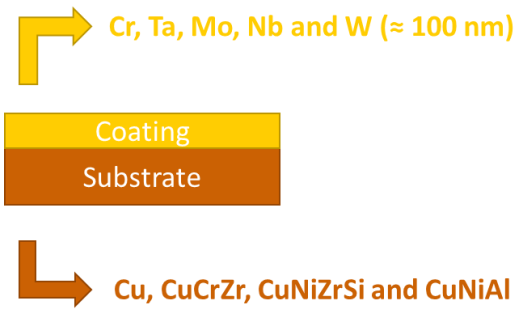

Figure 17: Metal deposits on copper alloys

As an example, the work was carried out as shown in Figure 18 and Figure 19:

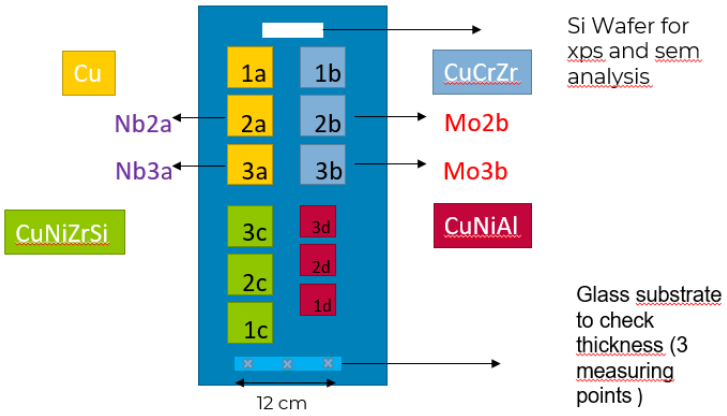

Figure 18: Layout diagram of copper alloy deposits

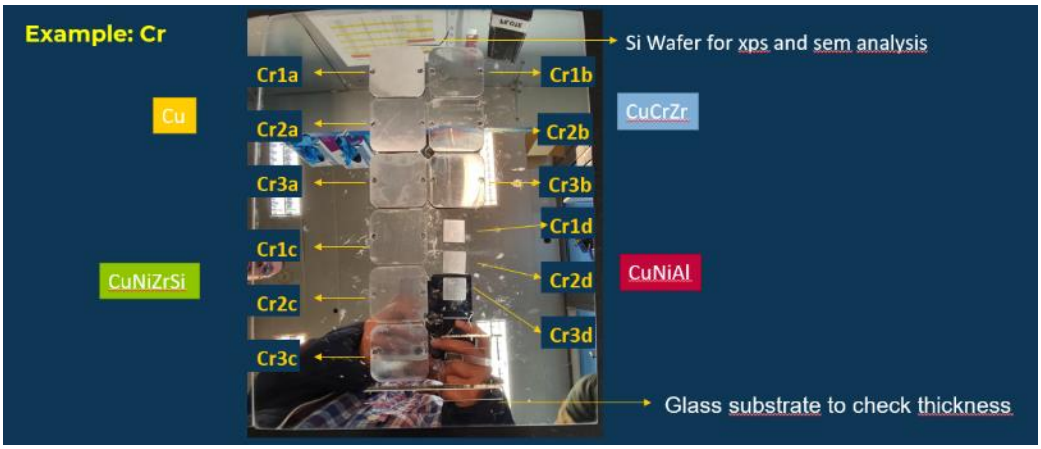

Figure 19: Cr deposits on copper alloys

- *Thickness measurements: Dektak® stylus profilers*

Measurements by mechanical profilometer were carried out on each of the batches carried out to verify the thickness and homogeneity of the metal deposits (Figure 20).

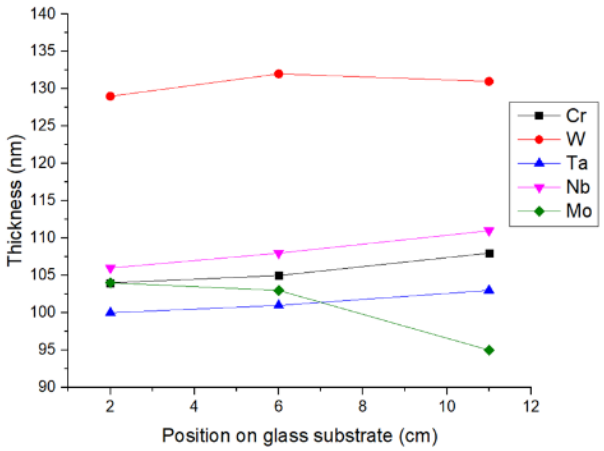

Figure 20: Measurement of thicknesses by mechanical profilometer

The thickness is of the order of 100 nm and is homogeneous over all thin films.

- *Observation by scanning electron microscopy (SEM)*

Electron microscopy observations were made on each of the deposits to verify the thickness and quality of the metal deposits (Figure 21).

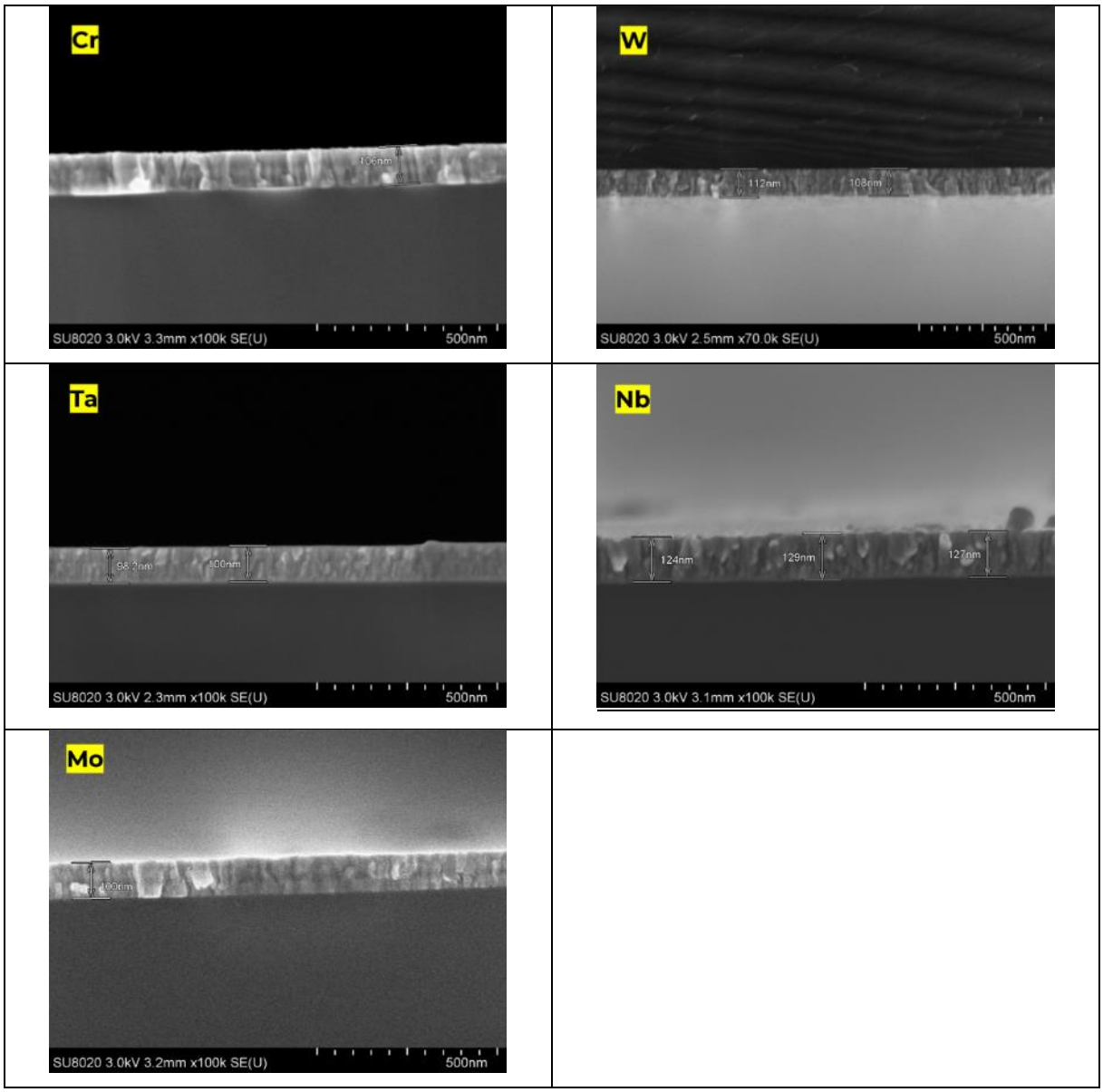

Figure 21: SEM observations of metal deposits.

- *Chemical quantification by XPS of metal films*

The metal films were chemically quantified by XPS (X-ray photoelectron spectrometry) to verify the quality of metal deposits and oxygen levels (Figure 22).

A thickness profile was made for each of the samples.

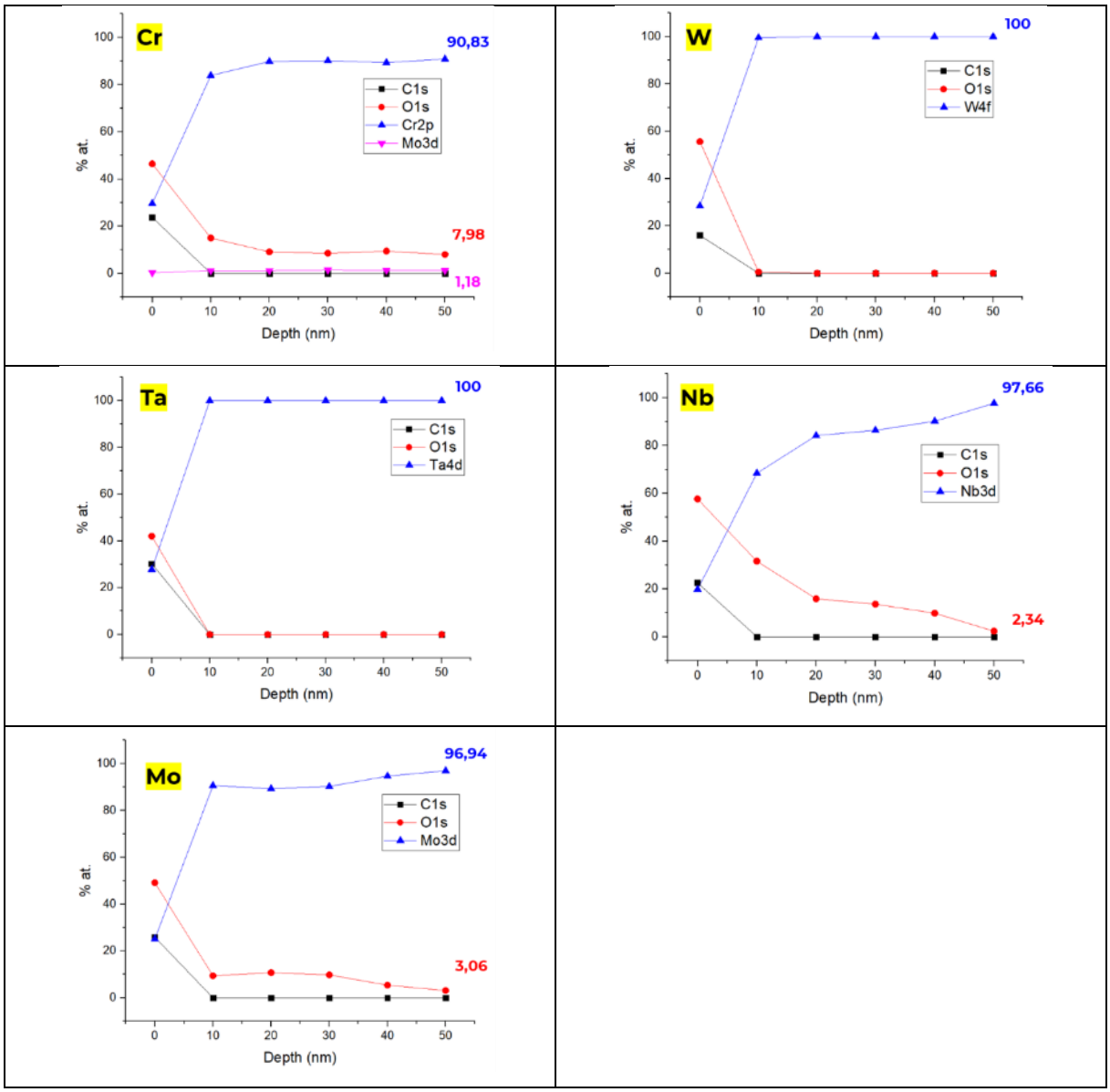

Figure 22: Chemical quantification and XPS profile of metal films.

The films observed are metallic, the oxygen level present is less than 8at% and there is no chemical impurity.

- *Summary*

- Dektak® stylus profilers: the thickness is ≈ 100 nm
- SEM observations: homogeneous films of ≈ 100 nm
- Chemical composition (XPS): Metal films and oxidation as follows:

  Cr > Mo > Nb > Ta,W

Deposition on flat substrates of aluminium alloys

For this work, different metal deposits were made on aluminium alloys as illustrated in Figure 23.

Figure 23: Metal deposits on aluminium alloys

The work was carried out as shown in Figure 24 and Figure 25:

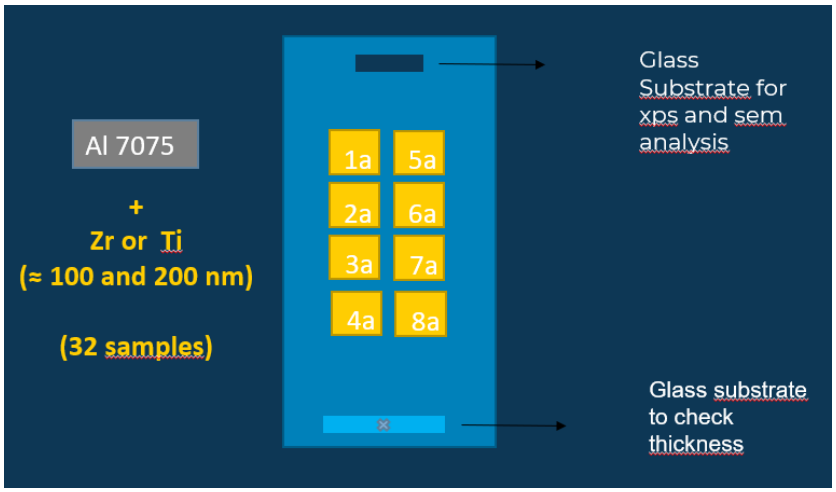

Figure 24: Layout diagram of deposits on aluminium alloys

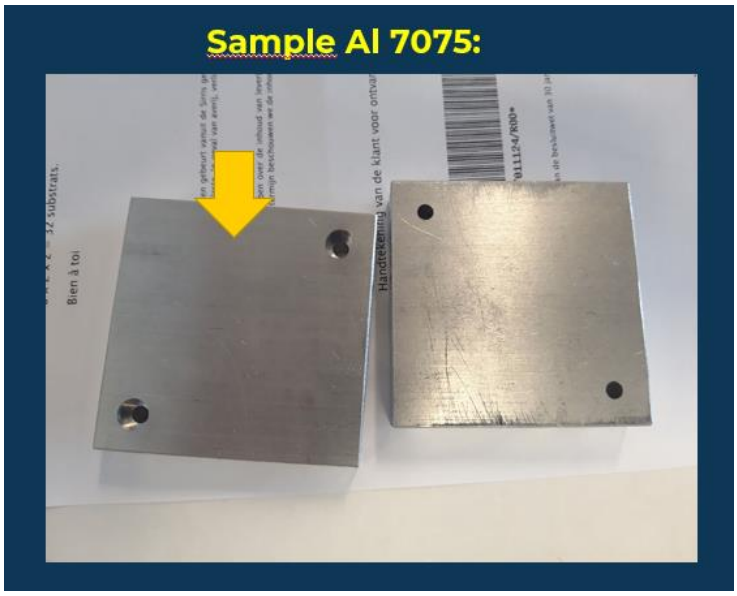

Figure 25: Aluminium alloy substrates before deposition.

- *Thickness measurements: Dektak® stylus profilers*

Measurements by mechanical profilometer were carried out on each of the batches in order to verify the thickness (100 and 200nm). See Table 4.

Table 4: Measurements by mechanical profilometer

Materials	Thickness measurements (nm) - Dektak
Zr	72
Ti	98
Zr	206
Ti	196

The thickness is in the order of 100 and 200 nm.

- *Observation by scanning electron microscopy (SEM)*

Electron microscopy observations were made on each of the deposits to verify the thickness and quality of the metal deposits (Figure 26).

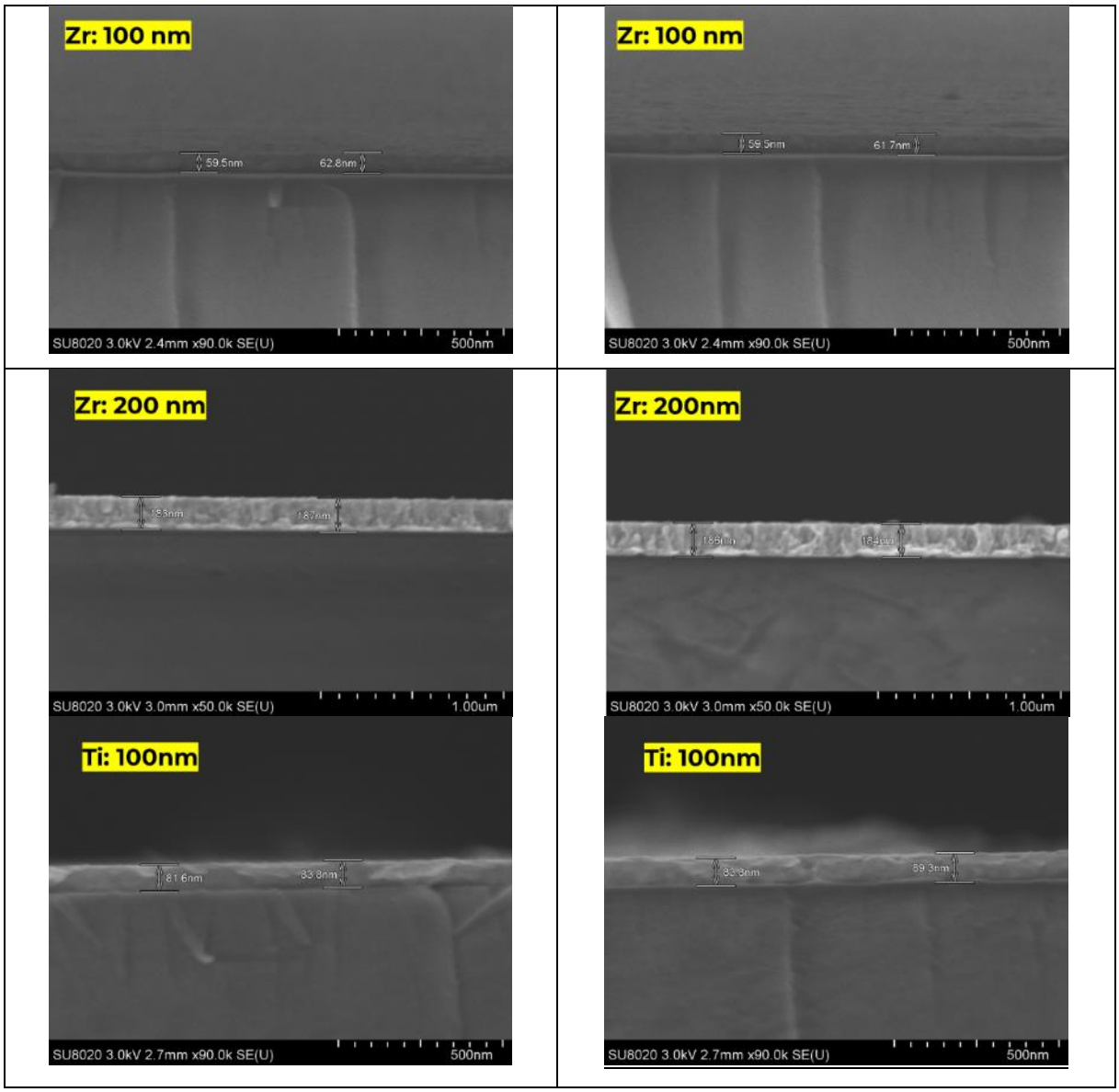

Figure 26: SEM observations of metal deposits.

- *Chemical quantification by XPS of metal films*

The metal films were chemically quantified by XPS (X-ray photoelectron spectrometry) to verify the quality of metal deposits and oxygen levels (Figure 27).

A thickness profile was made for each of the samples.

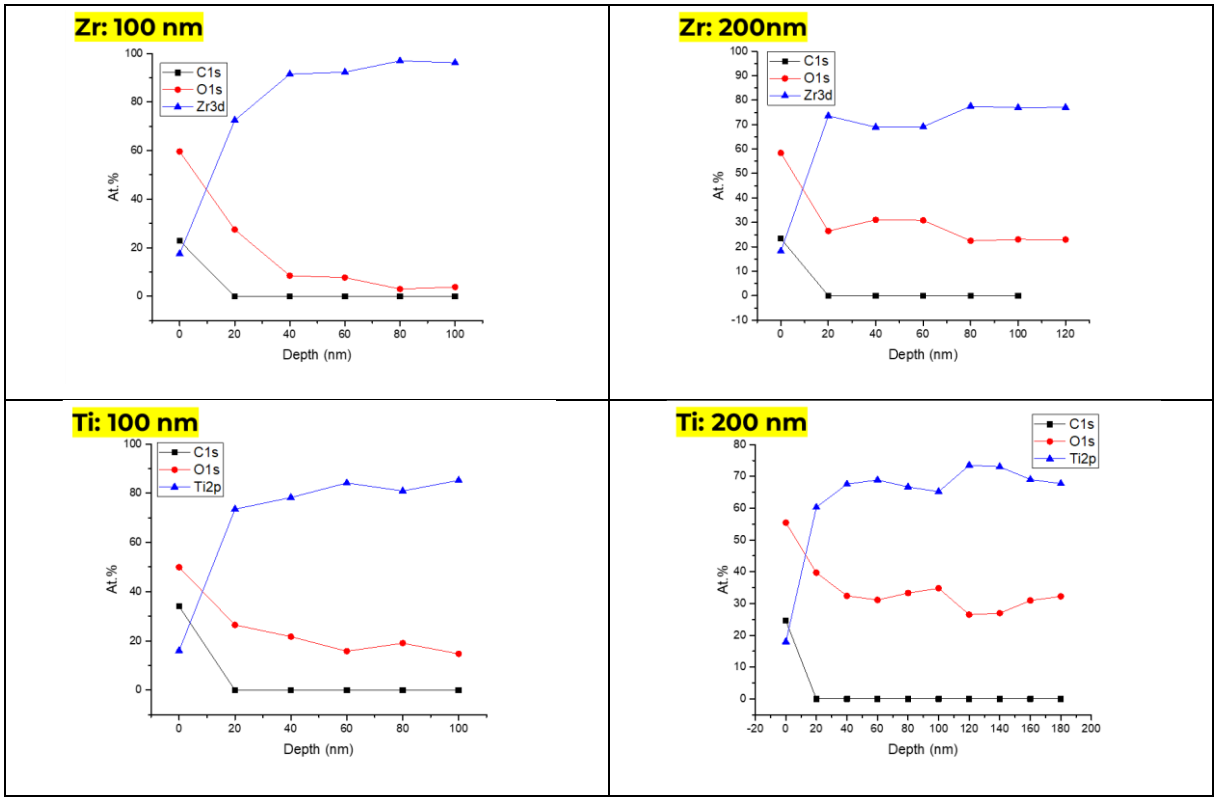

Figure 27: Chemical quantification and XPS profile of metal films.

The films observed are metallic, the oxygen level present is less than 40% at. and there is no chemical impurity.

- *Summary*

- Dektak® stylus profilers: the thickness is ≈ 100 and 200 nm
- SEM observations: homogeneous films of ≈ 100 and 200 nm
- Chemical composition (XPS): Metal films and oxidation as follows:

Ti > Zr

Conclusions

In this task, different metallic depositions were realized on metallic powders. For copper powder, deposition of Cr, W, Ta, Nb and Mo on the copper alloys Cu, CuCrZr, CuNiSiCr and CuNiAl.
For aluminium, deposition of Zr, Ti, B*, Mg* on the aluminium alloys Al 7075, AlCu4MgTi and Al 7020.
Note: B and Mg are not shown here.

3.1.3.3 Performed activities – UMONS

Optimization of the deposition rate with hot magnetron

The main research activity of the UMONS team in the PONAMP project was the detailed study of the parameters of the magnetron plasma deposition process in order to increase the economic efficiency of the process. In other words, the aim was to determine the relationship between the working parameters, the plasma characteristics and the film properties.

The magnetron deposition chamber has been adapted to allow operation in Hot Magnetron Sputtering (HMS) regime by arranging spacers under the sputter target (see Figure 28) but also to allow the analysis of the plasma and its interaction with surfaces thanks to adequate methods such as time-resolved optical emission spectroscopy (OES), film growth rate measurement and the analysis of the electrical parameters of the discharge.

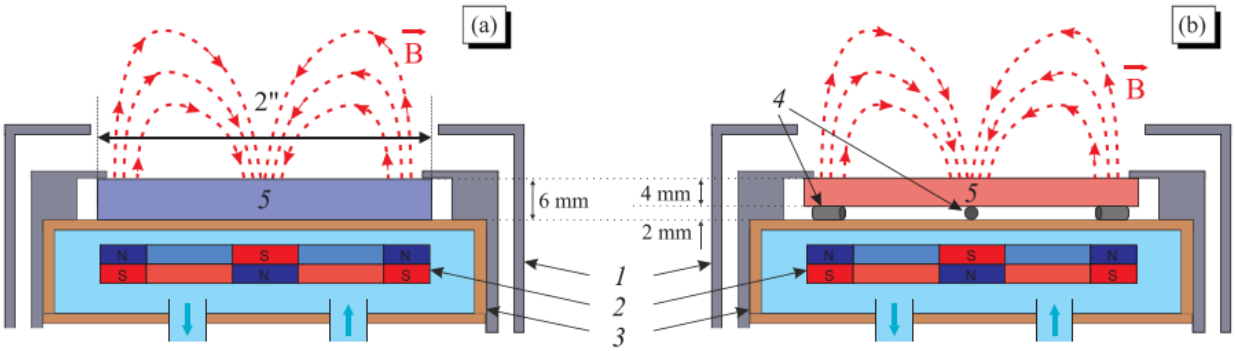

Figure 28 : Magnetron source configurations with: (a) a cooled target (the CMS system); (b) a thermally insulated target (the HMS system). 1—anode, 2—permanent magnets, 3—water-cooled assembly, 4—tungsten spacers, 5—Nb targets

The critical point at the moment when the magnetron cathode enters the hot magnetron regime was first determined. This can be determined by observing the current and electrical voltage displayed by the power supply whose power is regulated. When the target is hot, the emission of secondary electrons from the surface of the sputter target becomes important because the thermionic emission mechanism engages. The electric current then becomes very important. As the power supply operates in regulated power regime, if the current increases, the electrical voltage must decrease to maintain the imposed power value. Figure 29 illustrates this effect in the case of Titanium, Niobium and Tungsten sputtered into argon. In this figure, we can see that Tungsten does not have a critical point in the power range accessible with our system. It is apparently not possible to achieve the hot magnetron regime with this material in our case. However, the hot magnetron regime is reached with Titanium and Niobium, but for different power densities. The power value to be applied is therefore a function of the characteristics of the material to be sputtered.

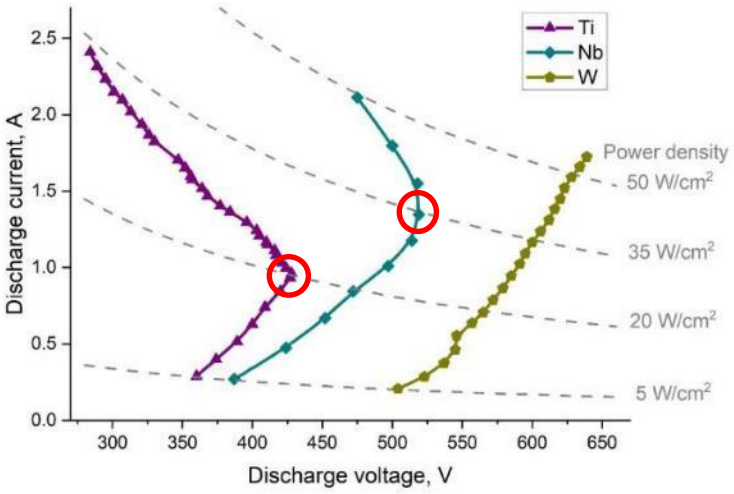

Figure 29 : Determination of the critical point value by the evolution of the discharge current as a function of the voltage for the titanium, niobium and tungsten sputtering targets.

Figure 30 shows the evolution of current and electrical voltage as a function of time, when a critical power is applied to achieve the hot magnetron regime. The heating dynamics of the target can be observed. It takes several tens of seconds before the target, and the electrical parameters of the discharge, stabilize. It should also be noted that the evolution is different for Titanium and Niobium. The stabilization time of the plasma parameters is a phenomenon that will have to be taken into account when deposition of thin films in hot magnetron regime in order to ensure that films whose properties are homogeneous over their entire thickness are obtained.

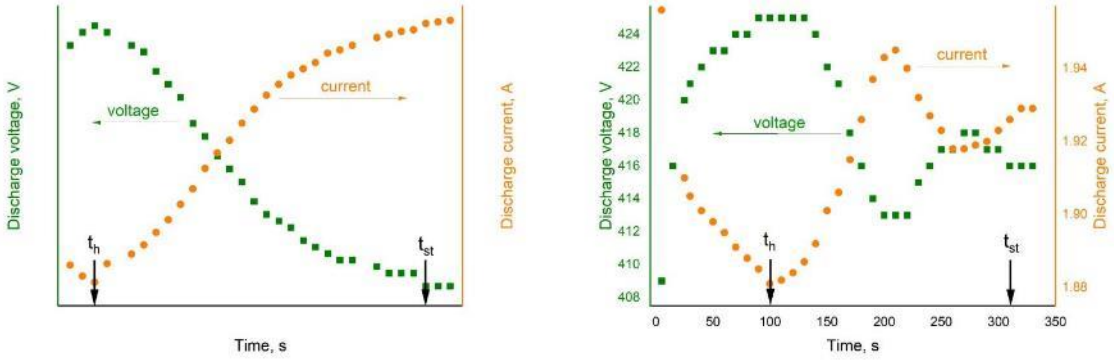

Figure 30 : Temporal evolution of current and discharge voltage for a power density of 20W/cm². At the top, titanium spray in argon (7mTorr), at the bottom, case of Niobium sputtered in argon (7mTorr) with a power density of 35 W/cm².

The time-resolved evolution of spectral line intensities and ratios of the Ar I lines are given in Figure 31, where all three cases are considered: CMS ((a) and (b)), HMS-cold, i.e. the applied power is identical to the one applied for the CMS regime ((c) and (d)), and HMS-hot, i.e., the electrical is much higher than the one applied for the CMS and HMS-cold cases ((e) and (f)).

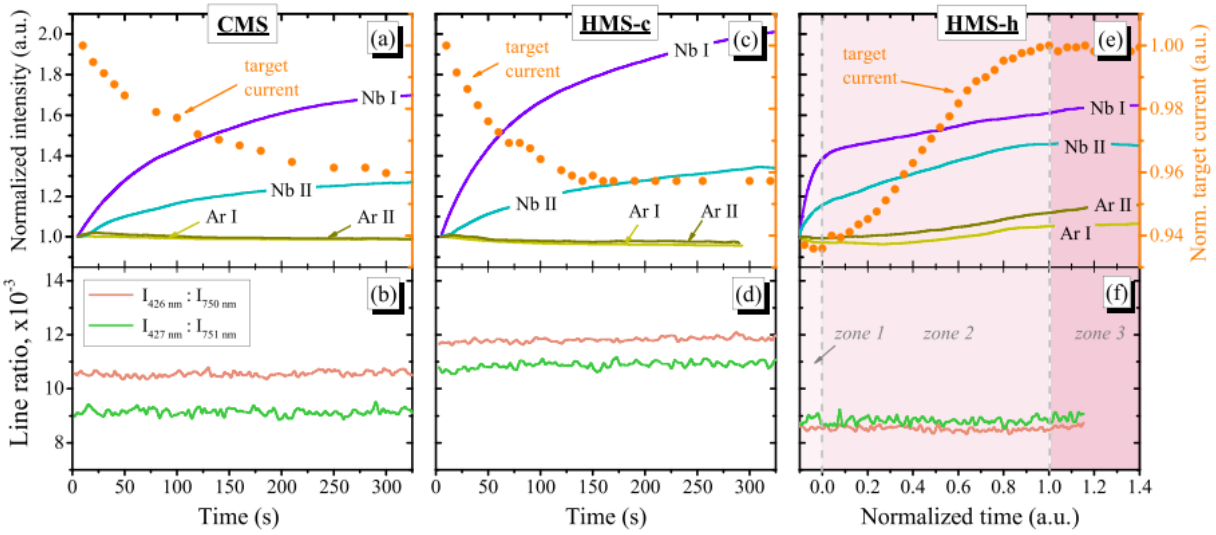

Figure 31 : Time-resolved behaviour of spectral lines of the selected plasma species and line ratios during the target heating in the CMS ((a) and (b)), the HMS-c ((c) and (d)), and the HMS-h ((e) and (f)) cases. The corresponding line ratios are given in (b), (d), (f) panels. The emission intensity was normalized by the starting value and shown in (a), (c), (e) panels. The target current in (a), (c), (e) was normalized by its highest value. The timescale in (e) and (f) was normalized in a way that '0' denotes end of the zone 1 and start of the zone 2, '1' defines end of the zone 2 and beginning of the zone 3. The Ar pressure was 7.5 mTorr (1 Pa).

In the CMS case, the target current decreases with time while the emission intensity of Nb neutrals and ions increases (Figure 31 (a)). This situation may indicate continuously growing number of the sputtered atoms and their consequent excitation and ionization due to the lower energy required for the latter process as compared to Ar species (ionization potential of Nb is 6.8 eV while it is 15.8 eV for Ar). Meanwhile, the Ar line ratio, which, in turn, reflects the electron temperature, stays constant (Figure 31 (b)). The HMS-cold case is similar to the CMS one, i.e. the emission intensities of Nb I as well as Nb II monotonously rise (Figure 31 (c)). However, the Nb I intensity increment is 15% higher than in the CMS case. Looking at Figure 31(d), it is observed that the electron temperature stays also constant. Nevertheless, in terms of its absolute values, the line ratio, and hence the electron temperature, seems to be higher in the HMS-cold case as compared to the CMS one. Thus, the sharper increase of the Nb I emission line intensity might be explained by presumably higher electron temperature rather than by higher number of sputtered atoms, i.e., deposition rates are very similar in these two cases. When the HMS-hot case is considered (Figure 31 (e)), the thermionic emission starts to make a significant contribution to the value of the target current starting from the '0' point (Figure 31 (e)). In this case, the behaviour of the emission lines cannot be interpreted explicitly because both the particle and the electron densities change distinctly over time while the electron temperature (Figure 31 (f)) remains constant. Nevertheless, the assumptions can be made in each of the defined temporal zones. The zone 1 represents the CMS-like growth of Nb species. Afterwards, once the discharge enters zone 2, the plasma composition changes as the thermionic emission increases dramatically. The most interesting effect observed here is that the growth rate of the Nb II line intensity becomes slightly higher than the growth rate linked to the Nb I. Thus, it may reflect the more efficient plasma ionization. However, the Nb I intensity increment is found to be lower than in the HMS-cold case and comparable to the CMS case. This could be caused by: (a) slight deposition of Nb on the window by that time; (b) possible self-absorption effect due to increase in a number of the sputtered Nb atoms. Meanwhile, the emission intensities of the Ar I and Ar II lines in both CMS and HMS-cold cases (Figure 31 (a) and (c)) decrease over time. This might be explained by two factors. First, as it was mentioned previously, a gas

rarefaction may take place, resulting in a decrease of Ar density and, consequently, the Ar line intensities. Second, the injection of Nb atoms in the plasma discharge facilitates the Penning ionization ($Ar_{met} + Nb \rightarrow Nb^+ + Ar + e^-$), which, in turn, results in a destruction of metastable Ar neutrals and a consequent depletion of Ar ions and excited Ar neutrals. Once the magnetron discharge is ignited in the HMS-hot case (Figure 31 (e)), the decline of Ar line intensities is still observed in zone 1. In zone 2, however, the decline is changed by the growth where the Ar II line becomes dominant over the one related to Ar I. This might be explained by increase of the electron density and, once again, may indicate a slightly higher ionization degree as compared to the CMS system. Remarkably, the spectral lines linked to other excited levels of both Ar and Nb species demonstrate the same trend, except for the lines corresponding to the lower Ground State sublevels of Nb neutrals (data not shown). Nevertheless, the line at 405.89 nm was selected to define the general behaviour of Nb I in Figure 31 for three reasons. First, there is only one possible transition from the given excited state. Second, other emission lines linked to transitions to other excited levels of Nb I (not shown in this work) demonstrate an analogous to this line behaviour. At last, the line at 405.89 nm reflects the most expected behaviour of Nb neutrals, since their amount in plasma volume has to increase in the HMS-hot case.

The target temperature was also determined by fitting the baseline of the OES spectrum in the red - NIR part of optical spectrum and by using a pyrometer (Figure 32).

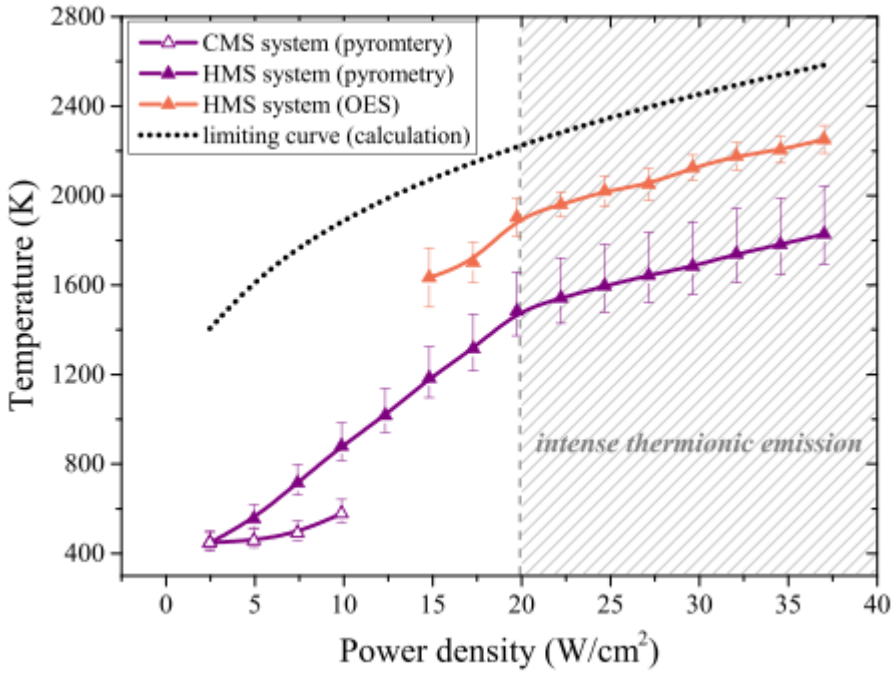

Figure 32 : Target temperature in the CMS (empty markers) and HMS (solid markers) systems as a function of power density, measured by OES-based (violet curves) and pyrometry (orange curve) methods. The black dotted curve was calculated assuming that 95% of the electrical power applied to the cathode is used for the target heating. The error bars for the pyrometry data were determined by the emissivity error (5%). The error bars for the OES-based data were determined by accuracy of the curve fitting. The Ar pressure was 7.5 mTorr (1 Pa).

In the usual Cold Magnetron Sputtering (CMS) system, it was found that the target temperature remains stable up to a power density of 5 W cm^{-2} and then starts to escalate (Figure 32, empty markers). For this reason, the use of power density above 10 W cm^{-2} is considered unsafe for the

magnets of the CMS system. In the meantime, the increase of the target temperature in the HMS system (Figure 32, solid markers) is characterized by two linear regions with a different slope. At the power densities below 20 W cm^{-2}, the temperature rises with the slope of 60 $K \cdot cm^2 W^{-1}$. Then, as soon as the intense thermionic emission is triggered, the slope becomes three times less. This is due to the fact that the emitted electrons absorb energy from the heated surface and thereby cool it down. Besides, the higher the target temperature, the greater the heat losses through the IR radiation. IR emission should be taken into account when discussing thin film deposition on the substrate because the film can be annealed in situ, during growth, and his characteristics such as morphology and crystallinity modified.

We finally studied the increase in the deposition rate as a function of the operating parameters of the sputtering plasma. In the classical CMS systems, where the deposition process occurs solely due to the target sputtering mechanism, the deposition rate increases linearly with the power. However, in the HMS systems, the behaviour changes as soon as other mechanisms, e.g. a sublimation, are involved. Figure 33 shows the evolution of the deposition rate of niobium films sputtered in argon as a function of the electric power density supplied to the magnetron cathode in hot magnetron configuration, i.e., with spacers placed under the spray target.

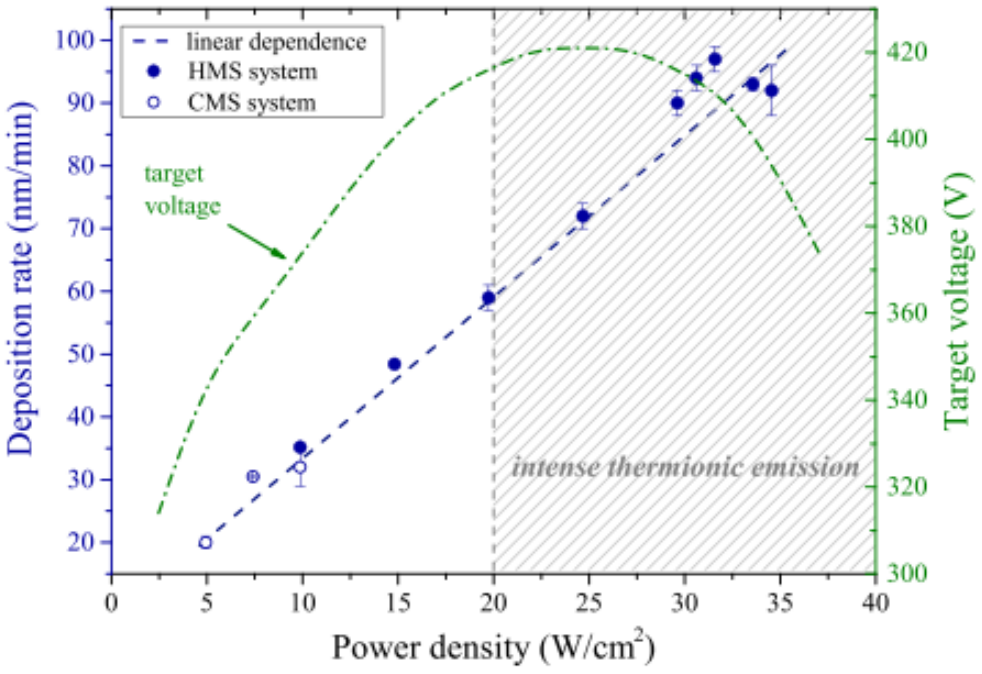

Figure 33 : Deposition rate as a function of the applied power density in the CMS (empty markers) and the HMS (solid markers) systems. The green curve denotes the target voltage evolution, emphasizing the thermionic threshold. The Ar pressure was 7.5 mTorr (1 Pa).

In this work, the deposition rate measured in the CMS system (Figure 33, empty markers) demonstrates the standard linear dependence as the power density increases, reaching its maximum at 32 nm min^{-1}. Meanwhile, when the HMS system is used (Figure 33, solid markers), the dependence continues to be linear until the power density of 27 W cm^{-2} is attained. With further increase of the applied power, the deposition rate values start to deviate from the linearity due to the high target temperature, as it was initially expected. However, the tendency changes once the power density of 32 W cm^{-2} is achieved: here and with continuous power increase, the deposition rate is saturated. This phenomenon might be caused by the enhanced thermionic emission from the target, as explained below. Due to intense thermionic emission, the number of electrons in the confined discharge area

significantly increases, a large part of which does not contribute to the sputtering mechanism. Furthermore, as the current increases, the voltage decreases correspondingly (Figure 33, green curve) and the plasma positive ions bombarding the target have less kinetic energy. The sputtering yield, which directly depends on the ion kinetic energy, is therefore reduced. Thus, at high power density, i.e., high target temperature, when no considerable evaporation or sublimation of Nb takes place, the deposition rate is saturated with the applied power.

In the second part of the work, the knowledge gained about plasma behaviour was used to deposit thin films of Niobium with an argon plasma in several distinct operating regimes. Six Nb coatings were deposited using two different magnetron configurations. The first system (CMS) represents classical cold-target magnetron sputtering, when a sputter target is firmly attached to a water-cooled magnetron cathode. In this configuration only one Nb coating was deposited (the sample "1-CMS", see Table 5). The second system (HMS) represents hot-target magnetron sputtering, when a sputter target is thermally insulated from the water-cooled cathode and the target is heated up while the plasma is on. In this system other five samples were prepared ("2-HMS-c" – "6-HMS-7").

- The coatings "1-CMS" and "2-HMS-c" were deposited at the same power, roughly same deposition rate but using different configuration, i.e., at different target temperature.
- The coating "3-HMS-h" was deposited at three times higher power, 2.5 times higher deposition rate and two times higher target temperature than in the "1-CMS" case.
- The coatings "4-HMS-3", "4-HMS-3", and "4-HMS-3" were deposited at the same power, same target temperature but using different deposition times.

Prior to each deposition all substrates were cleaned by RBS 25 and isopropanol.

The film thickness was measured using SEM. The oxygen fraction was determined by EDX technique. The electrical conductivity was estimated by four-point probe method. The impurity flux was calculated based on the residual pressure. The target temperature was measured using Planck's law and pyrometry (see above). The cross-section and topology were prepared by SEM (see Table 5).

Table 5: Deposition conditions for the Nb films

Samples						Deposition conditions						
Name	Substrate	Coating	Thickness, nm	O, atom %	El. Conductivity, $x10^6$ S/m	Base pressure, $x10^{-7}$ Torr	Impurity flux, $x10^{14}$ particles/cm^{2}s	Power density, W/cm^2	Target temperature, K	Working pressure, mTorr	Distance, cm	Deposition rate, nm/min
1-CMS	Silicon <100>	Nb	499±11	9±3	2.53±0.02	5	3.78	10	~ 1000	7.5	11	33±1
2-HMS-c			535±7	9±3	2.50±0.02	4.2	3.17	10	~ 1300			35±1
3-HMS-h			470±23	8±2	4.80±0.02	7	5.29	30	~ 2100			82±4
4-700-3			327±11	8±2	3.04±0.02	4.9	3.7	35	~ 2200			109±4
5-700-5			453±19	8±2	4.37±0.03	2	1.51	35	~ 2200			91±4
6-700-7			616±39	8±2	4.68±0.06	3.4	2.57	35	~ 2200			88±6

From the images of the film cross sections presented in Figure 34 and the image of the film topography presented in Figure 35, it is quite clear that the depositing the film I nHMS-hot regime significantly changes the film microstructure as compared to the film grown in CMS and HMS-cold deposition conditions. The film deposited in the two latter conditions are very similar. The above observation is related to the plasma properties (see OES data) which are quite different for the HMS – hot conditions as compared to the CMS an HMS-cold conditions.

1-CMS	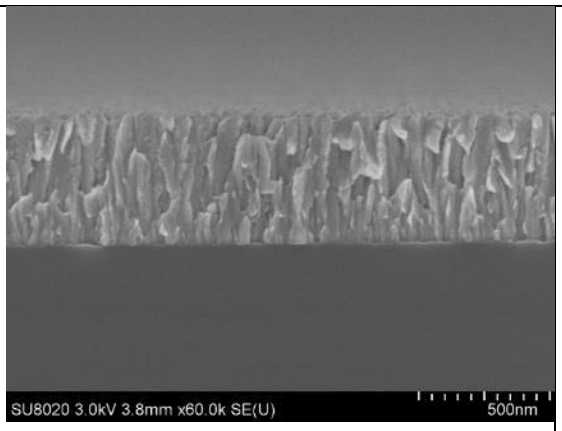	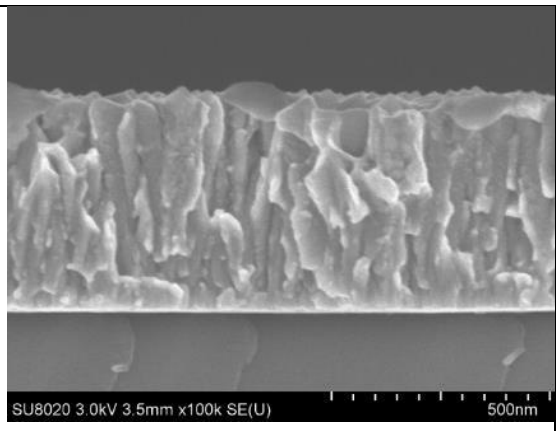
2-HMS-cold	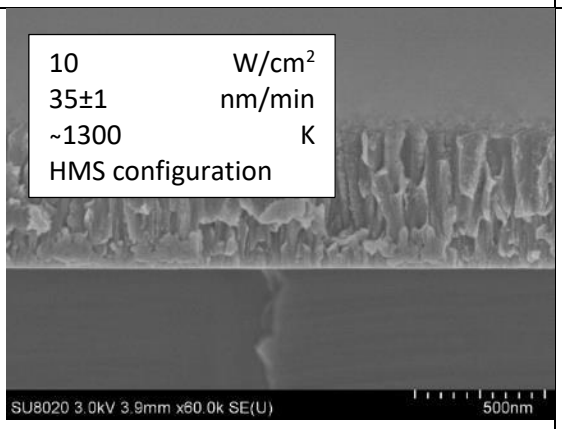	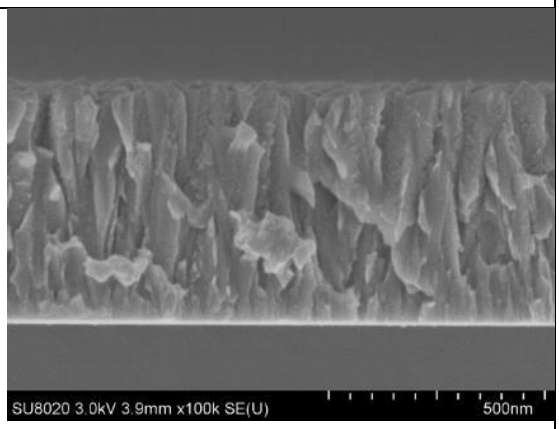
3-HMS-hot	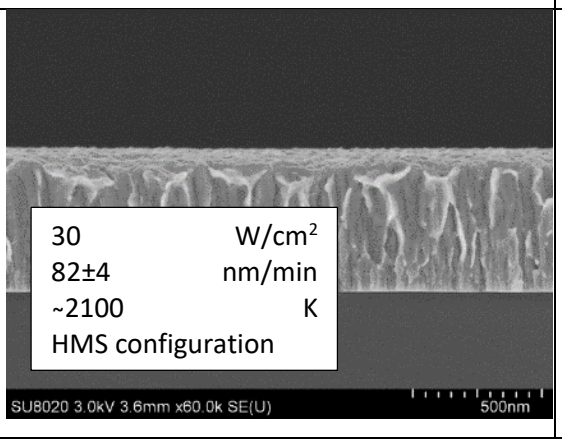	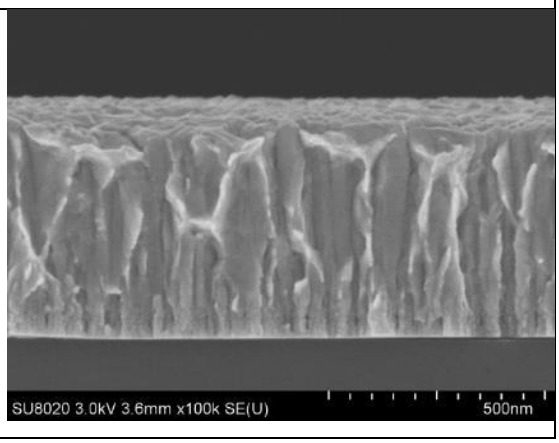

4-700-3	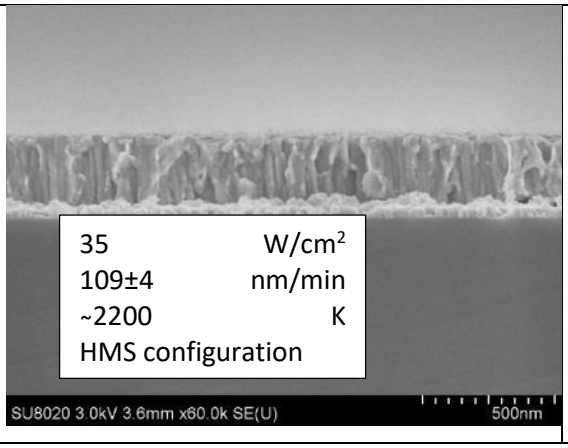	

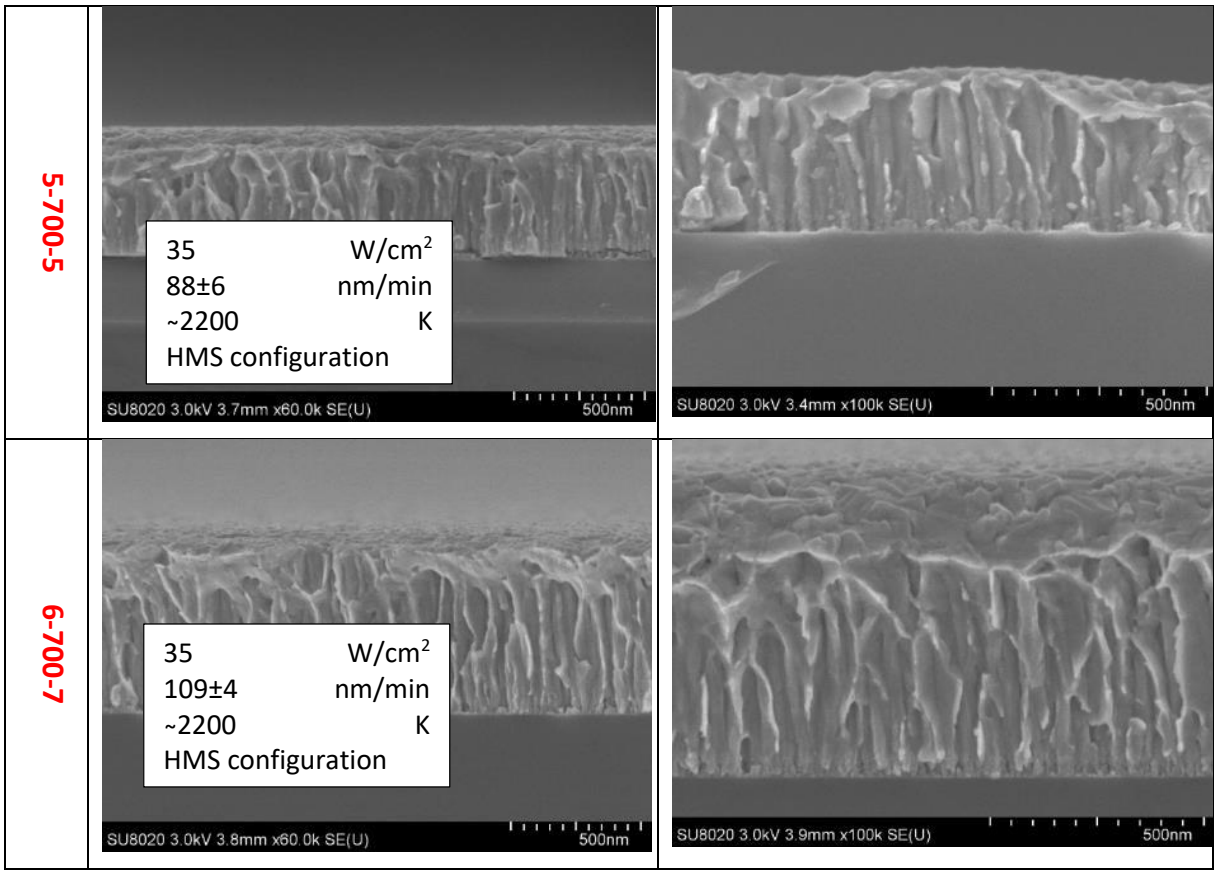

Figure 34 : Cross sectional Scanning Electron Microscopy images of the various Nb thin films.

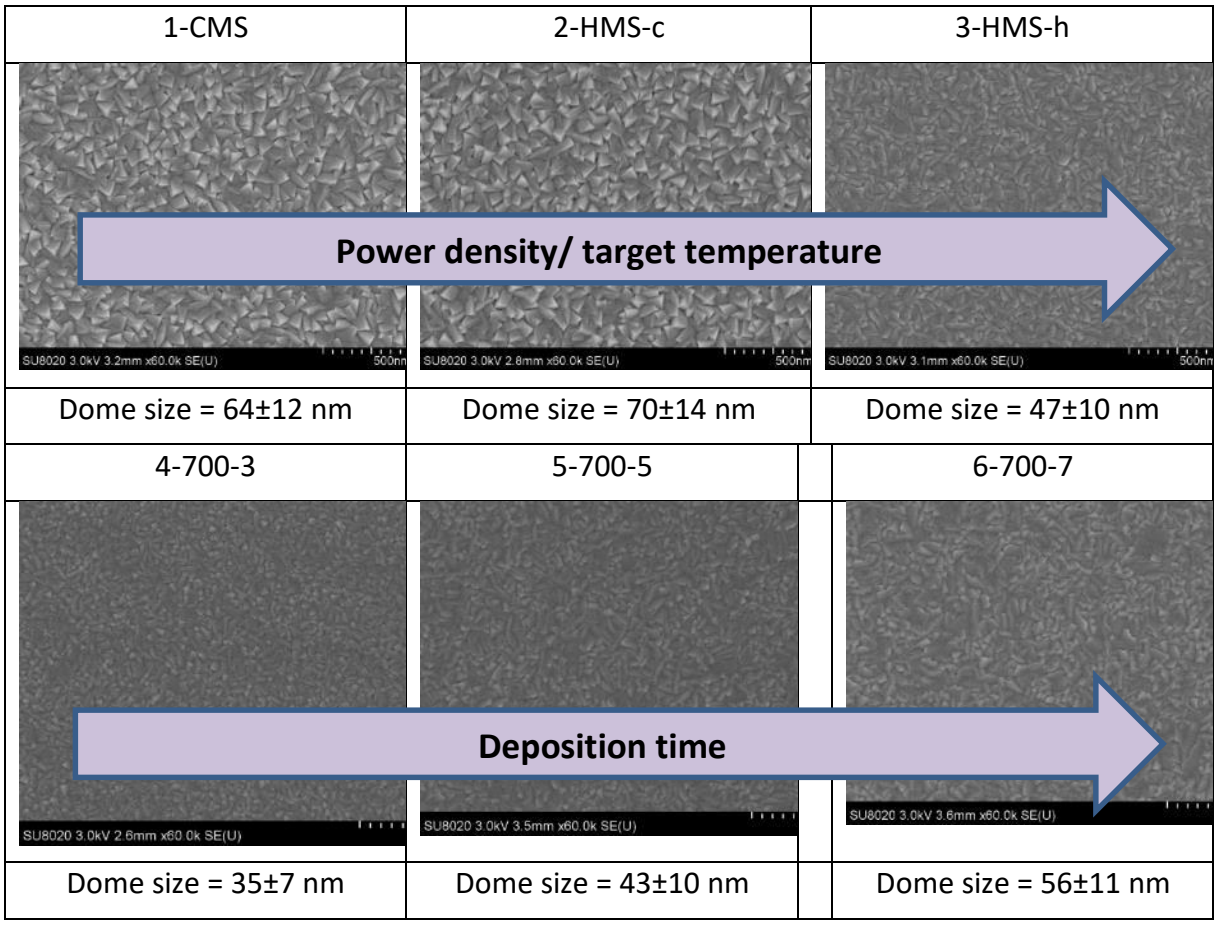

Figure 35 : Evolution of the Nb film surface topography as a function of the deposition conditions: (top) as a function of the applied power and sputter target temperature, (bottom) as a

function of the deposition time in the case of the HMS-hot condition i.e., with 35 W/cm^2 of applied power density.

3.1.3.4 Performed activities – Materia Nova (II)

Optimization of the coatings on powders by hot magnetron

- Experimental process

Magnetron sputtering is one of the most widely used methods for thin film deposition. It can be utilized to manufacture nearly every metal coating or metal composite as well as nitride or oxide layers, thus making magnetron sputtering a most versatile coating method. The possibility to coat large area substrates and the easy-to-handle process parameters of magnetron sputtering able a wide range of industrially important applications. Although coating plane substrates is state of the art, coating powder-substrates, granulates and particles of approximately 2–600 µm diameter by magnetron sputtering is still a more difficult task. This is due to: (i) Each side of every single particle must be exposed to the sputter beam in order to get coated uniformly; therefore, a particle mixing, or rotating mechanism is necessary. (ii) Small particles of different sizes and shapes become wedged together during the mixing process which prohibits most of the particles from being coated since they are not exposed to the sputtering beam. And (iii), in vacuum the particles tend to stick together as coating proceeds, especially when the powder is coated with pure metal, because of the lack of any separation layer between the coating of two particles in contact, i.e. air, water film or an oxide layer. Rotary plasma reactor is presented below. To overcome these issues there are several approaches, such as:

- Adapted rotating drum, where the axis of rotation is horizontal and the barrel can be shaped in different ways, e.g., circular with inlets, hexagonal or conical, and the targets are positioned within the drum or perpendicular to the drum.
- Vibration, where the sample stage is connected to an ultrasonic or electromagnetic vibration generator which keeps the particles tumbling.
- Tilted rotating vessels, which also can be of different shapes.

At MaNo, to vibrate the powder, a mechanical shock was applied to the rotating drum during the deposition. For this application, a *Home Concrete Vibrators* was used. Figure 36 shows the main part of the barrel-sputtering system. A barrel was placed in the vacuum chamber to hold powdery materials. The barrel could be rotated using a motor drive at different speed during sputtering, thus making it possible for the powdery particles to be agitated.

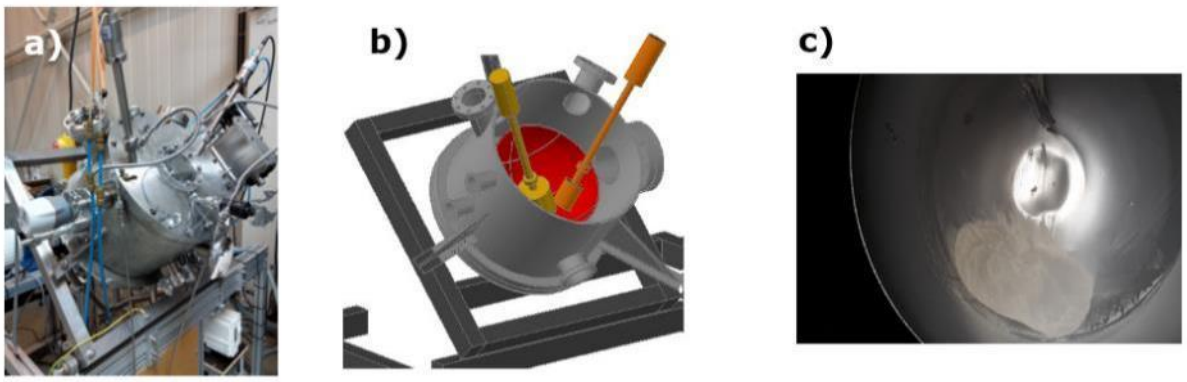

Figure 36: a) Rotary plasma reactor b) Reactor schematic view and c) Powder in the "bowl"

For this work, we adapted several times the powder stirring system. A metal rod turns very fast in a tube and induces a vibration with a drilling machine. The result is presented in Figure 37.

Figure 37: Reactor with Home Concrete Vibrators.

A new reactor was built from the MaNo experiment: abbeads 2 (see Figure 38).

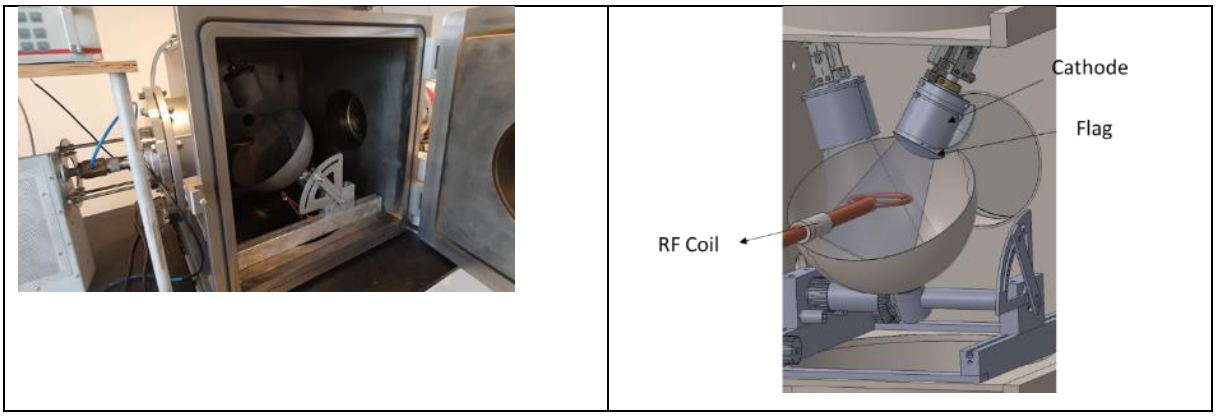

Figure 38: New Reactor abbeads 2 with Home Concrete Vibrators and RF coil.

- Hot Sputtering

In the magnetron sputtering, deposition rates are limited by the ion current on the cathode due to the existence only a sputtering mechanism of the target erosion. Thus, the addition of the target evaporation as the second mechanism of the cathode erosion doesn't have alternatives to the increase of the deposition rates. It can be realized in liquid phase or hot target magnetrons. There are three potential mechanisms of enhanced deposition rates: a particle-induced erosion, a sputtering yield increase and the target evaporation (or sublimation). This aspect was studied by Umons. For target, the magnetron sputtering system with indirect cooling and the special geometry with voids were used (Figure 39).

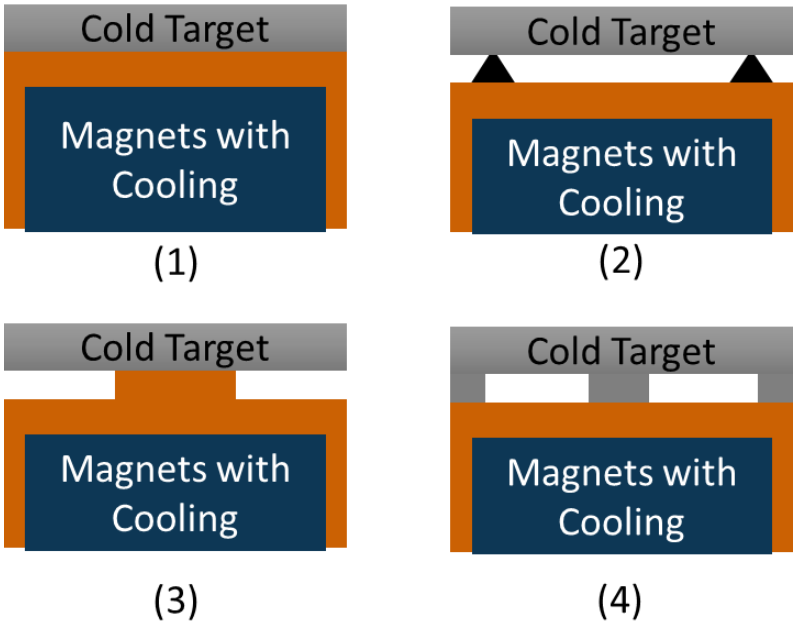

Figure 39: Systems with heat conductive contact between the target and cooled magnetron

(1) Complete cooling: the target has a good heat-conducting contact with the magnet system. The latter should be intensively cooled during the magnetron operation. Therefore, the target is not heated to a high temperature by the action of plasma.

If the heat conductive sink from the target is limited, the temperature can be very high:

(2) complete heat insulation, (3) and (4) partial heat presents some schemes of the target thermal insulation from the coolable elements of the cathode assembly (i.e. magnetron body).

Figure 40 shows the complete heat insulation used at Materia Nova/Umons.

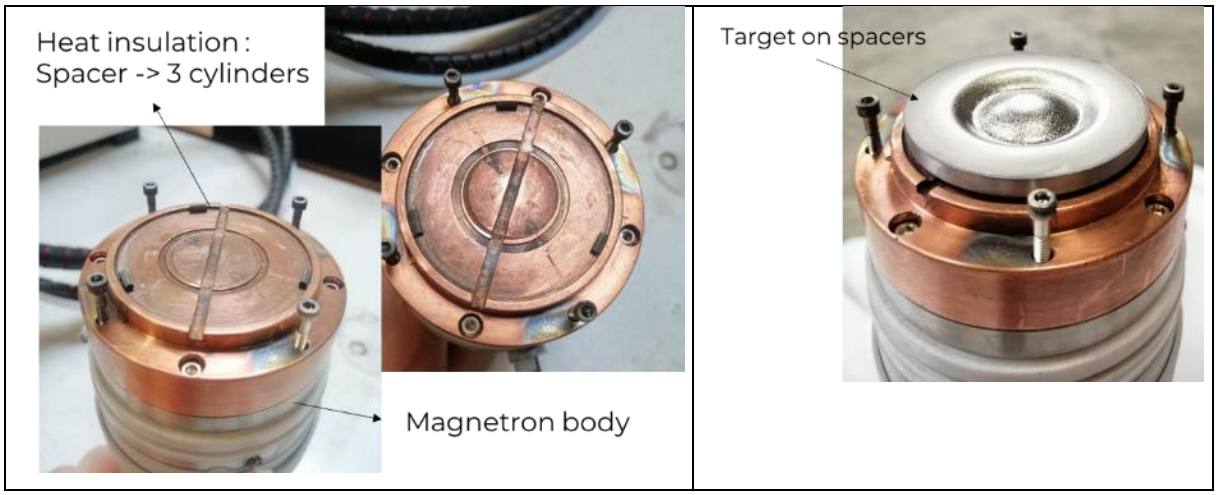

Figure 40: Complete heat insulation used at Materia Nova/Umons

The hot and cold cathode were evaluated on the abbeads deposition chamber. Figure 41 shows a plasma with a target of Ti at 200 W with 100% Ar for each cathode.

Cold magnetron sputtering system	Hot magnetron sputtering system	
 (a)	 (b)	 (c)

Figure 41: Cold and hot magnetron sputtering system. a) Emitted blue light from Ar species in the plasma b) Red light emitted from the target at high temperature c) Red light emitted from the target at high temperature after switching off (without plasma) can be observed.

Plasmas in the hot-sputtering configuration were fired for 15 min at high power (700 W instead of the standard 200 W). The surface of the targets was then observed (see Figure 42). The surface condition of the Nb and Ti targets appears to have melted after plasma. The Cr appears to have sublimated and the W sputtered.

Temp.(°C) for Given Vap. Press. (Torr)			
10^{-8}	10^{-6}	10^{-4}	Atm (M.P.)
2117	2407	2757	3410

W

Temp.(°C) for Given Vap. Press. (Torr)			
10^{-8}	10^{-6}	10^{-4}	Atm (M.P.)
1728	1977	2287	2477

Nb

W

Nb

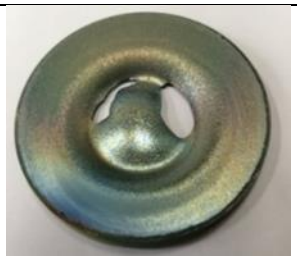

Cr

Ti

Temp.(°C) for Given Vap. Press. (Torr)			
10^{-8}	10^{-6}	10^{-4}	Atm (M.P.)
837	977	1157	1857

Cr

Temp.(°C) for Given Vap. Press. (Torr)			
10^{-8}	10^{-6}	10^{-4}	Atm (M.P.)
1067	1235	1453	1660

Ti

Figure 42: Target surface after sputtering with Hot magnetron: 35 W/cm2 (700 W) – 5mTorr

- Deposition rate

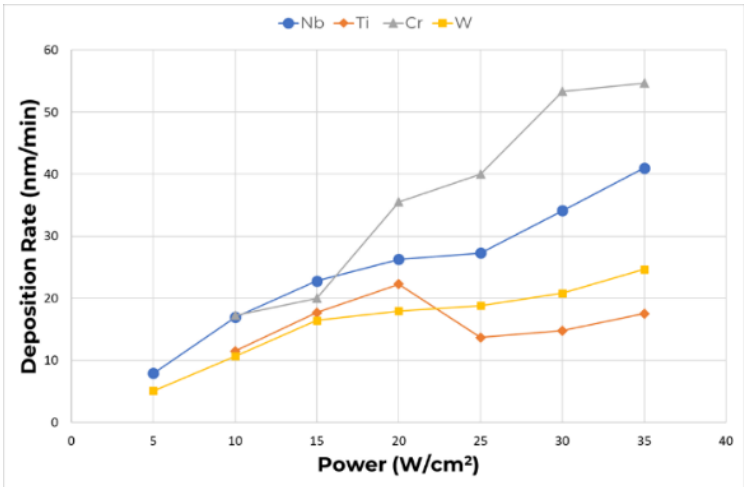

Figure 43: Deposition rate evolution from Nb, Ti, Cr and W targets

The deposition rate increases with power. There is no evaporation effect and consequently an exponential increase in the deposition rate (see graph in Figure 44).

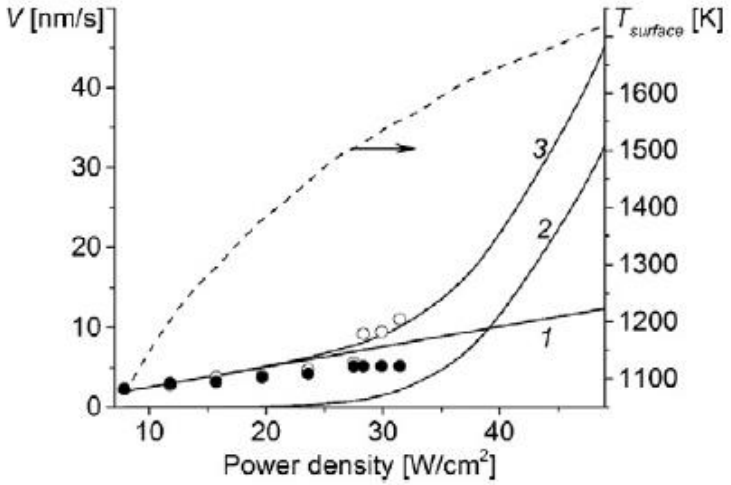

Fig. 2. Deposition rates of Cr coatings (points and solid lines) and surface temperature $T_{surface}$ (dashed line) of hot Cr target as a function of Q: ○ – hot target (exp.); ● – cooled target (exp.); 1 – by sputtering (calc.); 2 – by evaporation (calc.); 3 – by total erosion (calc.).

Figure 44: Deposition rate evolution from Nb, Ti, Cr and W targets [37]

- Thin films deposition

Deposits were made by hot/cold sputtering and observed by electron microscopy (see Figure 45). There is no significant difference in the morphology of the films. They are columnar and the Ti film in hot sputtering seems more porous.

	10 W/cm2 (Cold)	35 W/cm2 (Hot)
W	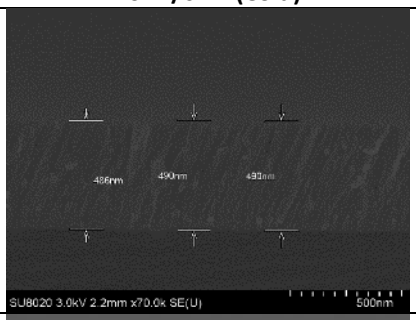	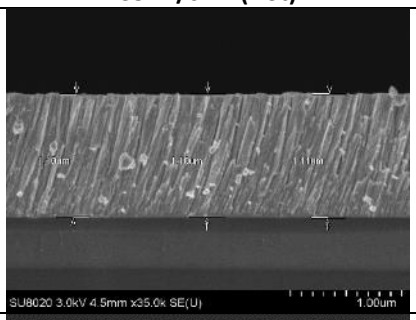
Nb		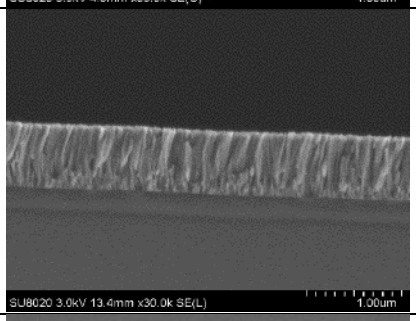
Ti	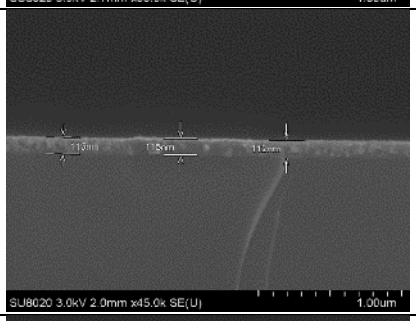	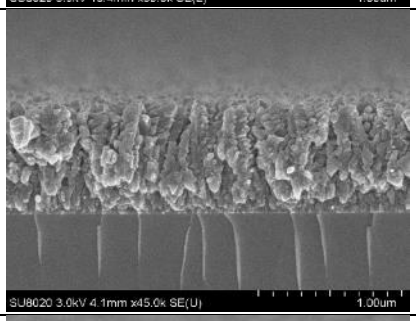
Cr	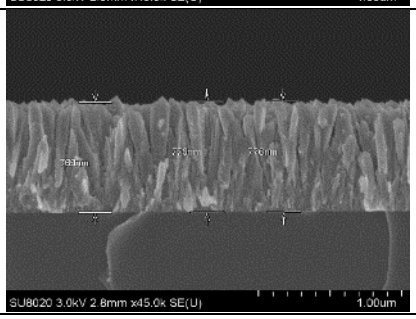	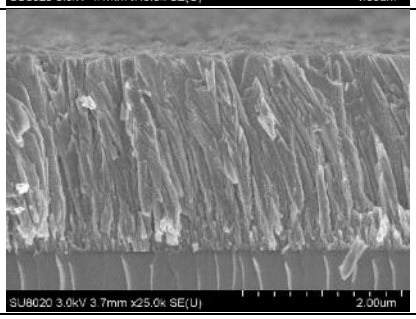

Figure 45: Deposits made by hot/cold sputtering

- Nb coating on Cu powder to obtain 1% wt

Deposits of Nb on copper powders by hot sputtering for fem are presented in Figure 46 and Figure 47.

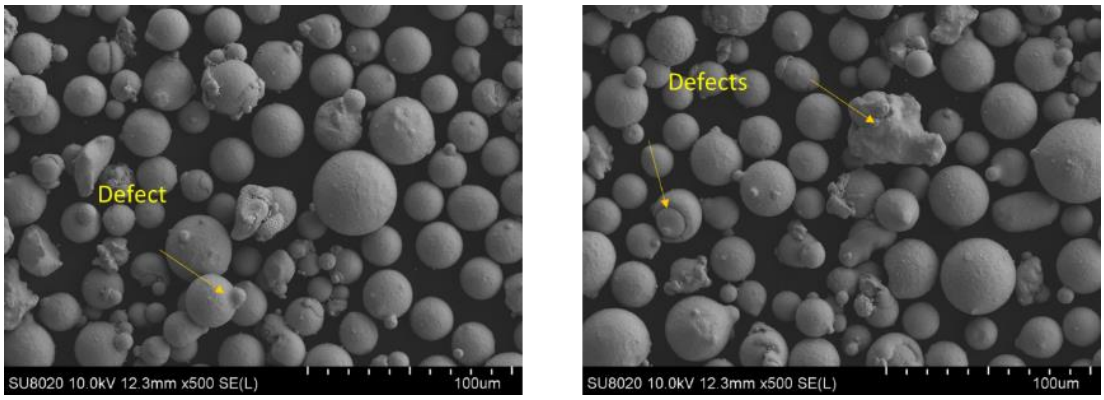

Figure 46: SEM images of surface of Cu powder with Nb coatings

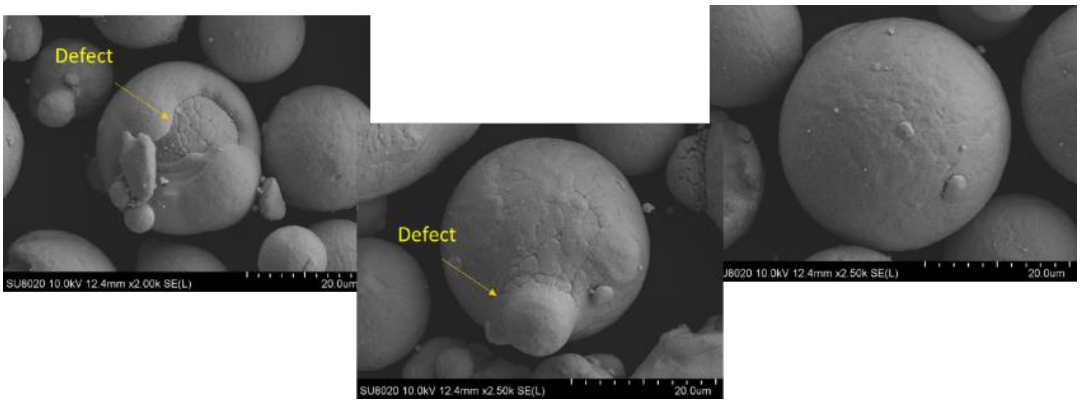

Figure 47: SEM images of surface of Cu powder with Nb coatings

SEM images of cross section of Cu powder with Nb coatings are presented in Figure 48.

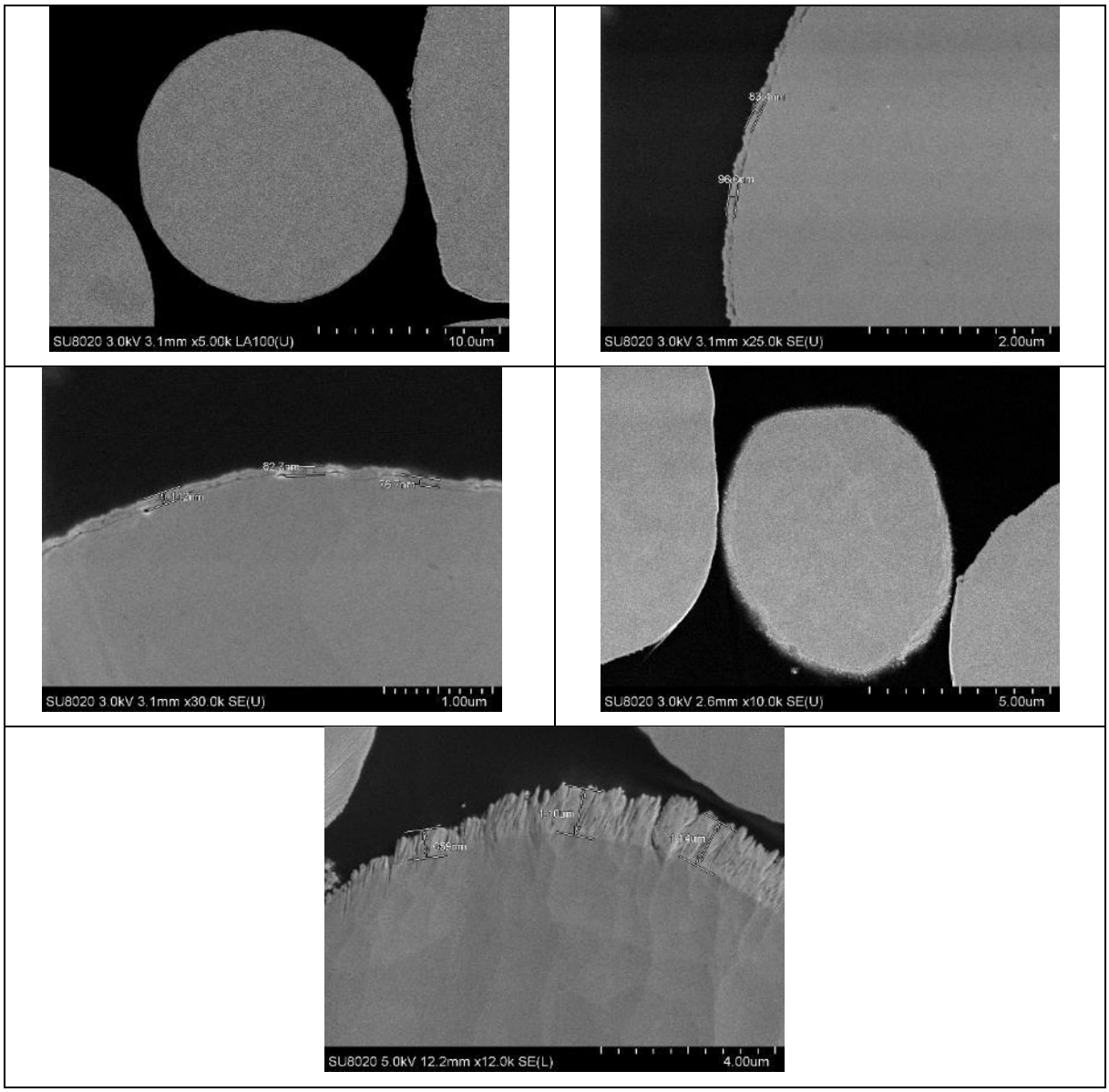

Figure 48: SEM images of cross section of Cu powder with Nb coating

SEM/EDX images of the surface and of the cross section of Cu powder with Nb coatings are presented in Figure 49 and Figure 50. The coating seems uniform but oxygen on the surface seems to be high.

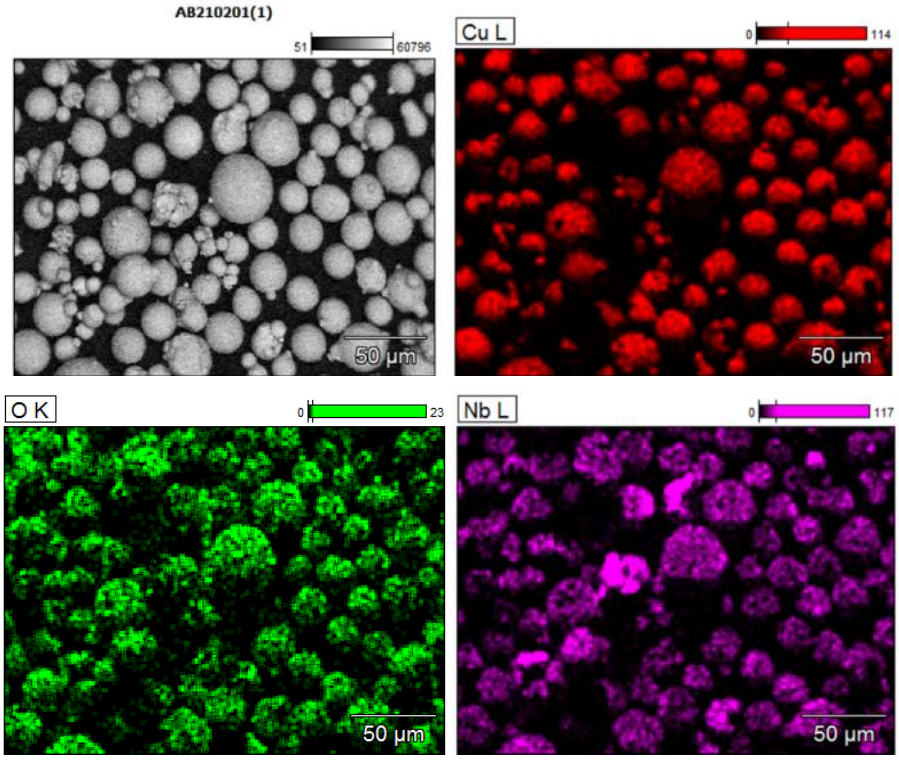

Figure 49: SEM/EDX images of surface of Cu powder with Nb coatings

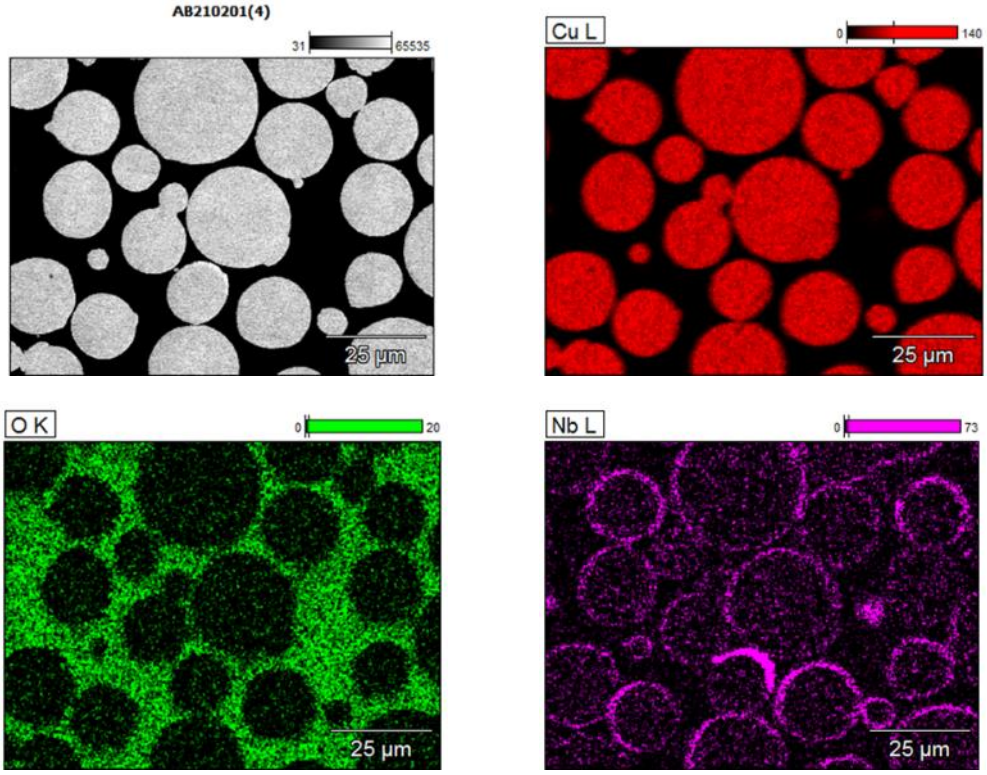

Figure 50: SEM/EDX images of cross section of Cu powder with Nb coatings

- Conclusions

The study of hot sputtering on powders leads to the following conclusions:

- the design of the cooling system allows hot sputtering.

- hot sputtering allows to work at higher powers and thus to increase the speed of deposition.

- the heating of the target increases the temperature of the walls of the chamber and thus the oxygen content in the films

Coated powder for partners -MaNo

In this task, different metallic depositions were realized on metallic powders.

- For copper powder, deposition of Cr, W, Ta, Nb and Mo on the copper alloys Cu, CuCrZr, CuNiSiCr (see results WP4)
- For aluminium, deposition of Zr, Ti, B, Mg on the aluminium alloys Al 7075, AlCu4MgTi and Al 7020 (see results WP3).

3.1.3.5 Performed activities – fem

- Processing of flat substrates after the coatings by magnetron sputtering
- Investigation of laser tracks width and depth
- Characterization of uncoated and PVD-coated powders (CuNiSiCr, CuCrZr, said alloys coated with Nb / Cr, pure Cu coated with W): morphology, coating thickness, chemical composition and oxygen content, XRD analysis

Sheets of four different materials (pure Cu, CuCrZr, CuNiSiCr and CuNiAl alloy) were coated with five different elements (Cr, Mo, Nb, Ta, W) by PVD in cold-rolled condition at Materia Nova in Belgium and made available to fem (see Figure 51). A total of 24 metal sheets was available for laser exposure. The plates were exposed at fem with 95 W power according to the specified pattern (see WP1) in the LPBF system and then examined.

The surface was examined in the light microscope to measure the track widths produced: the measurement was made at five specified points per track (see Figure 52b-h). No laser tracks were present on the uncoated pure Cu and CuCrZr sheets with 95 W power (see Figure 52a-b). The Nb coating on these two materials allowed laser tracks with a width of 60-80 µm to be produced (Figure 52c-d), which could also be measured on the CuNiSiCr sheet coated with Cr (Figure 52e). Similar track widths were also achieved with the uncoated CuNiAl sheet (Figure 52f), which showed a higher absorption of the laser energy than the other uncoated substrates. The respective Cr, Nb, and Ta coatings on the CuNiAl alloy didn't offer a marked improvement to the track width in comparison to the uncoated material (Figure 52g). On the other hand, the W coating sometimes resulted in higher and non-uniform track widths (up to 200 µm), due to an occasional higher laser coupling (Figure 52h).

The measured values were evaluated in graphs to compare the influence of different coating elements. The elements Cr, W and Nb always showed a positive effect on the formation of the track width compared to all uncoated materials (see Figure 54 to Figure 56). In the case of the CuNiAl alloy, the W coating exhibited at lower laser speeds (50-100 mm/s) much higher track widths compared to the other elements (see Figure 57).
The light reflectance of the sheets was measured at 740 nm wavelength. The coated surfaces exhibited approximately half the reduced reflectance (value 40-45%) compared to the pristine substrates (value 70-80% - see Figure 53).

SEM examination was performed on selected cross sections of individual laser tracks to measure their depth. CuCrZr and CuNiSiCr (each with Nb and Cr coating) reach depths between 20 µm and 30 µm (see Figure 58a), which were also measured for the uncoated CuNiAl sheet, and feature a conduction mode (with its circular segment shape). The W-coated CuNiAl sheet reached values of depth which are in a different order of magnitude (100 - 160 µm – see Figure 58b), and feature a keyhole mode (with its typical shape). The chart in Figure 59 shows a comparison of the measured values.
SEM examination of the track cross section on CuNiAl sheet coated with W showed good mixing of the W throughout the melted laser track, and fine precipitates distributed in the Cu-matrix could be documented (see Figure 60a). Said precipitates could also be observed for the CuNiSiCr sheet coated with Cr (see Figure 60b). This is consistent with the research approach (coating of a substrate with a non-mixable element and alloy formation and precipitation during the LPBF process).
The experiments proved that the coatings have a positive effect on the energy absorption. The CuNiAl alloy exhibited higher coupling compared to all other substrates. The elements Cr, Nb and W were considered to be the most suitable candidates for powder coating.

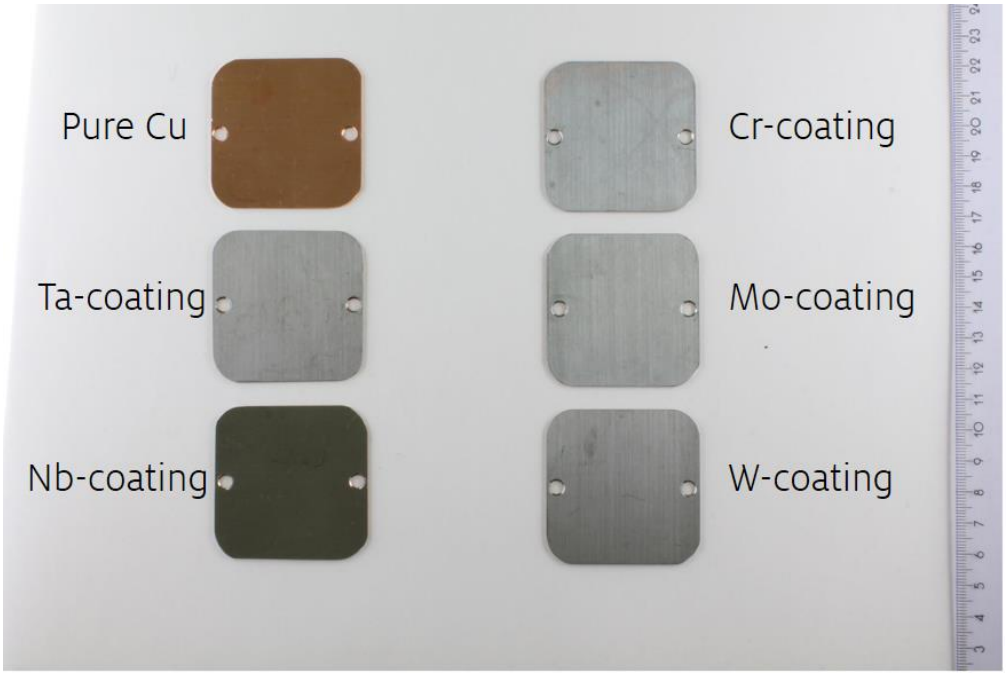

Figure 51: Example of PVD-coatings on pure Cu plates

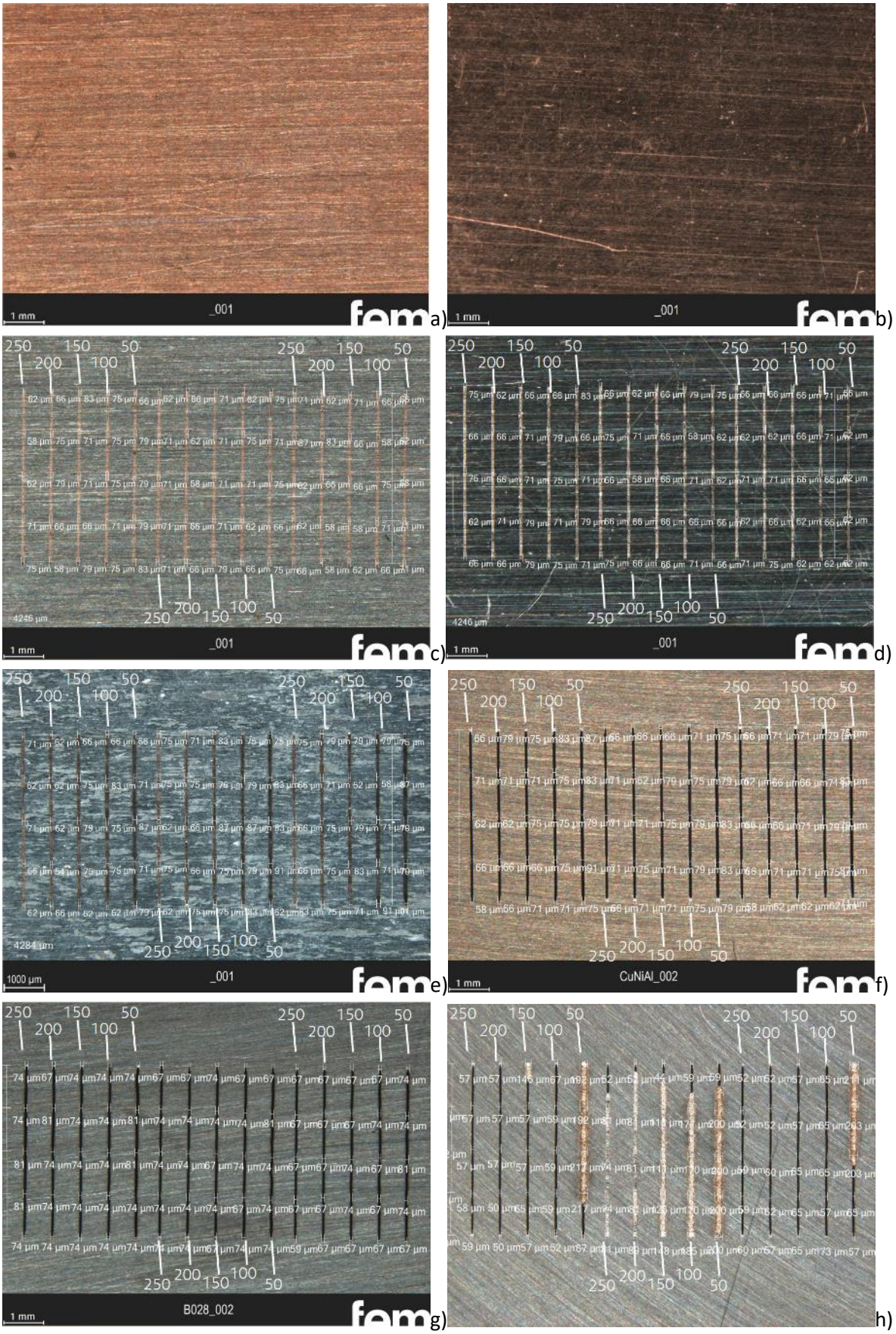

Figure 52: Examples of the measurement of the track widths on coated and uncoated sheets a) Pure Cu sheet (uncoated) b) CuCrZr (uncoated) c) PureCu + Nb d) CuCrZr + Nb e) CuNiSiCr + Cr f) CuNiAl (uncoated) g) CuNiAl + Nb h) CuNiAl + W

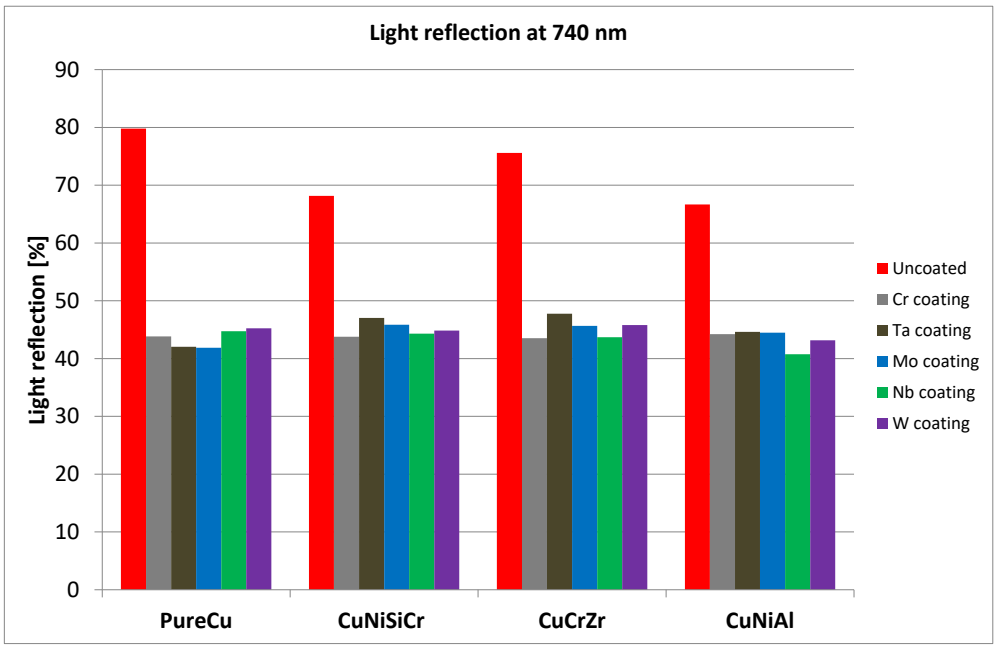

Figure 53: Measured light reflection at 740 nm for the uncoated and coated alloys

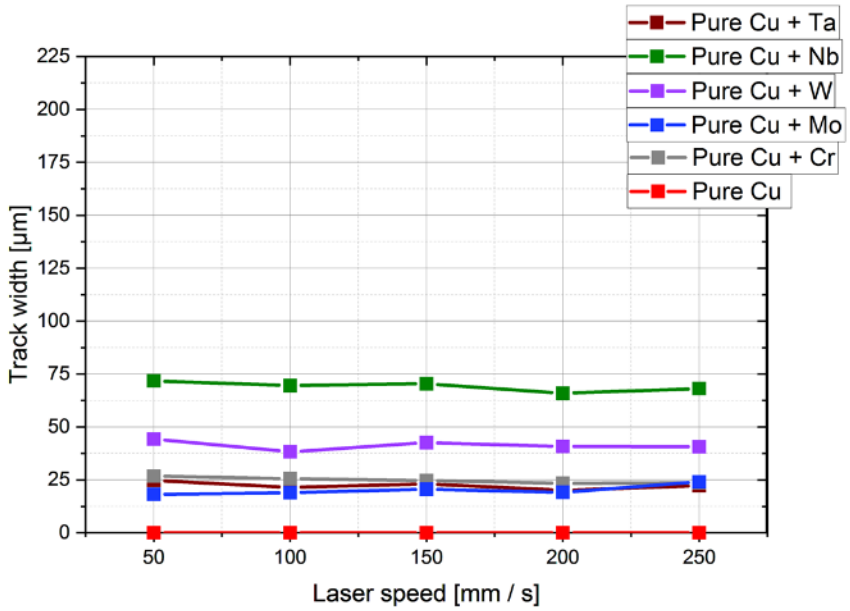

Figure 54: Measured track widths on pure Cu sheet with different coatings

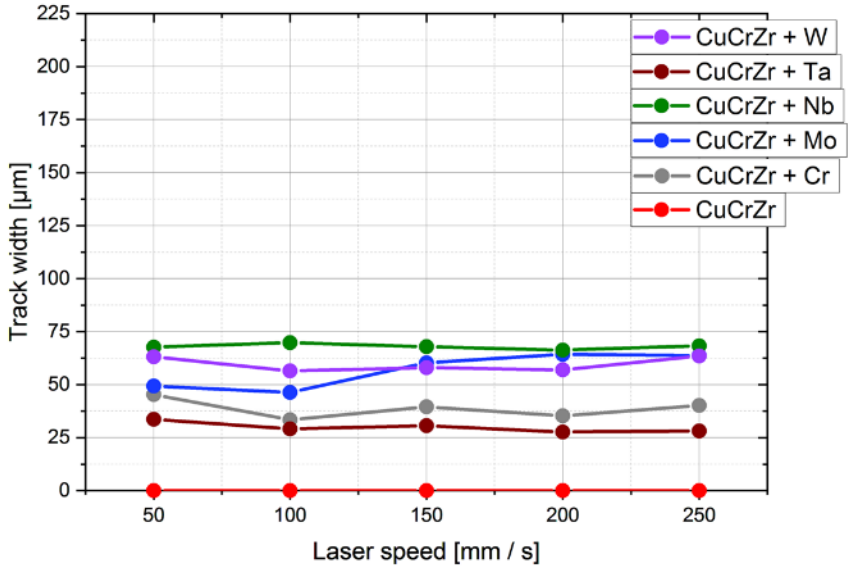

Figure 55: Measured track widths on CuCrZr sheet with different coatings

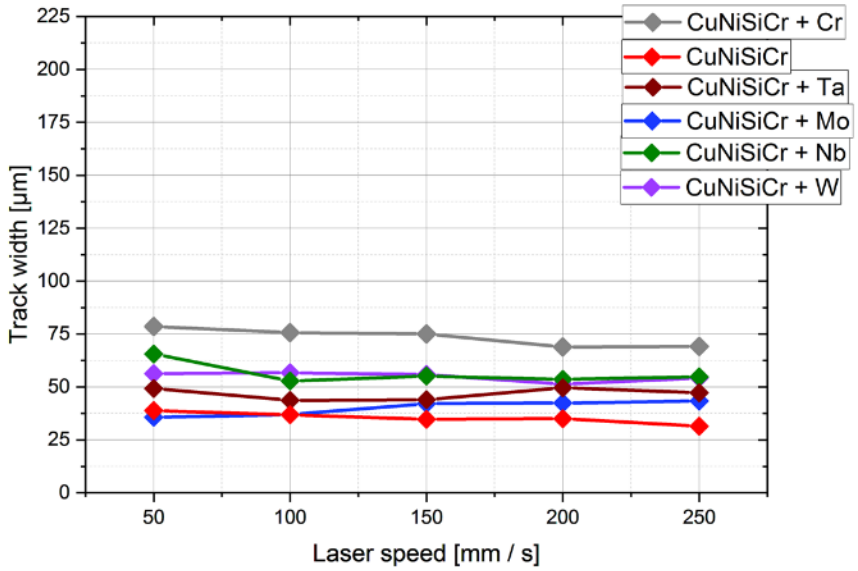

Figure 56: Measured track widths on CuNiSiCr sheet with different coatings

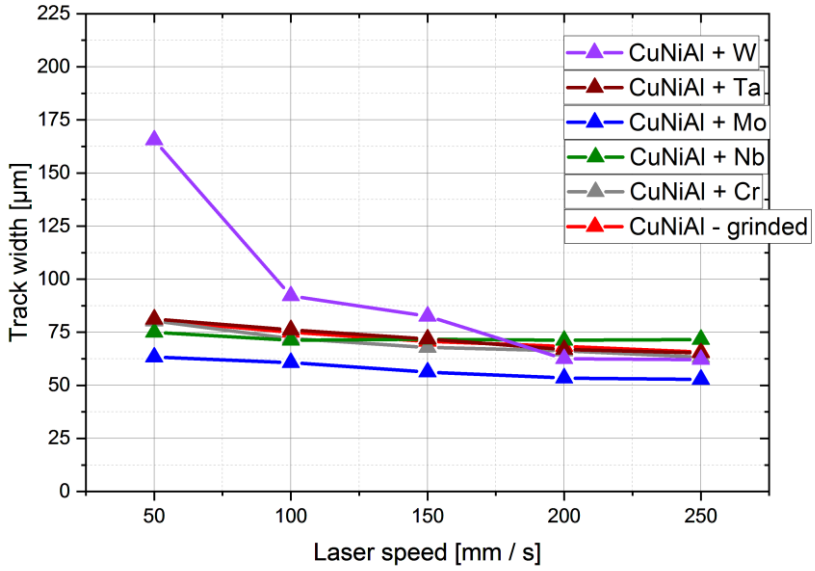

Figure 57: Measured track widths on CuNiAl sheet with different coatings

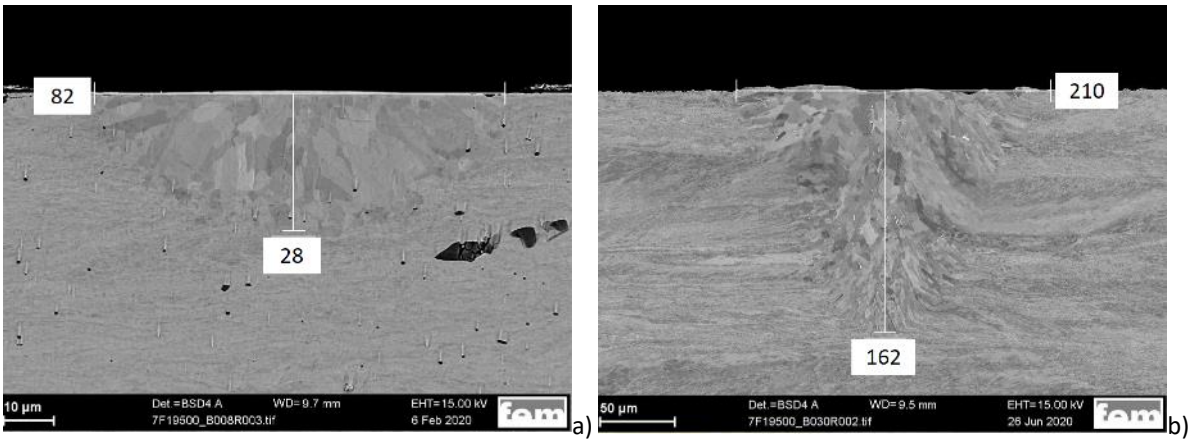

a) b)

Figure 58: SEM investigation of molten laser tracks in cross section (Laser parameters 95 W - 50 mm/s) - a) CuNiSiCr + Cr / b) CuNiAl + W

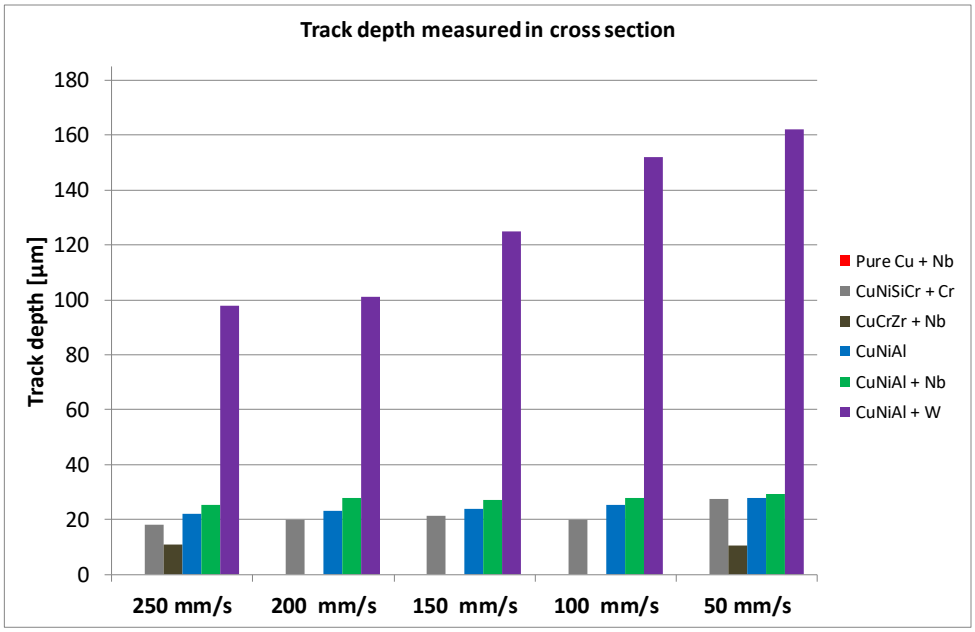

Figure 59: Measurement of the track depth on the SEM for selected samples.

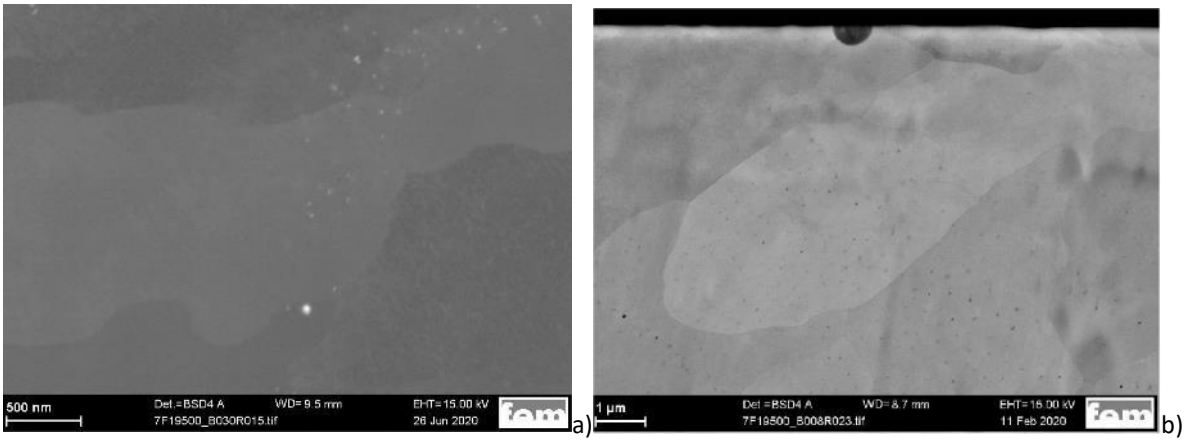

a) b)

Figure 60: SEM investigation on metallographic samples of LPBF processed coated sheets - Fine precipitates distributes in the Cu-matrix in the molten laser track a) CuNiAl sheet coated with W b) CuNiSiCr sheet coated with Cr

The elements Cr, Nb and W, due to their beneficial effect on the energy absorption and to the observed formation of precipitates in the microstructure, were found to be the most suitable candidates for powder coating. Concerning the substrates, it was decided to focus the attention on the CuCrZr and CuNiSiCr alloys, which were commercially available in powder form (and were provided by the industry partner Schmelzmetall), and pure Cu (which was atomized at Umsicht).

Table 6: Results of powder characterization at the fem

Alloy	Oxygen content (ppm)	Coating element	%wt of element already in the alloy	%wt of element after PVD coating	Coating Thickness (nm)	XRD Analysis
CuNiSiCr	50	-	-	-	-	-
CuNiSiCr + Cr	770	Cr	0,35	1,52	~100	metallic Cr
CuNiSiCr + Nb	2700	Nb	-	1,05	~60	metallic Nb + intermetallic phase $Cr_4Nb_2Si_5$
CuCrZr	120	-	-	-	-	-
CuCrZr + Cr	710	Cr	0,66	0,85	~40	-
CuCrZr + Nb	2800	Nb	-	1,94	~160	metallic Nb
Pure Cu + W	2100	W	-	1,87	~55	metallic W

The CuCrZr and CuNiSiCr powders (in coated and uncoated state) were characterized at fem. The pure Cu powder was not available in its uncoated form, so only the W-coated one was investigated. The morphology was investigated by SEM (with the additional use of FIB cut of the powder grains, to establish the coating thickness), while ICP analysis and hot gas extraction were used to determine the chemical composition and the Nb and O contents, respectively. In addition, XRD measurements of the

CuCrZr and CuNiSiCr coated powders were carried out. The results of the investigations are summarized in Table 6. The oxygen content of the untreated CuNiSiCr and CuCrZr powder (50 ppm and 120 ppm respectively) was significantly increased by the coating. The increased O content in the material occurs after PVD treatment, since the powder has a large surface area and can absorb a high amount of oxygen. This oxidation is difficult to prevent. The XRD measurements on the powders however confirmed the presence of the elements Nb, Cr and W in their metallic form (see Table 6).

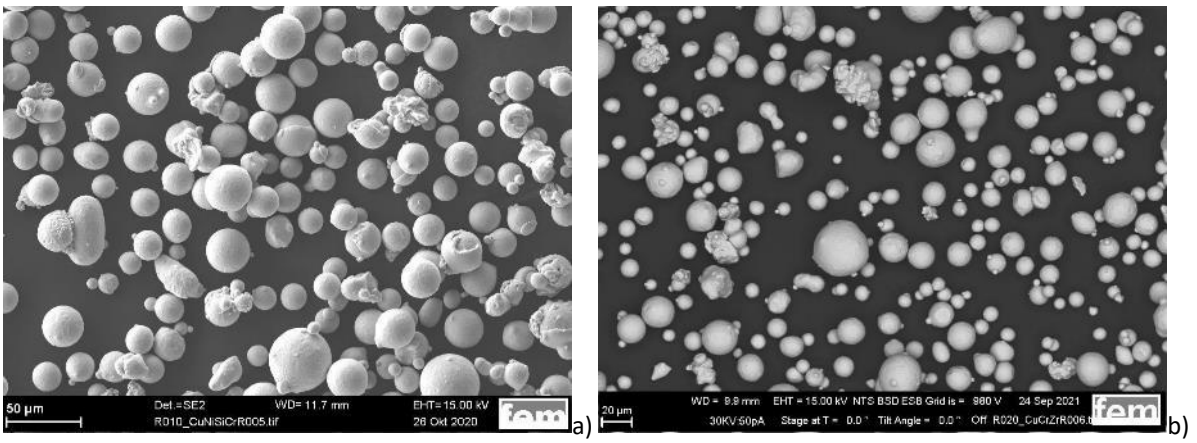

a) b)

Figure 61: SEM examination of the powder morphology (uncoated powders) - a) CuNiSiCr b) CuCrZr

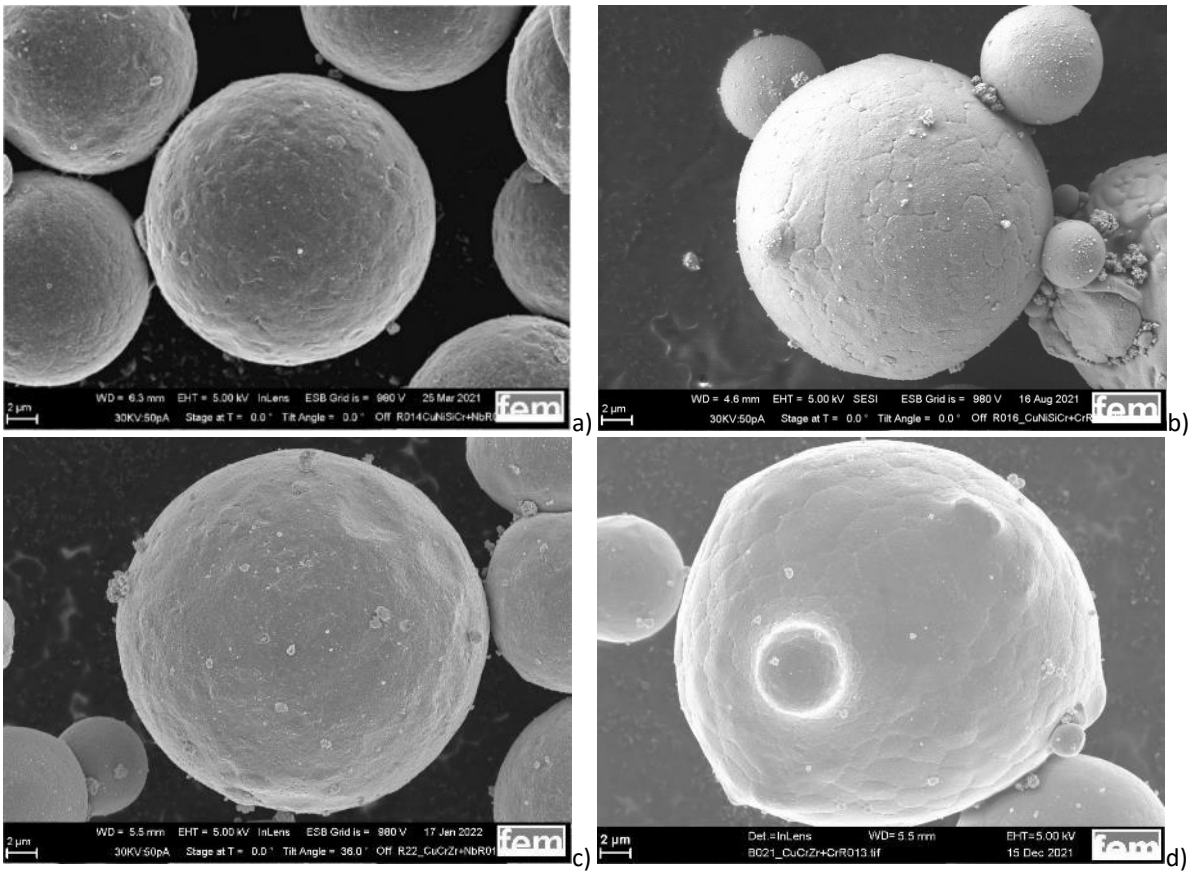

a) b) c) d)

Figure 62: SEM examination of the powder morphology (coated powders) - a) CuNiSiCr + Nb coating b) CuNiSiCr + Cr coating c) CuCrZr + Nb coating d) CuCrZr + Cr coating

The CuNiSiCr powder (CNCS – Schmelzmetall) presented an original grain size 20÷63 µm and was sieved <45 µm, while the CuCrZr powder (CCZ – Schmelzmetall) had an original grain size of 15÷45 µm. Both powders present spherical form, with occasional spattered particles present (see Figure 61). The SEM examination of the coated powders could prove that the round shape of the particles was not

influenced by the coating (see Figure 62). By FIB examination of the powder grains, uniform coating thicknesses of 40 to 160 nm (depending on the material – see Figure 63 and Figure 64) were measured, as listed in Table 6. The described coated powders were used for LBM experiments, and the results are presented in WP4.

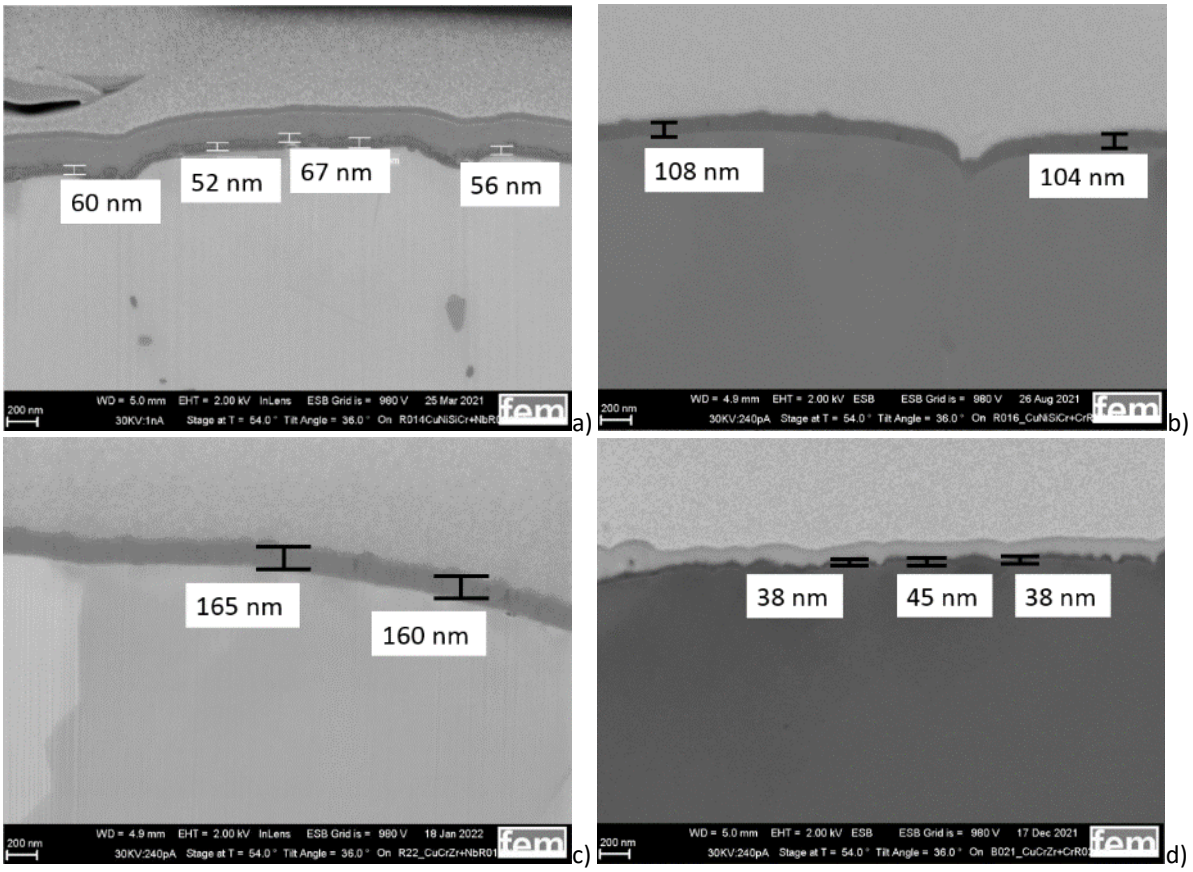

Figure 63: FIB cut of coated powder grains with measurement of the coating thickness - a) CuNiSiCr + Nb coating b) CuNiSiCr + Cr coating c) CuCrZr + Nb coating d) CuCrZr + Cr coating

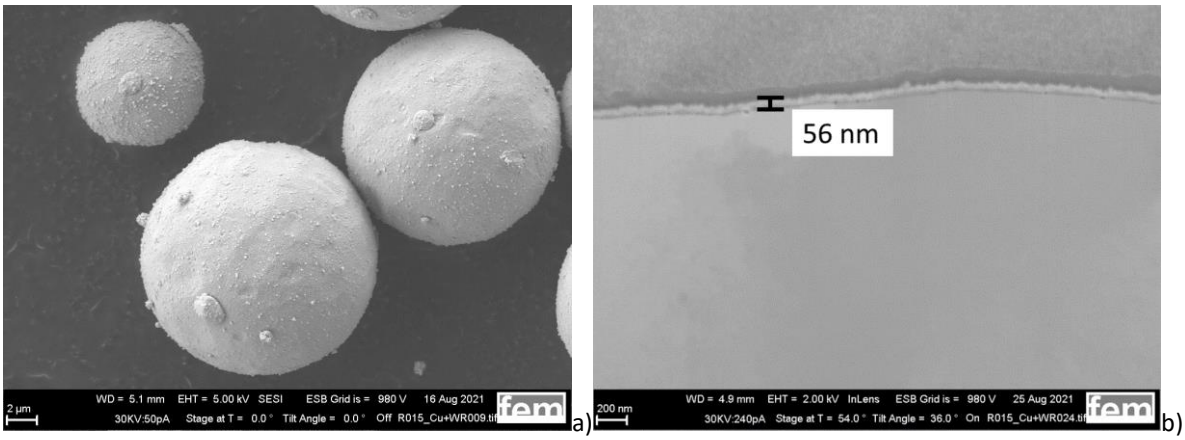

Figure 64: Pure Cu with W coating - a) SEM investigation of the powder morphology b) FIB cut of a powder grain with measurement of the layer thickness

3.1.4 WP3: Processing of Al-alloys by LBM

3.1.4.1 Performed activities – Sirris

The activities aimed at modifying 2 aluminium alloys:

- 7075 because it is prone to hot cracking during AM printing
- 7020 is a weldable alloy with low mechanical properties that could benefit from modification.

Singles track analysis for 7075 coated with Ti and Zr

Plates of 7075 were coated with 100 nm and 200 nm thick coatings. These plates were illuminated by the laser with several power levels and several scanning speeds. The aim was to identify and measure the meltpool depth and the presence or not of cracks. Samples were sectioned, polished and etched (see Figure 65 and Figure 66).The meltpool depth evolves non linearly with the power input. Beyond a certain power threshold, cracks are formed in the meltpool.

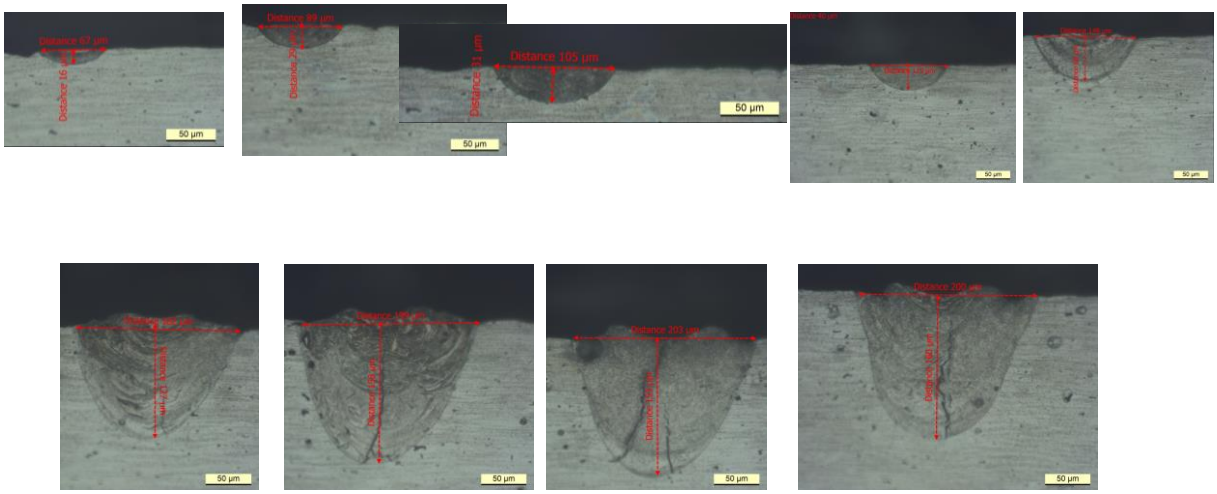

Figure 65: Results for 200 nm thick Ti coating on 7075

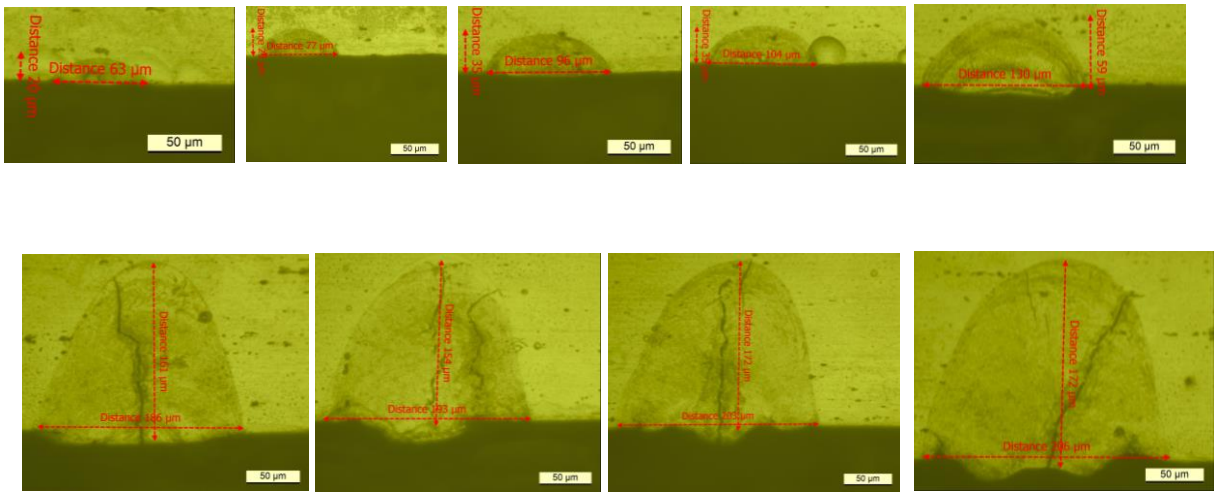

Figure 66: Results for 200 nm thick Zr coating on 7075

The graph in Figure 67 shows the meltpool depth as a function of the power input of the laser.

The optimal process parameter must meet the corresponding criteria:

- The meltpool depth must be at least the same as the layer thickness
- The absence of cracks

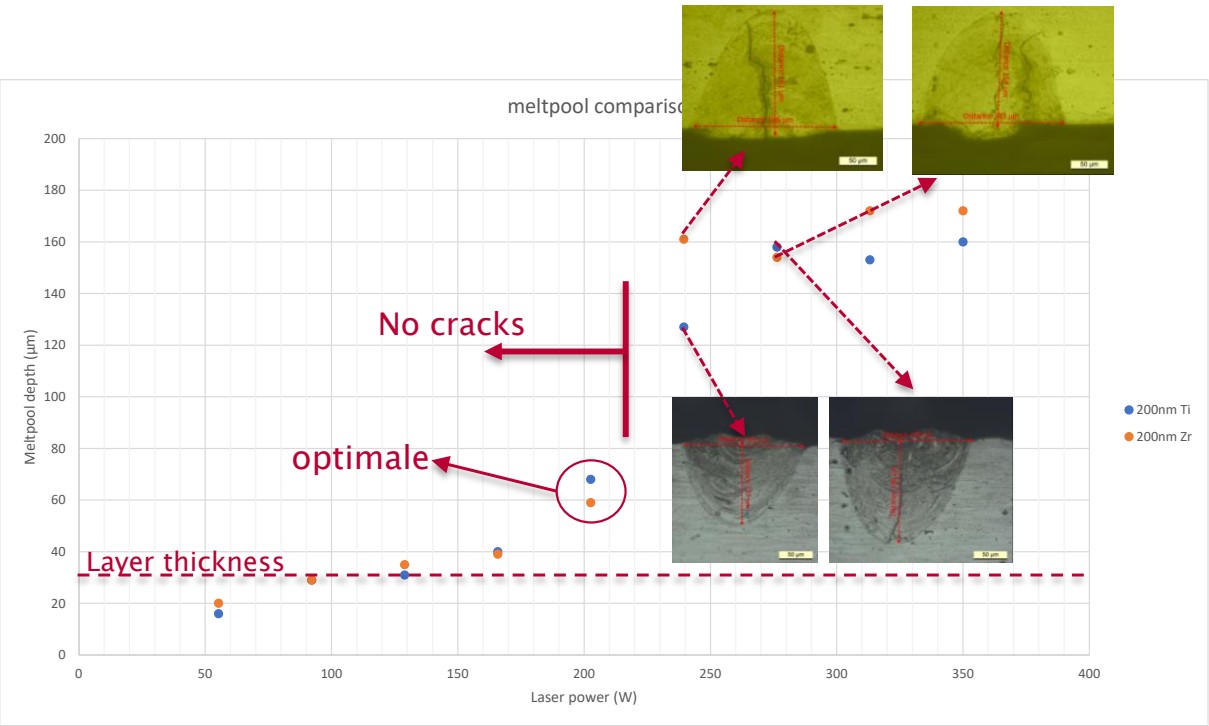

Figure 67: Meltpool depth as a function of the power input of the laser

The meltpool profile has typically two modes:

- Conductive mode
- Keyhole mode

The best results are obtained by keeping the conductive mode to control the overlap of tracks.

Calculation of the weight percentage ratio

The simple approach is to use the cross section surface of the coating with respect to the cross section surface of the meltpool depth (Figure 68).

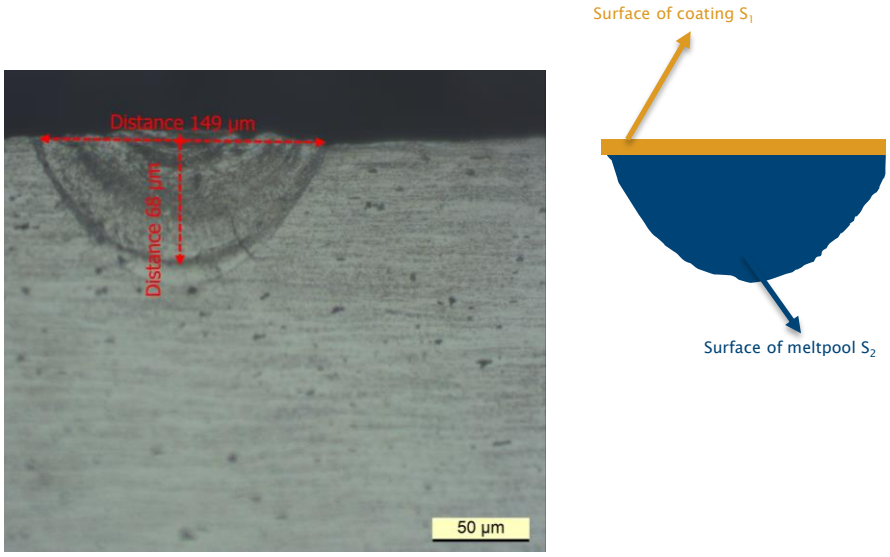

Figure 68: Values used for the calculation of the weight percentage ratio

$$\%\ element = \frac{\rho_{element} \cdot S_1}{\rho_{7075} \cdot S_2}$$

The hatch distance was computed based on the size of the meltpool to insure proper overlap (Figure 69).

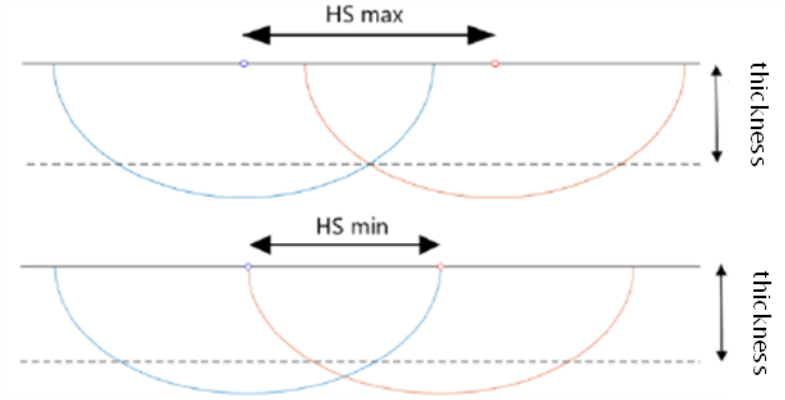

Figure 69: Variation of the hatch distance

Design of experiment

Table 7 shows the parameter used in the DOE, while Figure 70 shows the graphical evaluation of the DOE results.

Table 7: DOE Parameter variations

	P [W]	V [mm/s]	HS [µm]	Stratégie de remplissage	Epaisseur de couche [µm]	densité relative [%]
Plan treillis						
1	160	360	60	damier	30	98,58
2	160	360	60	damier	30	98,35
3	240	360	60	damier	30	97,13
4	240	360	60	damier	30	97,5
5	160	520	60	damier	30	98,7
6	160	520	60	damier	30	98,23
7	240	520	60	damier	30	97,1
8	240	520	60	damier	30	97,45
9	160	360	140	damier	30	98,28
10	160	360	140	damier	30	98,53
11	240	360	140	damier	30	93,34
12	240	360	140	damier	30	94,37
13	160	520	140	damier	30	98,3
14	160	520	140	damier	30	98,26
15	240	520	140	damier	30	97,9
16	240	520	140	damier	30	96,83
17	200	440	60	damier	30	98,32
18	160	440	100	damier	30	98,58
19	200	360	100	damier	30	98,52
20	200	440	100	damier	30	98,44
21	200	440	100	damier	30	97,84
22	200	440	100	damier	30	98,16
23	200	520	100	damier	30	98,36
24	240	440	100	damier	30	98,37
25	200	440	140	damier	30	98,32

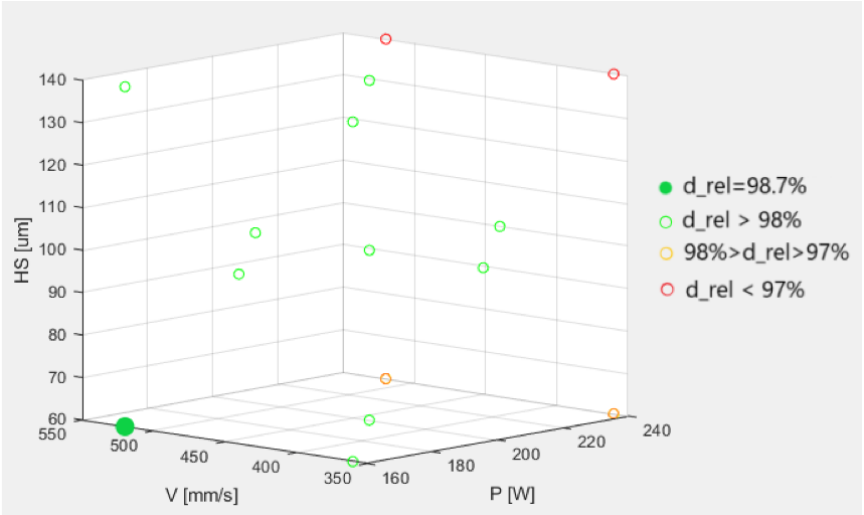

Figure 70: Graphical evaluation of the DOE results

Trials with build plate pre heating at 200°C

Based on the DOE and the best measurements obtained by Archimedes' measurement, samples were cross-sectioned and polished for image analysis (Figure 71). Etching can exacerbate present defects (Figure 72).

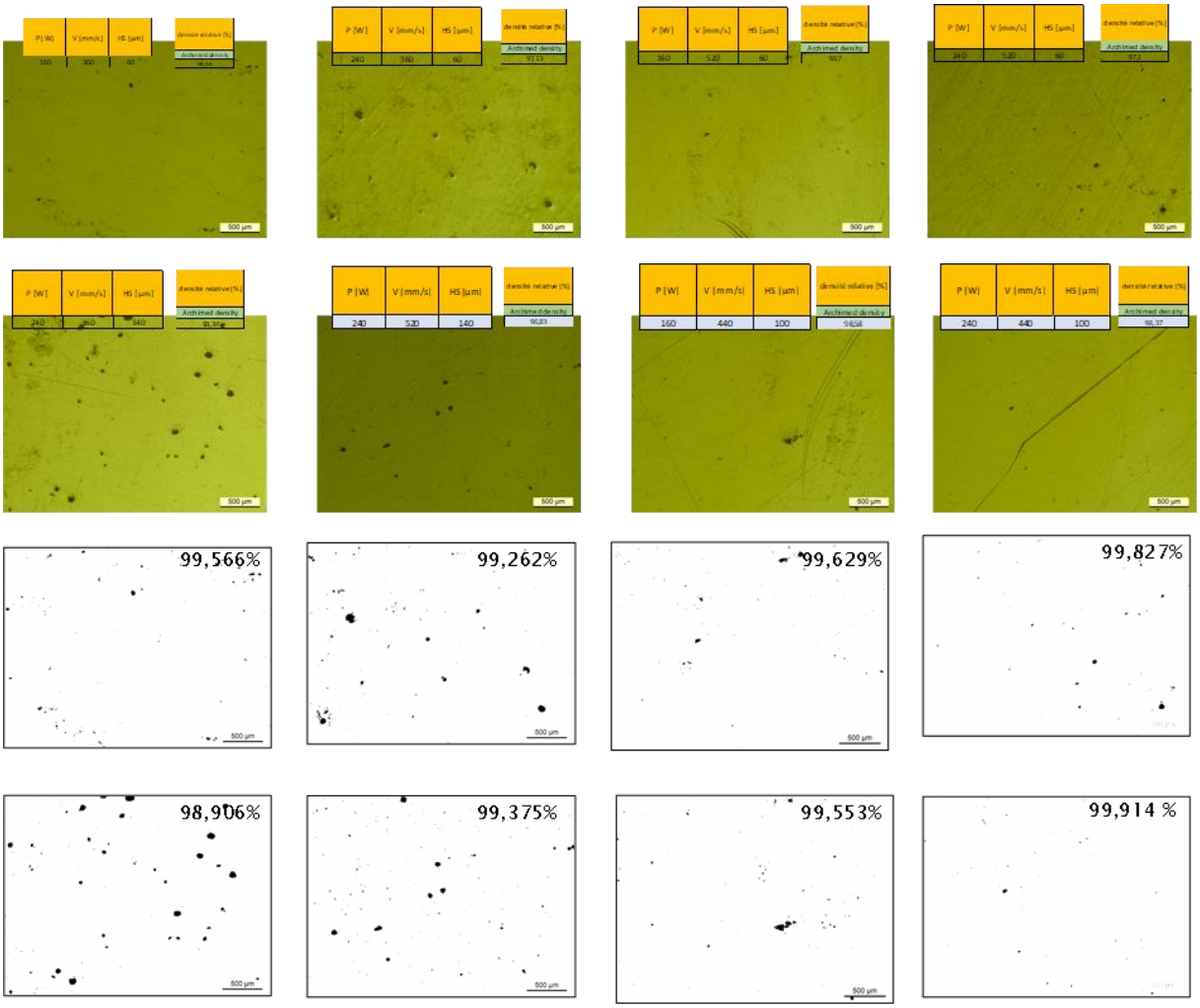

Figure 71: Cross sections of selected samples and corresponding image analysis

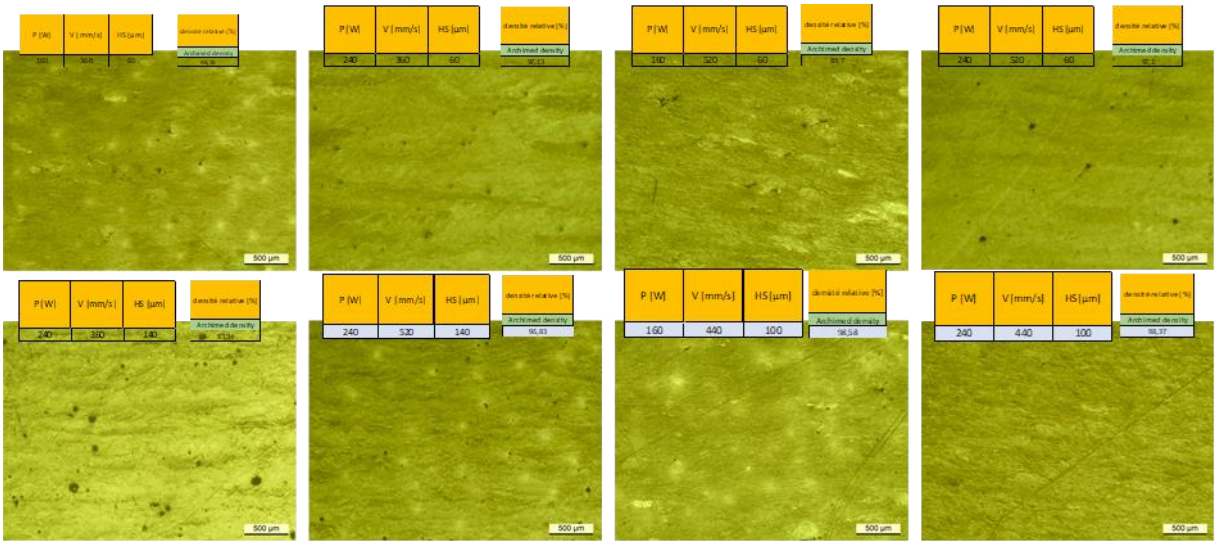

Figure 72: Etched samples

The best results were obtained for the following set of parameters: 240 W, 440 mm/s, hatch distance 100 µm (see Figure 73). The results are remarkable because of the absence of cracks in all processing conditions. The results show also the extensive grain refinement introduced by the selected element in the sample.

These parameters were also tested with much lower build plate temperature. It is known that higher temperature processing conditions improve the microstructure.

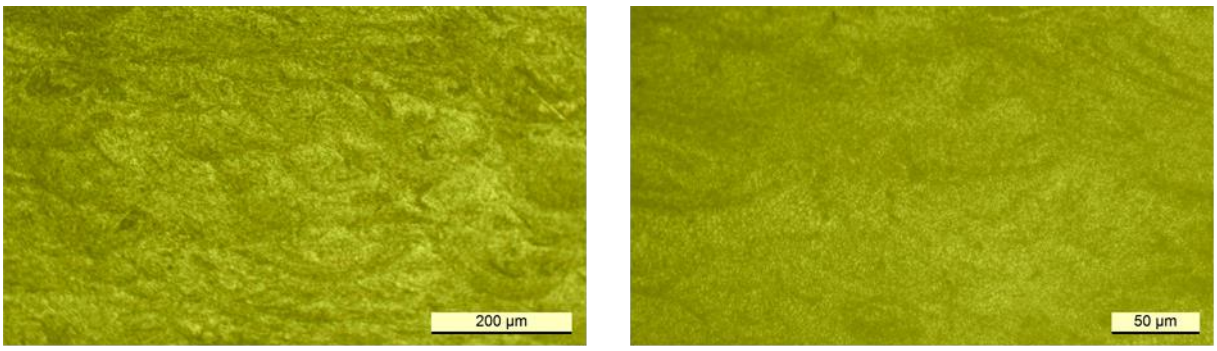

Figure 73: Results for 240 W, 440 mm/s, hatch distance 100 µm – Archimedes' density 98,37 %

Trials with build plate pre heating at 40°C

Figure 74 shows the results of the trials with build plate pre heating at 40°C. The absence of hot cracking is noticeable. Some lack of fusion defects have appeared but the grain refinement remains remarkable.

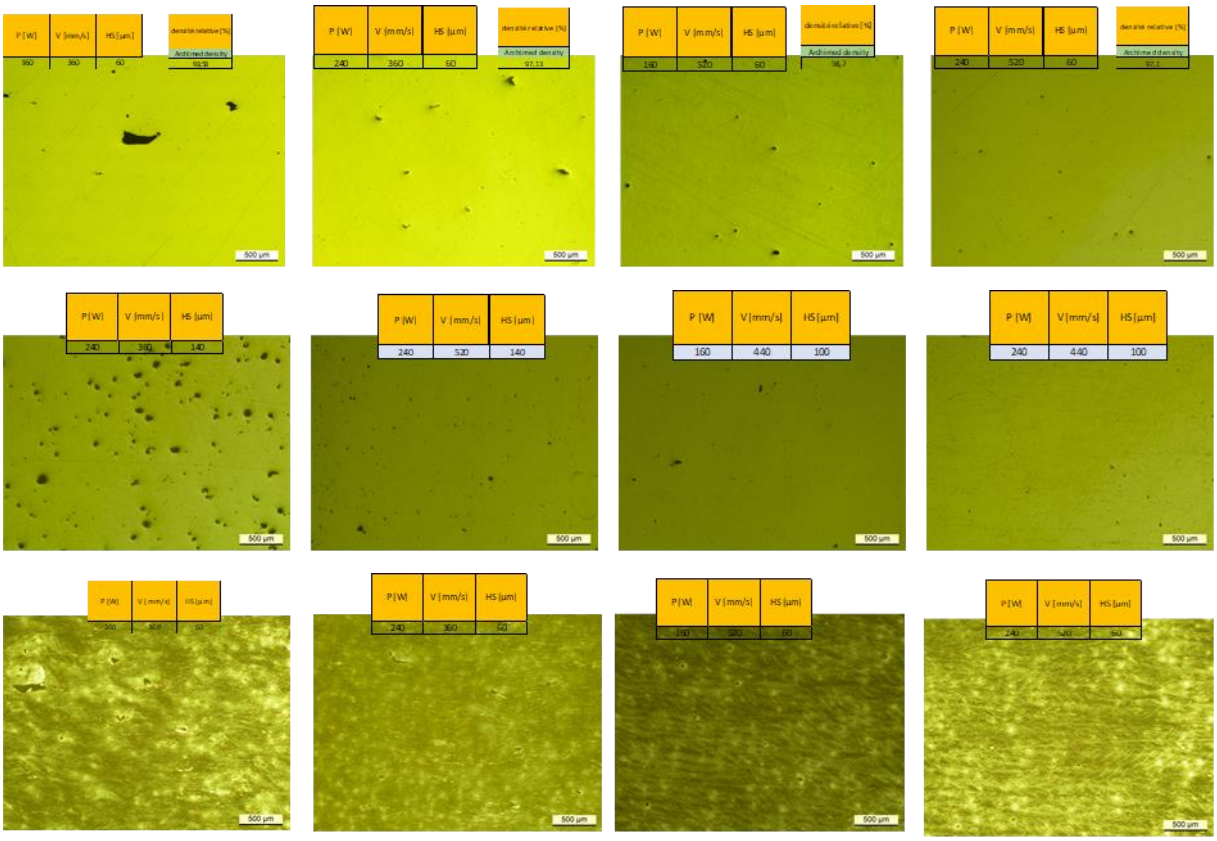

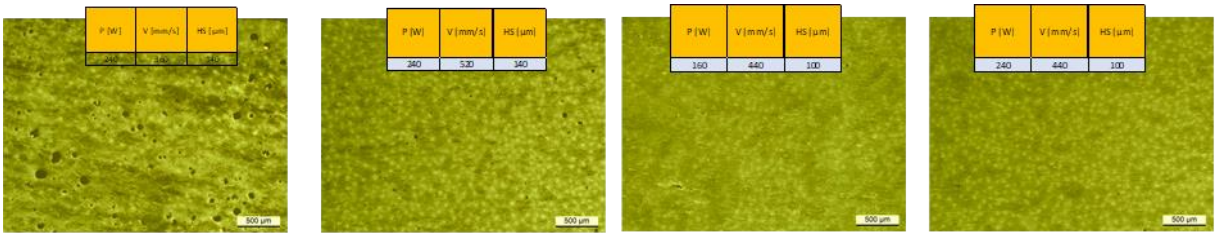

Figure 74: Trials with build plate pre heating at 40°C - cross sections of selected samples

Mechanical tensile testing

5 bars were printed horizontally and tested:

- In the as-build state
- Without a solution treatment but with an ageing conform to AMS2770 for 7075

Results are shown in Table 8and Table 9. Failure took place out of the extensometer for the T6 state. Interpreting the maximum elongation at failure of the tensile strength is tedious.

Table 8: Results in the as-build state

Em	Rp	R	At
Module	Contrainte à 0.2%	Contrainte à la rupture	Déformation à la rupture
GPa	Mpa	Mpa	%
68	324,1	383,3	10,99

Table 9: Results in the T6 state

Em	Rp	R	At
Module	Yield strength	Tensile strength	elongation at failure
MPa	Mpa	Mpa	%
71332	317,9	364,5	8,08

Demonstrator

A part was built with the modified powder for a partner in the project (Figure 75).

Figure 75: Demonstrator built in the project. Geometry and function of the part are property and know-how of one of the SME participating to the project.

7020 aluminium alloy

This alloy is a well-known weldable alloy. The target was to modify the composition (with Mg and B) to increase mechanical properties. The Mg addition will create precipitates that will act as strengthening elements after heat treatment. The boron aims at reacting with the titanium inside the matrix and form TiB_2 strengthening elements.

The results for the single track analysis with 100 nm Mg-coating on metal sheets are shown in Figure 76. The corresponding results for the 100 nm B-coating are shown in Figure 77. Figure 78 shows the evaluation of melt pool depth and width for different laser speeds.

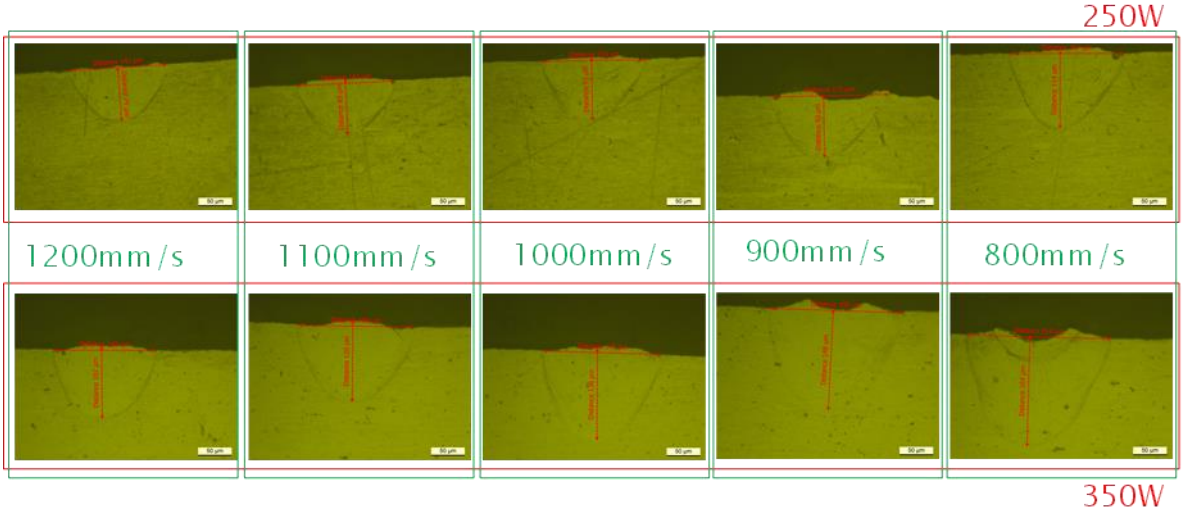

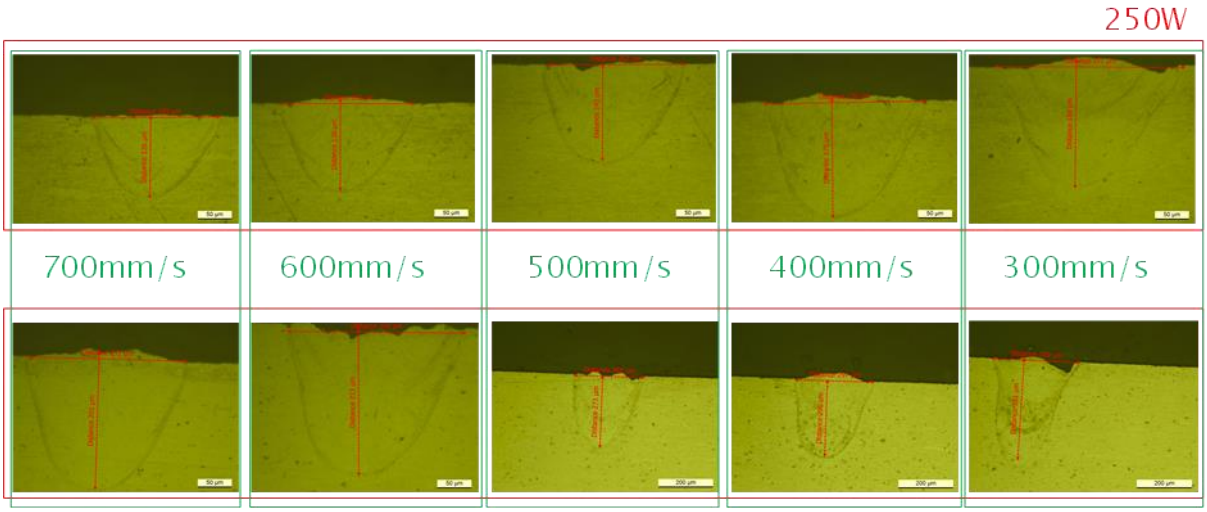

Figure 76: Results for the single track analysis of cross sections with 100 nm Mg-coating

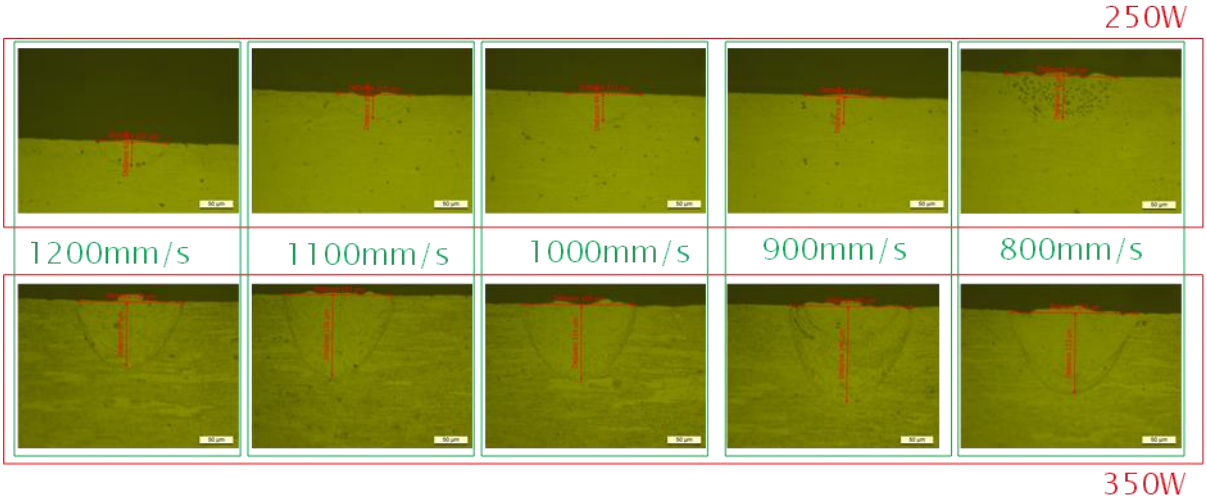

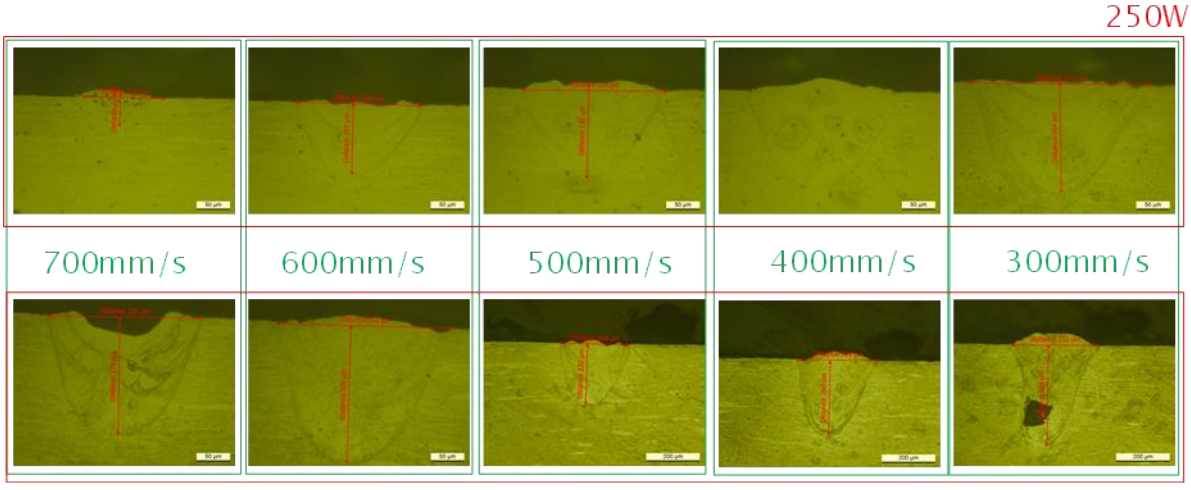

Figure 77: Results for the single track analysis of cross sections with 100 nm B-coating

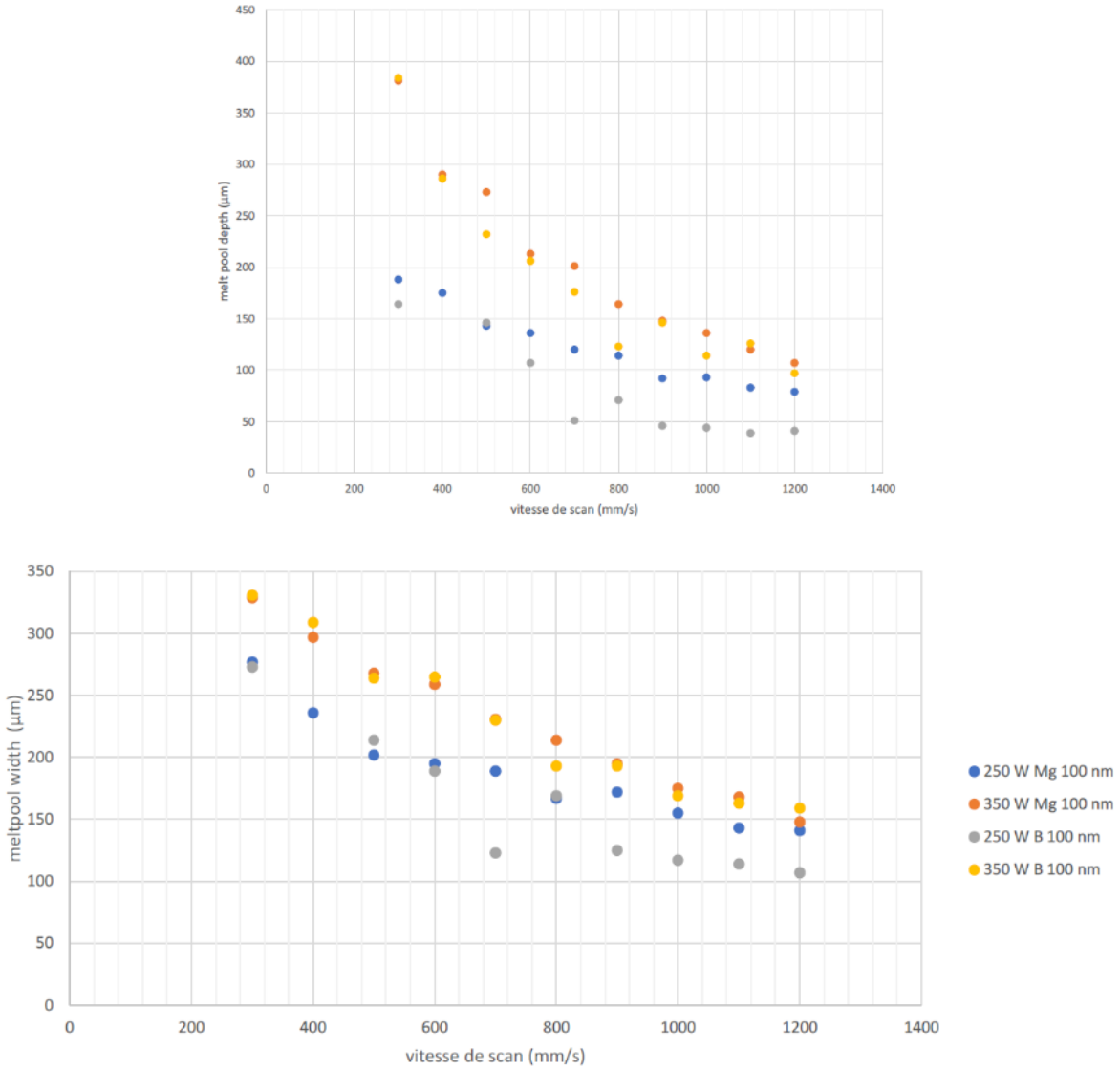

Figure 78: Melt pool depth and width for different laser speeds

Conclusions

- Alloy is weldable (because it contains Ti and Zr) - No cracks are visible
- Coating has no influence on absorption at high energy
- A small influence of coating absorption at 250 W and high speed (conduction mode of the melt pool)
- The powder was not tested, since it was not commercially available

3.1.5 WP4 Processing of Cu and Cu alloys by LBM / EBM

3.1.5.1 Performed activities – fem

- A DOE parameter study with the CuNiSiCr alloy powder was conducted to find a parameter window for a laser power up to 480 W, and therefore optimize its processability
- Laser parameters for the CuCrZr powder were also determined based on the results obtained with the CuNiSiCr alloy
- The Nb- and Cr- coated CuNiSiCr and CuCrZr powders and the W-coated pure copper powder were processed with LBM. Laser parameters were adjusted for the higher energy absorption of these materials

- Investigations (SEM, metallography) were performed on the built specimens
- Manufacturing of demonstrators out of CuNiSiCr and CuCrZr
- Determination of the mechanical and physical properties of the components before and after heat treatment
    - Preparation and testing of small plates and tensile specimens
    - Three material conditions (as-built, solution annealed, and solution annealed + aged)
    - Hardness measurement
    - Measurement of electrical conductivity
    - Mechanical testing of specimens
    - Investigation of tensile samples after testing

LBM processing of the coated and uncoated powders

A DOE parameter study was carried out on the untreated CuNiSiCr powder to establish a parameter window for a laser power up to 480 W in order to achieve optimum density: the powder layer thickness was kept constant (0.025 mm), while the laser power (95-480 W), speed (100-1400 mm/s) and track spacing (0.025-0.085 mm) were varied (see Table 10 for a complete list). The chosen part used for said variation was a test geometry designed at fem, which features thick and thin areas, as well as curved and inclined surfaces (see Figure 79). The parts were first examined in the SEM to assess the final processed layer and the corresponding melt pool obtained. Subsequently, the porosity in the cross section was investigated by quantitative image analysis (best results were validated by measuring more than one cross section plane).

Examples of SEM investigations can be seen from Figure 80 to Figure 82: depending on the parameter set, strong differences in the uniformity of the melt pool can be observed. Laser power and speed can strongly affect the fidelity to the original geometry: Figure 80 shows the effect of applying two extremes of the laser power, and Figure 81 of using two different speeds (in both cases keeping the other parameters constant). The variation of the hatch distance has also a strong impact on the porosity of the part, since it controls the overlap (or lack thereof) of the molten laser tracks. Figure 82 shows a detailed view of the part surface in case of the two extreme hatch distance values: a high value causes a clearly visible insufficient overlap (Figure 82 left), while for a too small one the scan track overlap is excessive (Figure 82 right, leading to excessive energy input and 7% porosity in the part, as shown in Figure 83a).

Figure 83 shows the metallographic cross sections for selected parameter sets (in hatch distance order). Smaller track gaps (0.025-0.035 mm) lead to high porosity values (7-12% see Figure 83a-c) at any power and even to the termination of the building process, because the building of the geometry is no longer guaranteed. A laser power of 200 W is not sufficient to melt the material (porosity 2.5-7% - see Figure 83a and h). To this purpose is required a minimum power of 300 W, in combination with a track spacing equal to or greater than 0.045 mm (porosity 0,5 to < 0.1% - see Figure 83d, e and g). Laser power values higher than 380 W, although achieving a low porosity in the massive lower region of the part, lead to strong distortion of the intended shape (Figure 83f). The following parameter window was defined based on the results. Laser power: 300-380 W, laser speed: 600-850 mm/s, hatch distance: 0.055-0.075 mm.

Based on these values, optimal parameters for the LBM processing of the uncoated CuCrZr alloy were established. The metallographic cross sections in Figure 84 show the porosity in the part depending on the variation of laser power and speed (by keeping constant the 0.055 mm hatch distance, which in the previous optimization was found to be the most stable). The optimal parameter set for CuCrZr was

established to be laser power 380 W, laser speed: 850 mm/s, and hatch distance: 0.055 mm (obtaining a porosity of 0,04 % - Figure 84d).

Table 10: Parameter list (arranged in hatch distance order) used in the DOE variation on the CuNiSiCr alloy with the corresponding measured porosity in the built part (*mean value of two cross section planes)

Power [W]	Speed [mm/s]	Hatch distance [mm]	Porosity [%]
293	750	0,025	n/a – building failed / geometry deformed
480	800	0,025	n/a – building failed / geometry deformed
480	1200	0,025	n/a – building failed / geometry deformed
200	600	0,035	7,08
300	800	0,035	10,71
350	850	0,035	12,15
400	800	0,035	n/a – building failed / geometry deformed
450	800	0,035	n/a – building failed / geometry deformed
450	1200	0,035	n/a – building failed / geometry deformed
300	750	0,045	n/a – building failed / geometry deformed
350	800	0,045	0,31*
480	1400	0,045	n/a – building failed / geometry deformed
300	800	0,055	0,05*
380	850	0,055	0,05*
450	850	0,055	n/a – building failed / geometry deformed
300	800	0,060	0,05
340	1000	0,060	n/a – building failed / geometry deformed
380	850	0,060	n/a – building failed / geometry deformed
480	1200	0,060	n/a – building failed / geometry deformed
350	800	0,075	0,07
450	850	0,075	n/a – building failed / geometry deformed
200	1400	0,085	2,53
300	800	0,085	n/a – building failed / geometry deformed
380	850	0,085	0,09
480	600	0,085	n/a – building failed / geometry deformed
480	1400	0,085	n/a – building failed / geometry deformed

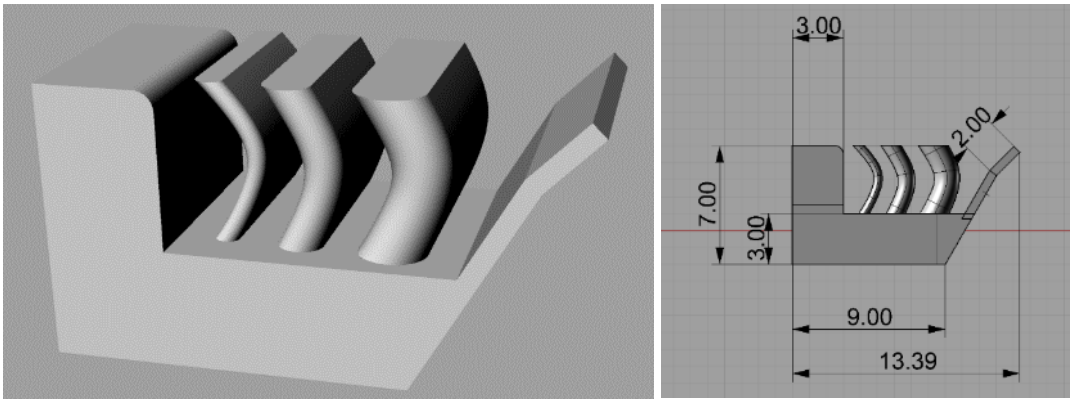

Figure 79: Geometry of the test part used for the LBM trials and its dimensions

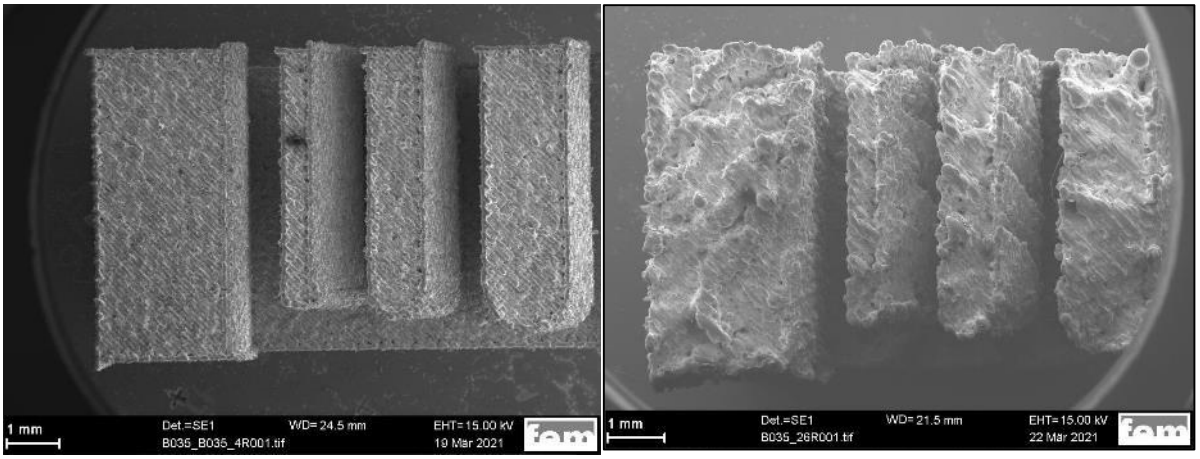

Figure 80: Influence of the laser power at the same hatch distance (0.085 mm) and laser speed (1400 mm/s) Left: Power = 200 W - Right: 480 W

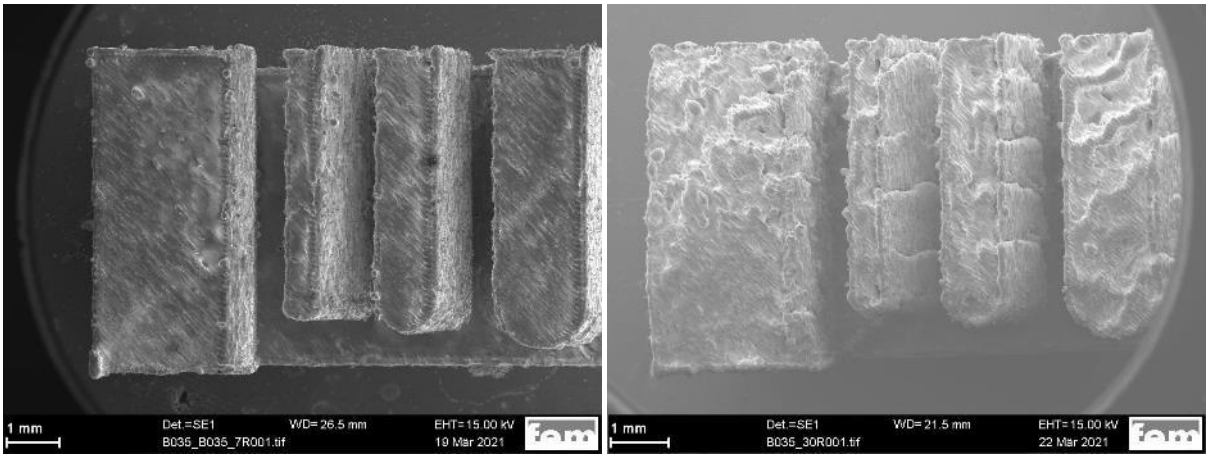

Figure 81: Influence of the laser speed at the same hatch distance (0.035 mm) and laser power (300 W) Left: Laser speed = 800 mm/s - Right: 1400 mm/s

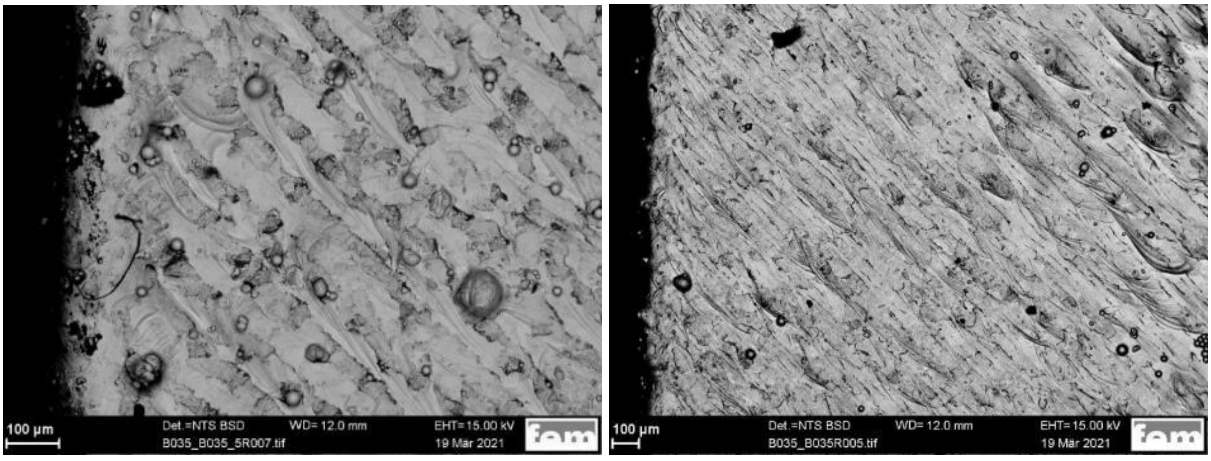

Figure 82: Influence of the hatch distance at the same power (200 W) and laser speed (600 mm/s) Left: Hatch distance = 0.085 mm (insufficient scan track overlap) - Right : Hatch distance = 0.035 mm (excessive scan track overlap)

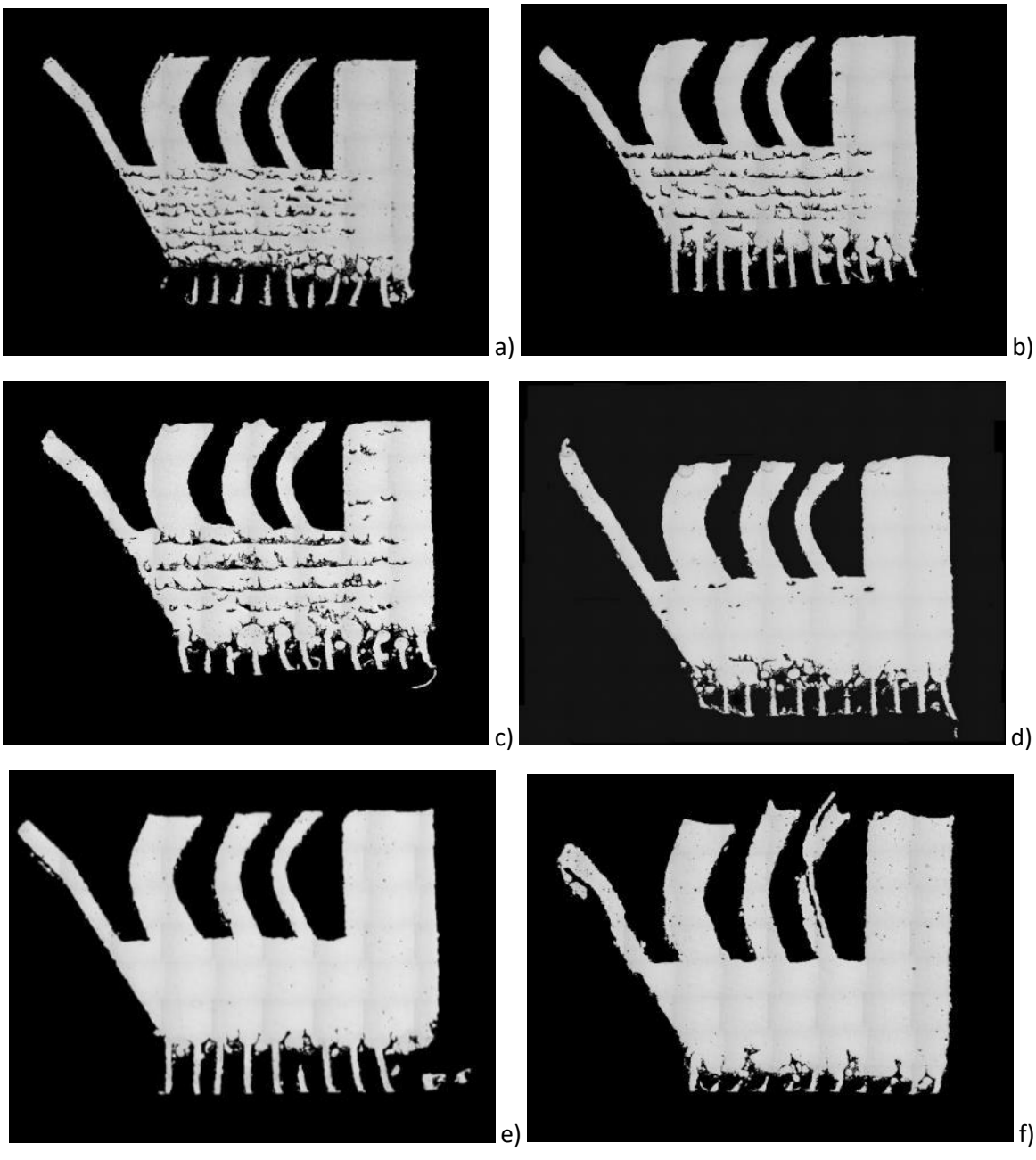

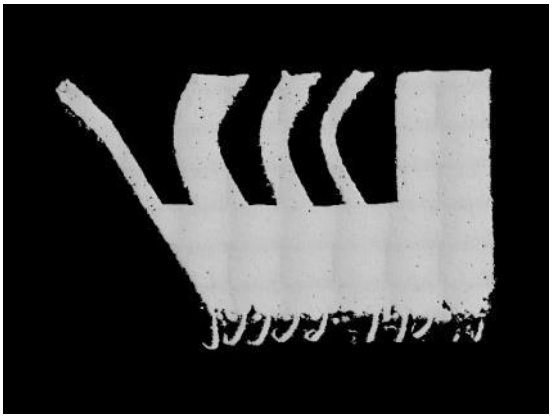
g)
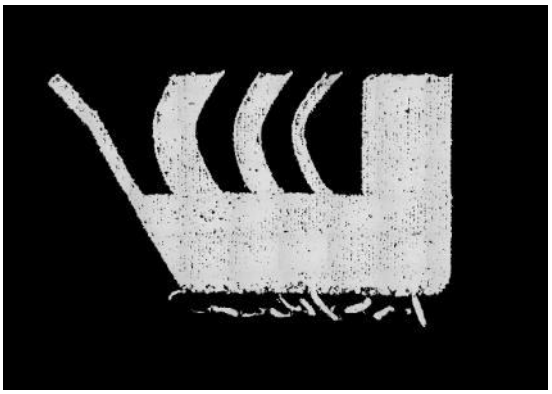
h)

Figure 83: Metallographic examination of the test parts made of CuNiSiCr – a) 200 W - 600 mm/s - hatch distance = 0.035 mm - porosity 7.1 % / b) 300 W - 800 mm/s - hatch distance = 0.035 mm - porosity 10.71 % / c) 350 W - 850 mm/s - hatch distance = 0.035 mm - porosity 12.15 % / d) 350 W - 800 mm/s - hatch distance = 0.045 mm - porosity 0.54 % e) 300 W - 800 mm/s - hatch distance = 0.055 mm- porosity 0.05 % / f) 450 W - 850 mm/s - hatch distance = 0.055 mm- geometry deformed / g) 350 W - 800 mm/s - hatch distance = 0.075 mm- porosity 0.07 %/ h) 200 W - 1400 mm/s - hatch distance = 0.085 mm- porosity 2.53 %

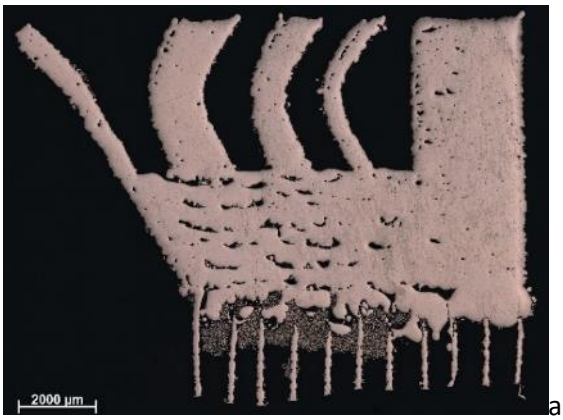

a)


b)


c)
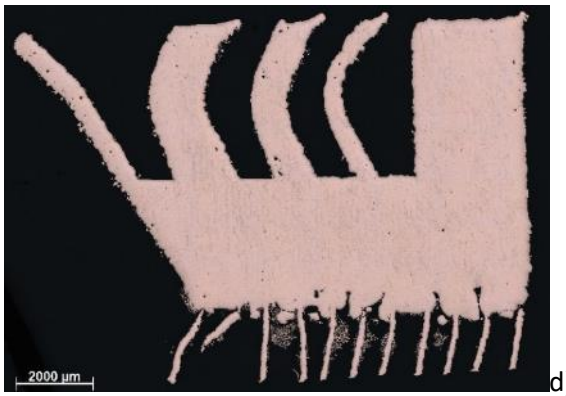

d)

Figure 84: Metallographic examination of the test parts made of CuCrZr – a) 380 W - 400 mm/s - hatch distance = 0.055 mm - porosity 4,7 % / b) 300 W - 400 mm/s - hatch distance = 0.055 mm - porosity 1,1 % c) 380 W - 600 mm/s - hatch distance = 0.055 mm - porosity 0,2 % /d) 380 W - 850 mm/s - hatch distance = 0.055 mm - porosity 0,04 %

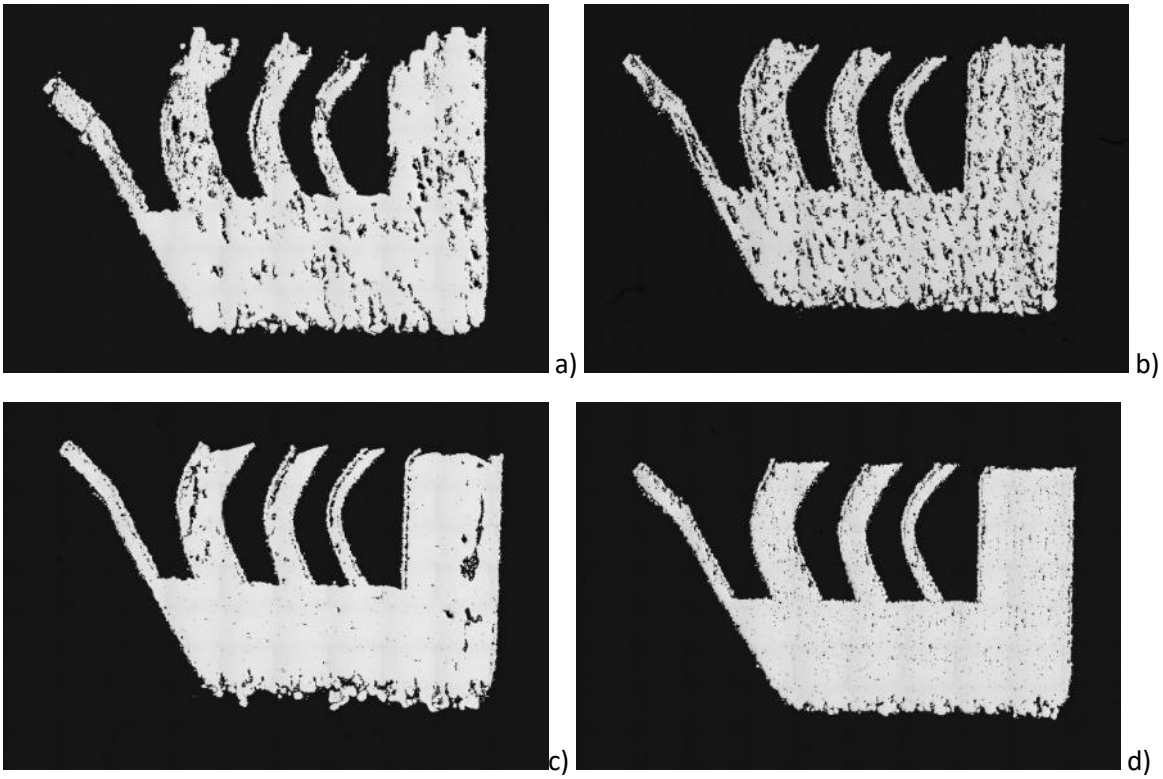

Figure 85: Metallographic examination of the test parts made of CuNiSiCr + Nb coating – a) 250 W - 1000 mm/s - hatch distance = 0.035 mm - porosity 6.5 % and deformed geometry b) 200 W - 1400 mm/s - hatch distance = 0.035 mm - porosity 9,2 % / c) 150 W - 600 mm/s - hatch distance = 0.045 mm - porosity 1,3 % / d) 200 W - 600 mm/s - hatch distance = 0.085 mm - porosity 1,0 %

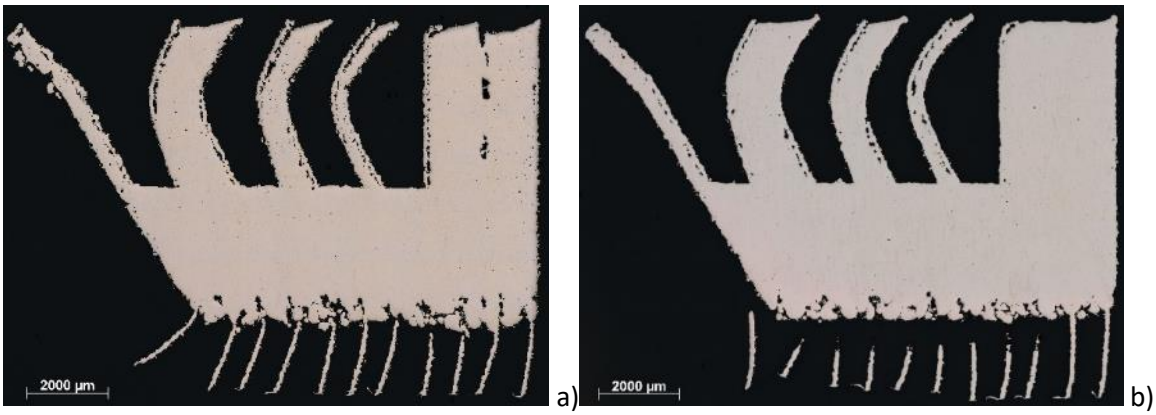

Figure 86: Metallographic examination of the test part made of coated CuNiSiCr – a): CuNiSiCr + Nb, process parameter 200 W - 600 mm/s – hatch distance = 0.055 mm - porosity 0.05 % / b): CuNiSiCr + Cr, process parameter 200 W - 900 mm/s - hatch distance = 0.055 mm- porosity 0.04 %.

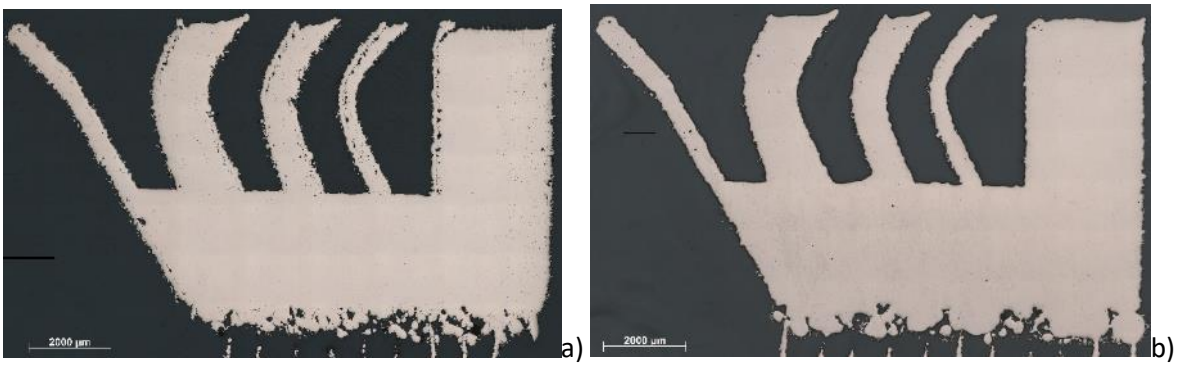

a) b)

Figure 87: Metallographic examination of the test part made of coated CuCrZr – a): CuCrZr + Nb, process parameter 250 W - 600 mm/s – hatch distance = 0.055 mm - porosity 0.02 % / b): CuCrZr + Cr, process parameter 350 W - 850 mm/s - hatch distance = 0.055 mm- porosity 0.1 %.

The selected parameters proved not to be optimal for processing the powder coated with Nb, which has a higher energy absorption than the uncoated alloy. Laser power values greater than 200 W led to building failure (Figure 85a), and the parameters needed to be adjusted accordingly. Keyhole porosity formation could be observed even at low power (200 W) in almost every sample, especially for hatch distances equal to or smaller than 0,045 mm (Figure 85b and c). Higher hatch distances on the other hand lead to porosity due to insufficient overlap and hence melting (Figure 85d).

In this case, the best results were obtained with a laser power of 200 W, a speed of 600 mm/s and a track pitch of 0.035-0.055 mm (0.05-0.1% porosity - see Figure 86a). Higher speeds lead to worse results (7-9% porosity as discussed and shown in Figure 85). The parameters for processing the CuNiSiCr with Cr coating were selected based on the already established parameter window, and low porosity values (0.04-0.1% - see Figure 86b) were obtained also in this case. The same low porosity values were obtained with the CuCrZr alloy with Nb / Cr coating (see Figure 87).

The SEM examination of the surface of the parts made of CuNiSiCr / CuCrZr + Nb / Cr showed finely distributed impurities. EDX measurements on these areas detected increased contents of Nb / Cr (respectively) and oxygen (Figure 88). The SEM investigation of the cross sections revealed finely distribute dark dots visible in the microstructure of both alloys (Figure 89): in this respect, EDX measurements were able to detect increased contents of Nb, Cr, Ni, Si and oxygen at the corresponding points (Figure 90 and Figure 91), which indicates oxide and precipitates formation.

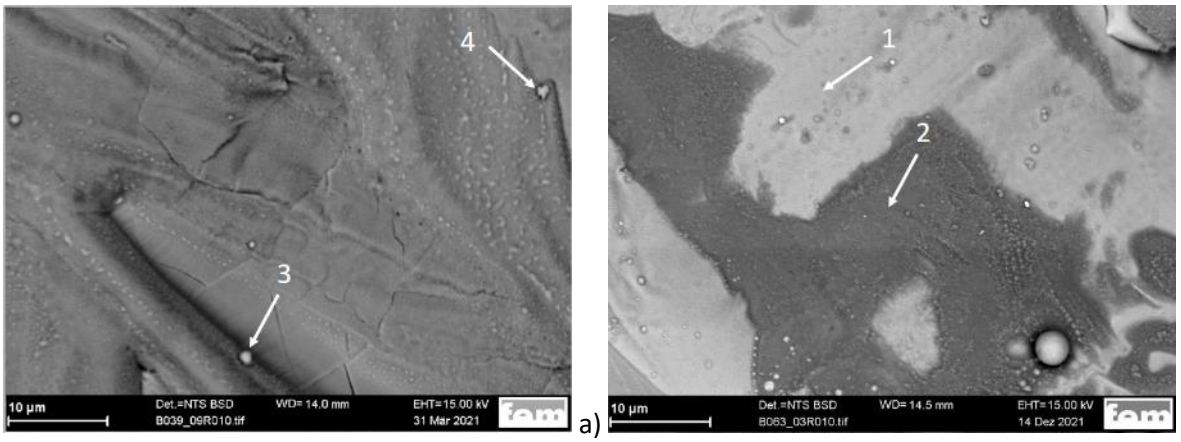

a) b)

Figure 88: SEM examination of the part surface with EDX measurements - left: CuNiSiCr + Nb coating – EDX Measurement points. 3 and 4: Nb and O / right: CuCrZr + Cr coating – EDX Measurement points. 1: Cu, Cr, and O - 2: Cu, Cr, Zr and O

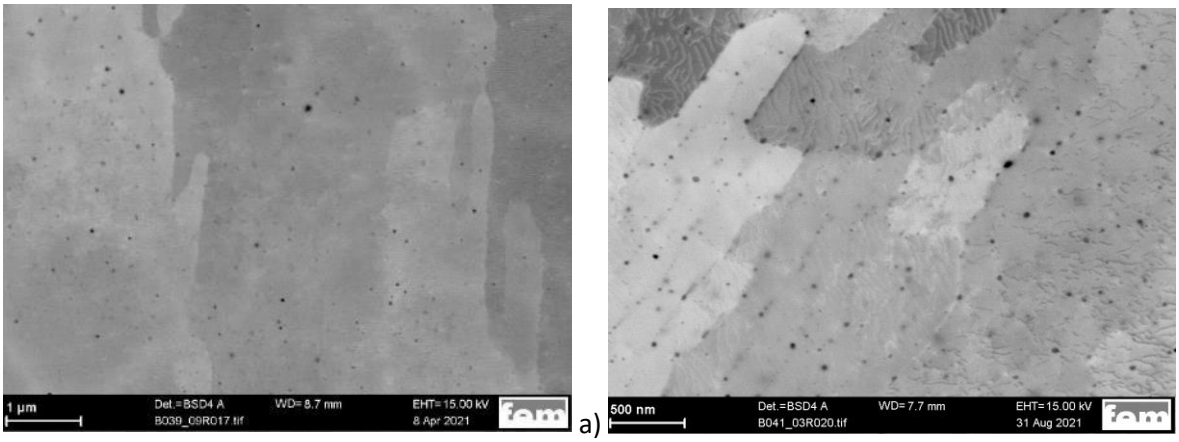

Figure 89: SEM examination of the microstructure of the part made of coated CuNiSiCr. Oxide dispersion visible in the matrix a) alloy with Nb coating b) alloy with Cr coating

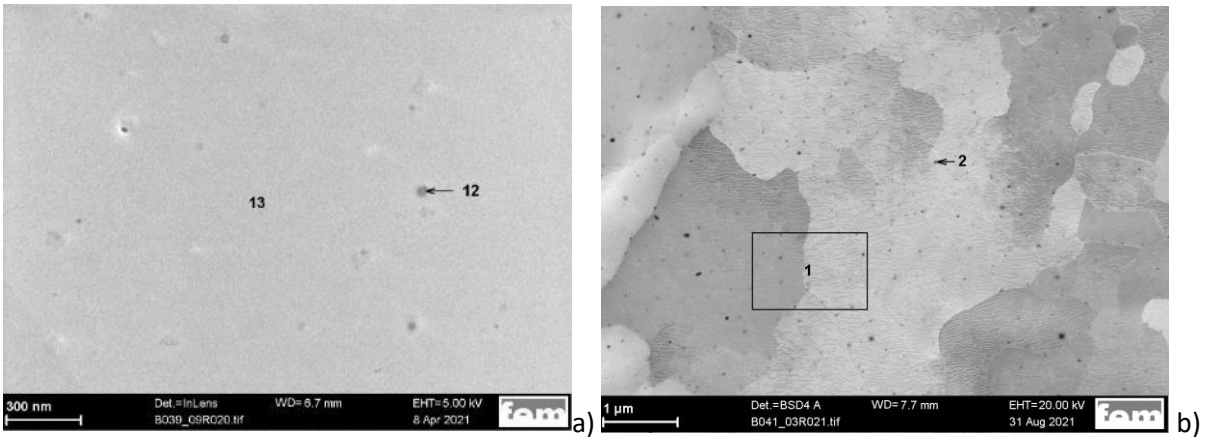

Figure 90: SEM examination of the microstructure of the part made of coated CuNiSiCr with EDX measurements. Oxide dispersion visible in the matrix a) alloy with Nb coating - EDX Measurement points. 13: Cu matrix, Nb / 12: Nb, Si and O / b) alloy with Cr coating - EDX Measurement points. 1: CuNiSiCr matrix / 2: Si and O

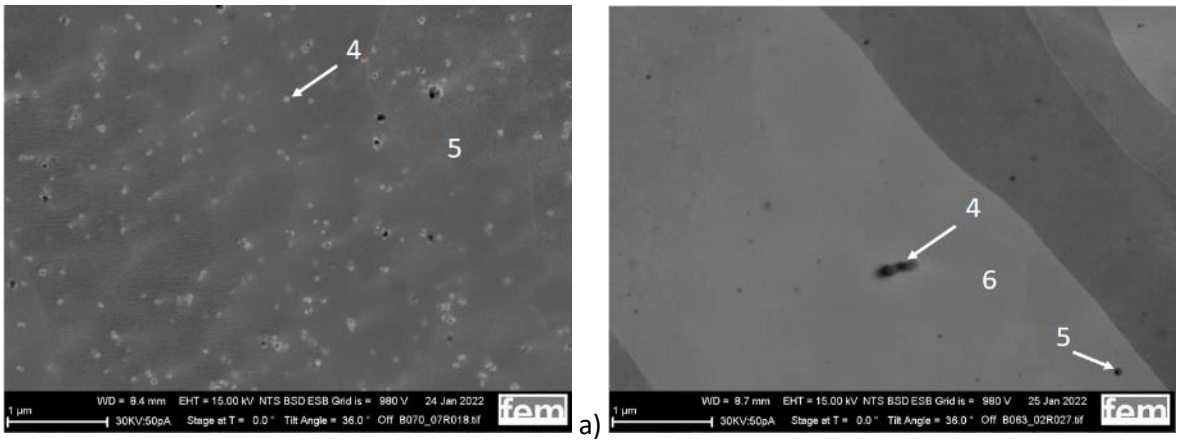

Figure 91: SEM examination of the microstructure of the part made of coated CuCrZr with EDX measurements. Precipitates visible in the matrix a) alloy with Nb coating - EDX Measurement points. 5: Cu, Cr / 4: Cu, Cr, Nb / b) alloy with Cr coating - EDX Measurement points. 4,5: Cu, Cr, Zr and O / 6: Cu, Cr

TEM lamellae from the mentioned cross sections were prepared (one for each different alloy) and investigated by STEM. Fine distributed precipitates in the matrix are clearly visible in each case (see Figure 92). Depending on their size the promote precipitation hardening by hindering the dislocation movement. Figure 92b shows the particle-dislocation interaction in the Cr coated CuNiSiCr powder.

The optimization of the coating thickness, the processing conditions and post-LBM heat treatment is important for an improvement of the mechanical properties. The precipitation was intended in the research approach, which was to increase the amount of a non-mixable element in the alloy through PVD coating, and obtain finely distributed precipitates after LBM processing (as seen in Figure 91a and Figure 92) to increase the physical and mechanical properties of the parts. Further work will be required to understand the physical process and the interaction of coating, LBM process and post treatment in order to obtain optimum properties.
The oxide formation on the other hand is due to the high oxygen content of the powders and was not intentional: the obtained effect is however similar to oxide dispersion strengthened (ODS) alloys, and could be interesting for high temperature applications (because of the high creep resistance).

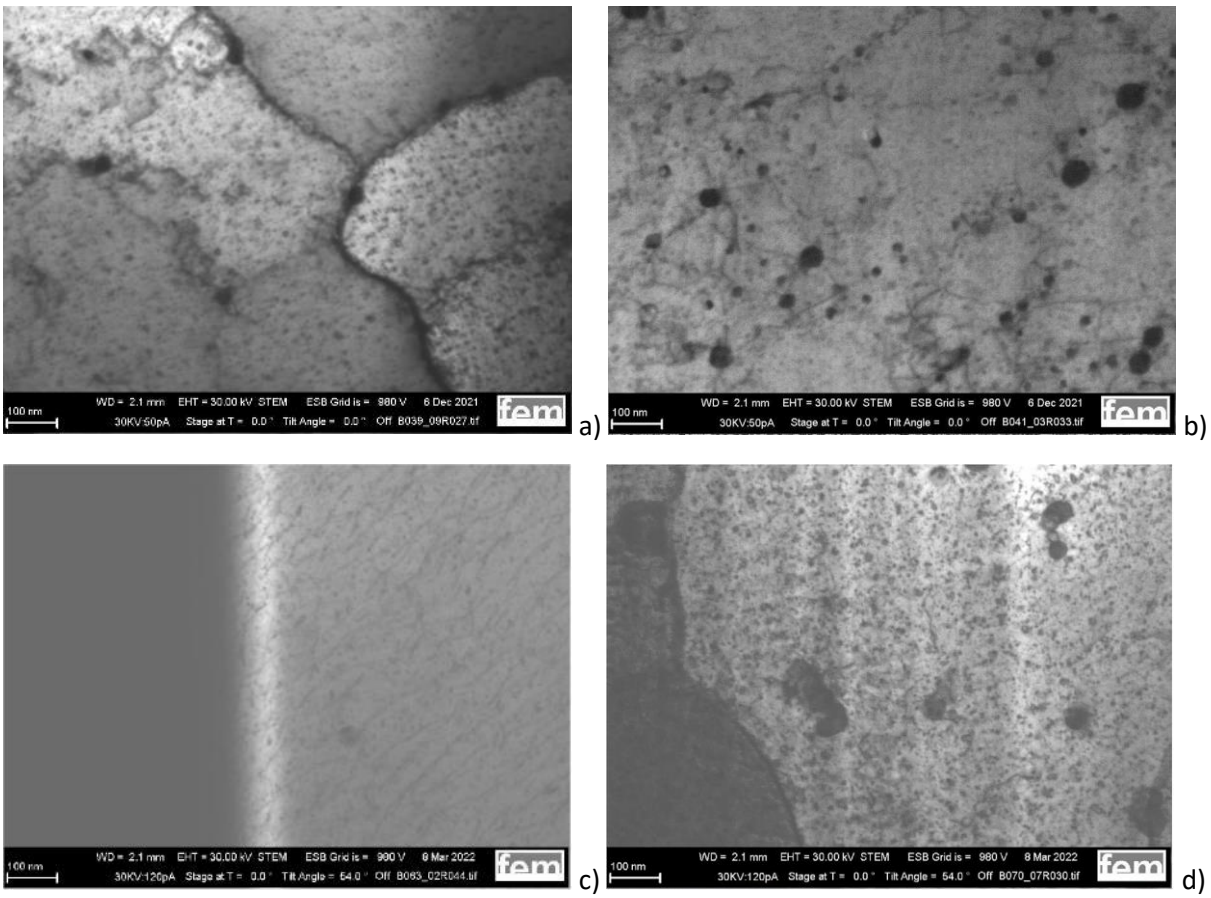

Figure 92: STEM investigation of TEM lamellae - a) CuNiSiCr + Nb / b) CuNiSiCr + Cr / c) CuCrZr + Cr / d) CuCrZr + Nb

The LBM processing of the W-coated pure copper powder revealed that the surface treatment causes a very high energy absorption and the processability of the material is thus greatly increased. The parameters obtained for CuNiSiCr and CuCrZr could therefore be applied for the processing this alloy (whereas laser power in the range 380 ÷ 480 W leads to building failure). With 380 W - 800 mm/s – hatch distance 0.055 - 0.066 mm, a porosity < 1% is achieved in the parts (see Figure 93b). With the same parameters, on the other hand, components made of pure Cu without coating have a porosity of ~16 % (see Figure 93a).

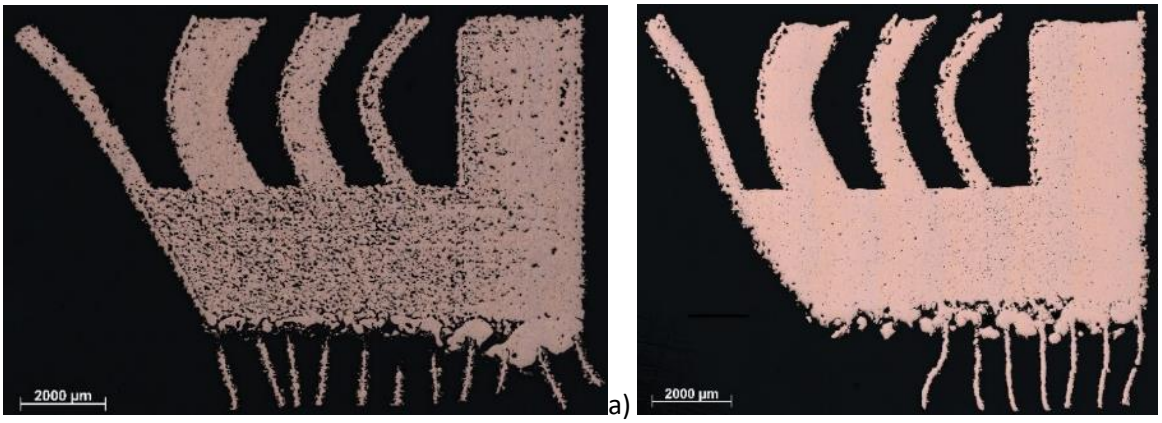

a) b)

Figure 93: Metallographic examination of the test part made of PureCu (process parameter 380 W - 600 mm/s - track spacing = 0.065 mm) – a) PureCu - porosity 15.9 % / b) PureCu + W - porosity 0.9 %

The SEM examination of the pure Cu+W part surface shows a pronounced coating, which contains W, Cu and O (detected by EDX analysis – see Figure 94). Numerous particles of W are also found in the microstructure (Figure 95a), which originate from the partially unmelted W coating. EDX measurements could detect increased contents of Cu, W and O, hence showing also in this case a distribution of oxides (see Figure 95b).

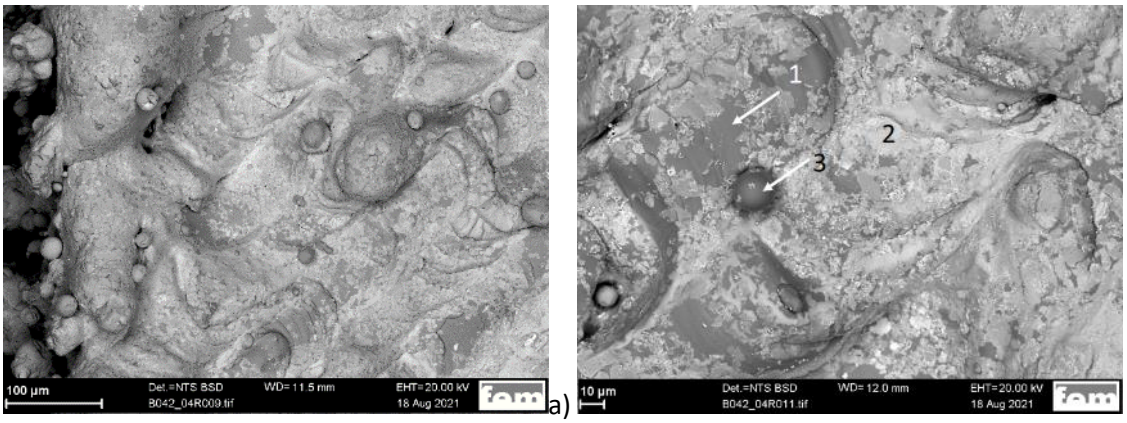

a) b)

Figure 94: SEM examination of the part out of pure Cu+W coating with EDX measurements. a) W containing residues covering the part surface b) EDX Measurement points. 1, 3: Cu matrix - 2: W, Cu and O

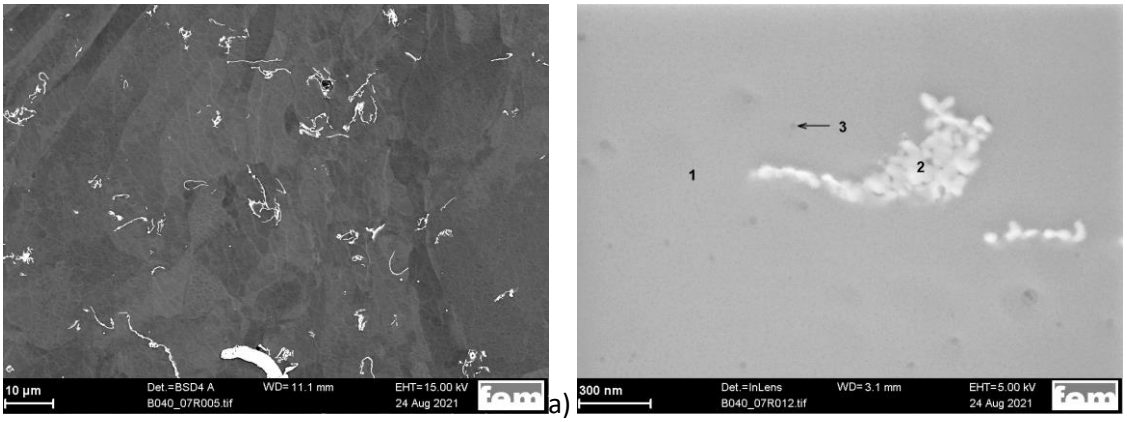

a) b)

Figure 95: SEM examination of the microstructure of the part made of pure Cu+W – a) unmelted W particles visible in the microstructure / b) EDX measurements - 1: Cu matrix + O, 2: increased content of W, Cu and O, 3: increased content of Cu and O

Building of a demonstrator

The geometry of a coil for highly efficient electric motors (designed by the SME and industry project partner Unicorn Engineering GmbH) was chosen for the building of demonstrators. The coil finds its application in an iron-free electrical motor design, with light weight and high efficiency for mobile applications. The part was built both with the CuNiSiCr and CuCrZr alloys. Coated powders could not be used for the manufacturing due to amount of material necessary to fill the building chamber of the Aconity LBM machine.

Figure 96 shows the geometry of the coil and the manufactured parts on the building platform. The metallographic examination showed a good density in the parts (see Figure 97and Figure 98), as was observed in the test geometries, with some occasional bigger pores.

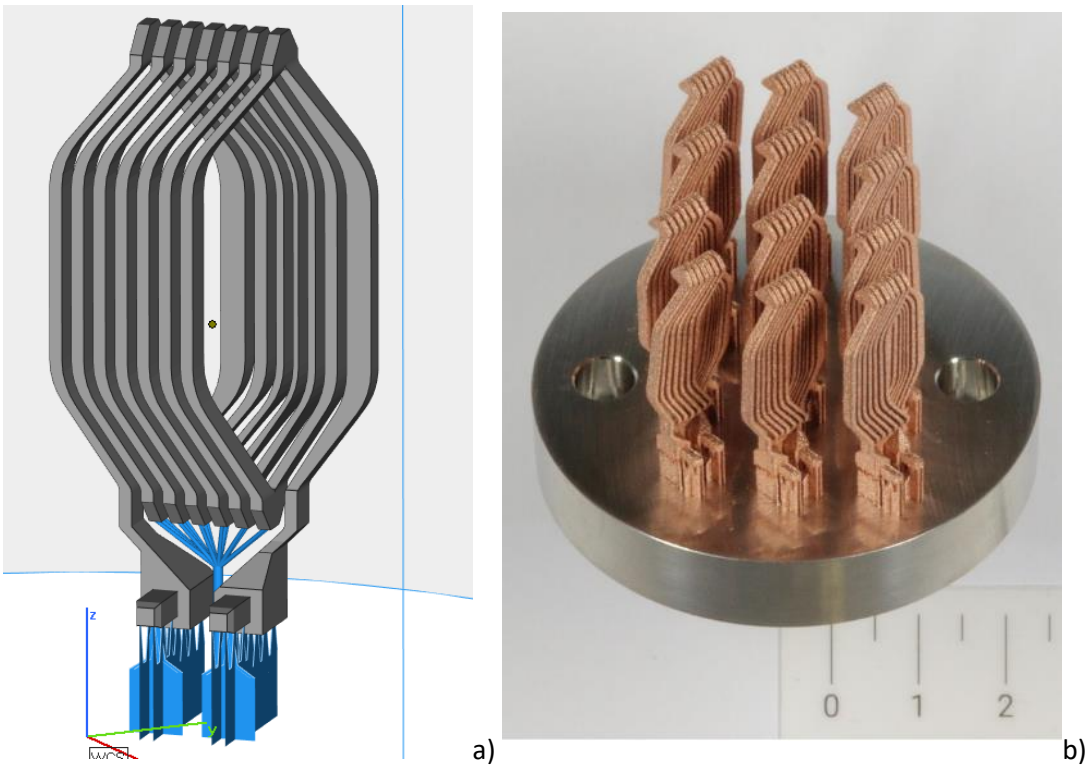

Figure 96: Manufacturing of demonstrator (coil for electric motor) – a) CAD design (design by Unicorn Engineering GmbH) b) manufactured CuCrZr parts on the building platform

Figure 97: Metallographic examination of the demonstrator (coil for electric motor). CuNiSiCr alloy.

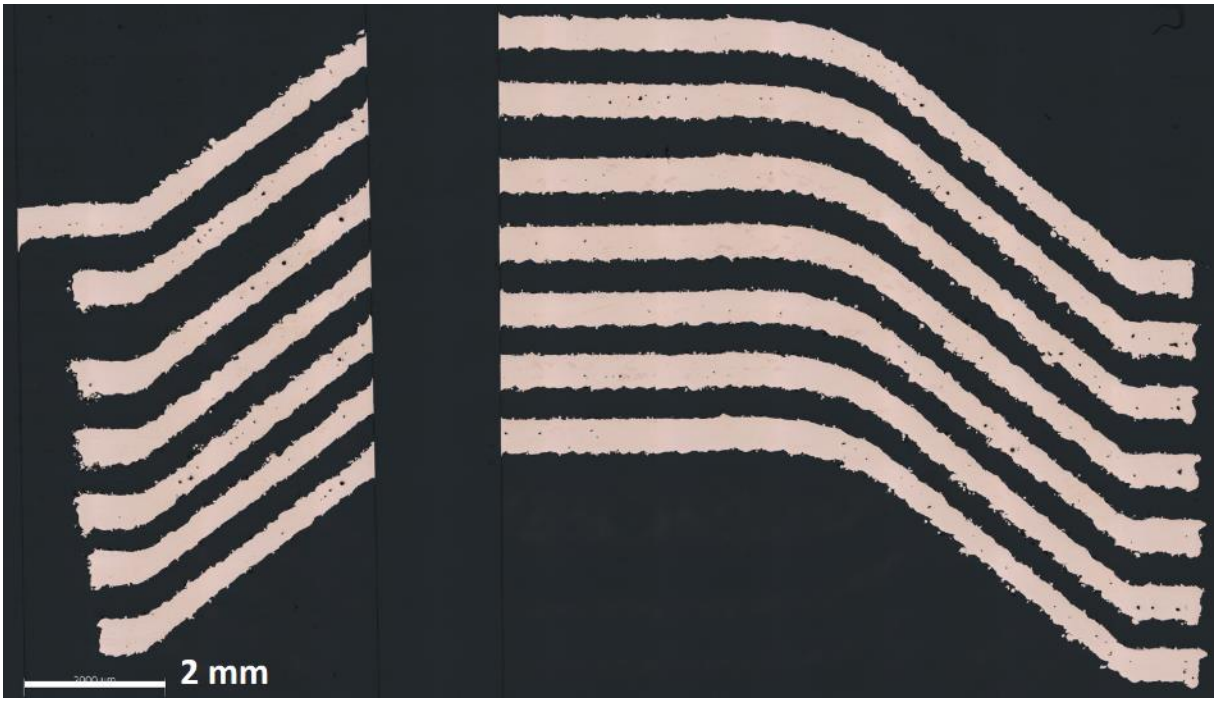

Figure 98: Metallographic examination of the demonstrator (coil for electric motor). CuCrZr alloy.

Investigation on test specimens – measurement of properties

In order to measure the physical properties of the manufactured materials, small plates (14 x 14 x 2.8 mm) were built with the optimal laser parameters. Vickers hardness and electrical conductivity were measured on such plates for three material conditions: as-built, solution annealed, and solution annealed and subsequently aged. The electrical conductivity was measured with the eddy current testing (Helmut Fischer Sigmascope SMP350) on grinded samples.

Test bars were also built for the production of tensile test specimens by machining (see Figure 99), which were also available and were tested in the before mentioned three material conditions (as-built, solution annealed, and solution annealed and subsequently aged). CuCrZr and CuNiSiCr samples were manufactured with 0° - (45° only CuCrZr) - 90° angle, while samples out of coated alloy were produced only with 0° orientation (due to the quantity of material available). Results of the tensile test were then evaluated and compared.

The measured values for hardness HV1 and electrical conductivity on plates of all materials (CuNiSiCr / CuCrZr with Nb/Cr coating and pure Cu with W coating) and conditions are listed in Table 11. The chart in Figure 100 shows a graphical comparison of the measured values. Properties of the CuNiSiCr / CuCrZr AM parts after solution annealing and aging match and exceed the data sheet values of the manufacturer (respectively 186 HV1 - 38 % IACS and 115 HV1 – 75,8 % IACS). Values of the commercially available CuNiSi sheet (202 HV1 and 55 % IACS) were compared with the additive manufactured material: AM parts show higher hardness (248 HV1) but lower conductivity (40 % IACS). Concerning the effect of the heat treatment, the AM condition is similar to the solution annealed condition, except for CuCrZr + Nb (for which solution annealing drastically improves electrical conductivity - from 30 to 66 % IACS). After solution annealing and aging coated and uncoated CuCrZr / CuNiSiCr show similar conductivity and hardness (see bold formatted values in Table 11). Hence the coating doesn't seem to improve the physical properties of the additive manufactured material: this is probably due to the high oxygen content in the powder, which has a negative effect on said properties.

After solution annealing and aging the AM part made of pure Cu + W reaches an el. cond. of 96 %IACS, which is in accordance with the low porosity (<1 %) obtained in the part.

Results of the tensile tests for the CuCrZr alloy are shown in Figure 101 to Figure 103. The orientation has a strong influence on the properties, and the samples built in 0° (parallel to the building plate) feature the highest values (Figure 101). The solution annealing reduces the yield strength Rp0,2 and increases the tensile strength Rm and the elongation at break (Figure 102). Aging doubles the tensile strength Rm and the yield strength Rp0,2, while having a minimal impact on the elongation at break (Figure 102). The coated alloys (with Nb/Cr) do not show improved properties in comparison to the original one: the Cr coating delivers similar values, while the Nb coating features slightly lower ones (Figure 103). Here it has to be noted that the comparison takes place between different building angles (0° for uncoated and 90° for coated): as mentioned before, the 90° building angle shows generally inferior properties than the flat 0° angle. The metallographic investigation on already tested samples could in fact show a higher porosity amount in the 45° and 90° building angle when compared to the 0° one (see Figure 104). The porosity tends to align parallel to the building plate, thus weakening the resistance of the sample along its longitudinal axis (which explains the lower tensile strength and elongation at break of the 45° and 90° building angle).

Additionally, it was noted (through the analysis of the stress-strain curves) that the results present a scattering, strongly dependent on the position of the sample on the building plate. The gas flow over the building plate during the LBM process is from right to left, and this causes the deposition of

smoulder (formed by the vaporization of volatile elements) on the parts placed on the left side (Figure 105), impacting their quality. As already shown in Figure 99a, three samples at a time were built in the 0° angle: the ones on the left and in the middle show always a lower elongation at break (because of their lower quality) than the one build on the right side. The different quality of the samples is noticeable in the SEM pictures of the fractured surface (see Figure 106): the samples on the left shows a higher amount of lack of fusion defects and unmelted powder particles trapped in bulk material. This reflects on the lower elongation at break compared to the sample on the right side (respectively curves B055 -1 and B055-3 in Figure 107). The porosity observed in these samples is higher than the one obtained in the test parts used in the parameter optimization. This can be explained considering that the surface to be melted is in these case much bigger, and the problem of smoulder formation and deposition has a stronger impact on the part quality. The small building plate (55 mm diameter) is not suitable for building parts with thicker walls / bigger surfaces (such as the test bars). The problem was not encountered during the building of the demonstrator, since the geometry featured thin walls and small surfaces. A bigger builder plate (i.e. 140 mm diameter), and the consequent amount of powder material would be required.

For CuNiSiCr, the influence of the orientation on the properties is not as big as for CuCrZr, whereas 90° shows slightly lower values for tensile strength Rm and yield strength Rp0,2 than 0°, and a slightly higher elongation at break (Figure 108). The solution annealing reduces the tensile strength, while the aging notably increases it (together with the yield strength) (Figure 109). Concerning the coated alloys, the same considerations made on the lack of improvements for the coated CuCrZr can be repeated for the CuNiSiCr, as seen in Figure 110. This can be explained by considering the high oxygen amount contained in the coated powder and the formation of brittle oxides during the LBM process, which weaken the sample. Figure 111 shows the SEM investigation with EDX measurement of the fractured surface on one CuNiSiCr + Nb sample. The measurement in a brittle fracture area (point 1) detects an increased amount of Nb and O, while the measurement in a ductile fracture area (point 2) detects the alloying elements Cu, Ni, Si, Cr, and only reduced amounts of Nb and O. Figure 112a shows an overview of a lack of fusion defect (i.e. a cavity) in the fractured surface. The lower half of the picture presents a raw surface and seems to be covered with a fine residue, which is believed to be vaporized material redeposited on the part during the melting of the current (or previous) layer (i.e. the before mentioned smoulder). The upper half of the area in the picture has a smoother appearance, since the molten material doesn’t show residues on its surface. Figure 112b shows a higher magnification at the interface of the two different areas: in the lower right corner, an insufficient and partial wetting of the smoulder zone by the melt front is clearly visible. Figure 113 shows EDX measurements which were conducted on these two areas: the melt front (point 8) features increased content of Nb and O, while the smoulder-covered area (point 7) shows increased content of Cu, Nb and O. Hence both areas contain oxides.

The results for the specimens built with pure Cu coated with W are shown in Figure 114. The solution annealing doesn’t significantly change the properties of the as-built state: the tensile strength Rm is slightly improved, while the yield strength Rp0,2 decreases minimally.

a)

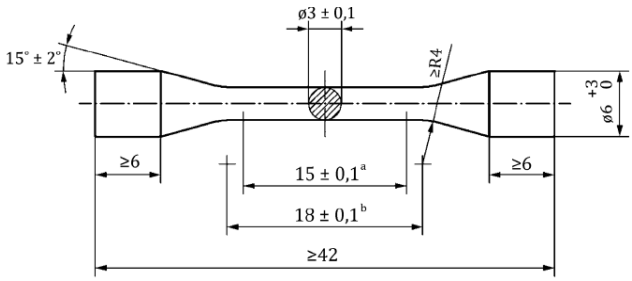

b)

Figure 99: a) Example of CuCrZr test bars built with 0° orientation b) Geometry of the final tensile test specimen with dimensions in mm

Table 11: Measured physical properties on as-built and thermal treated test plates

Material and condition	*Electrical conductivity [%IACS]*	*Hardness [HV1]*
CuCrZr as-built	26,7	77
CuCrZr solution annealed	39,4	66
CuCrZr SA + aged	**87**	**123**
CuCrZr+Cr as-built	23,2	65
CuCrZr+Cr solution annealed	41,7	63
CuCrZr+Cr SA + aged	**87,6**	**120**
CuCrZr+Nb as-built	30,3	116
CuCrZr+Nb solution annealed	65,9	84
CuCrZr+Nb SA + aged	**91,9**	**96**
CuNiSiCr as-built	15,6	124
CuNiSiCr solution annealed	17,5	102
CuNiSiCr SA + aged	**40,5**	**248**
CuNiSiCr+Cr as-built	10,6	95
CuNiSiCr+Cr solution annealed	18,9	86
CuNiSiCr+Cr SA + aged	**38,3**	**237**
CuNiSiCr+Nb as-built	14,9	109
CuNiSiCr+Nb solution annealed	19,1	97
CuNiSiCr+Nb SA + aged	**41,9**	**230**
PureCu + W as-built	89,2	72
PureCu + W SA (600°/60min)	**95,9**	**68**

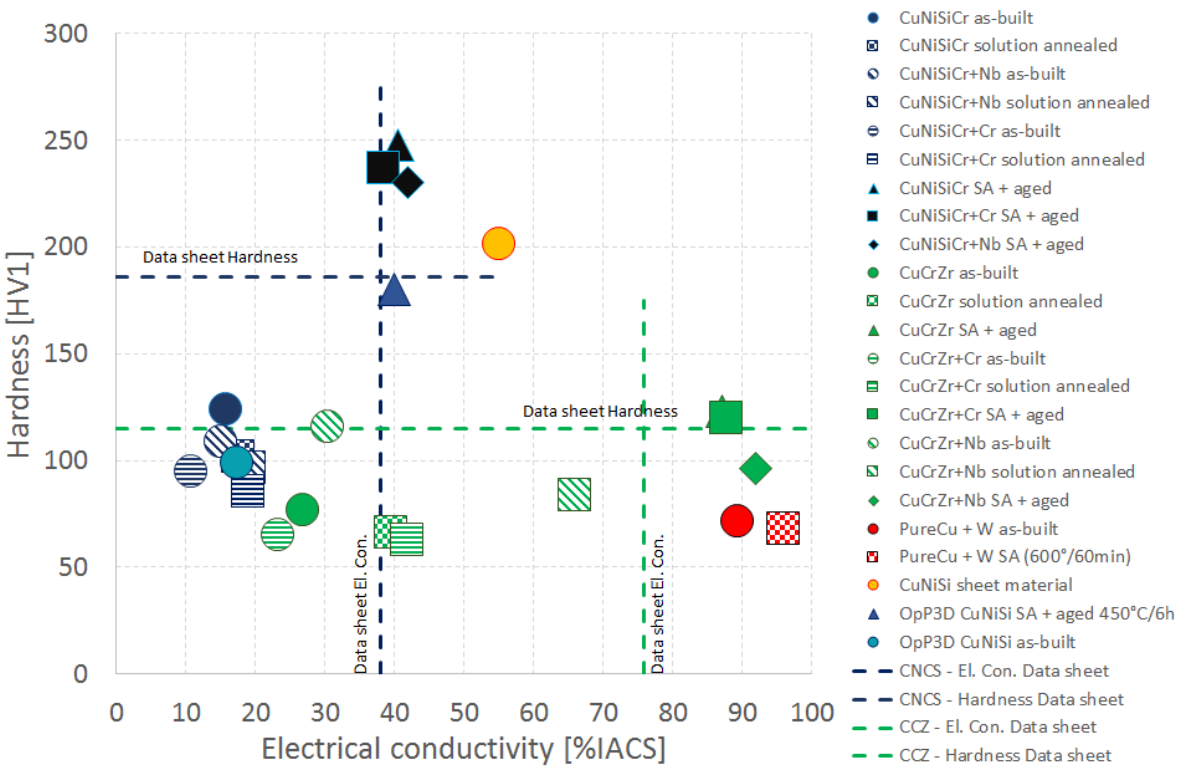

Figure 100: Graphical representation of the measured physical properties (Vickers hardness and electrical conductivity) on the test plates in as-built and thermal treated condition

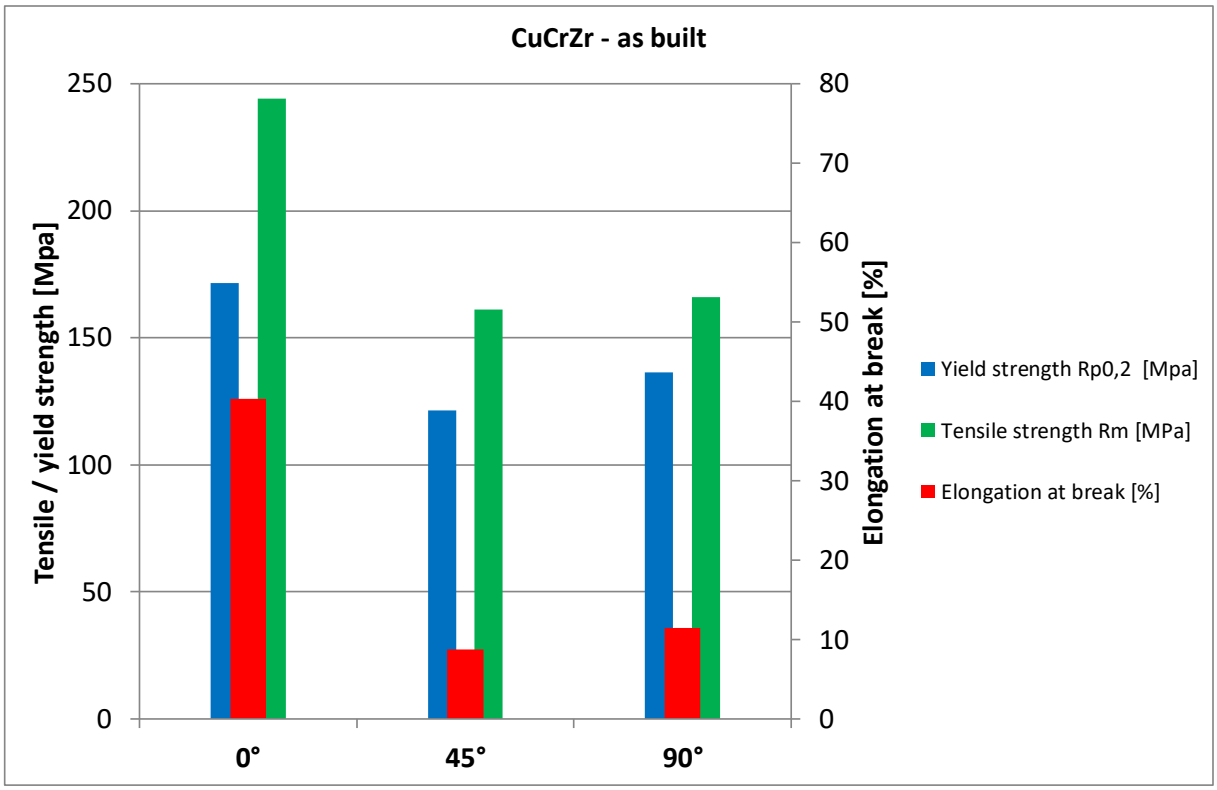

Figure 101: Tensile test results: comparison of the uncoated CuCrZr alloy in all three building orientations (0°, 45° and 90°)

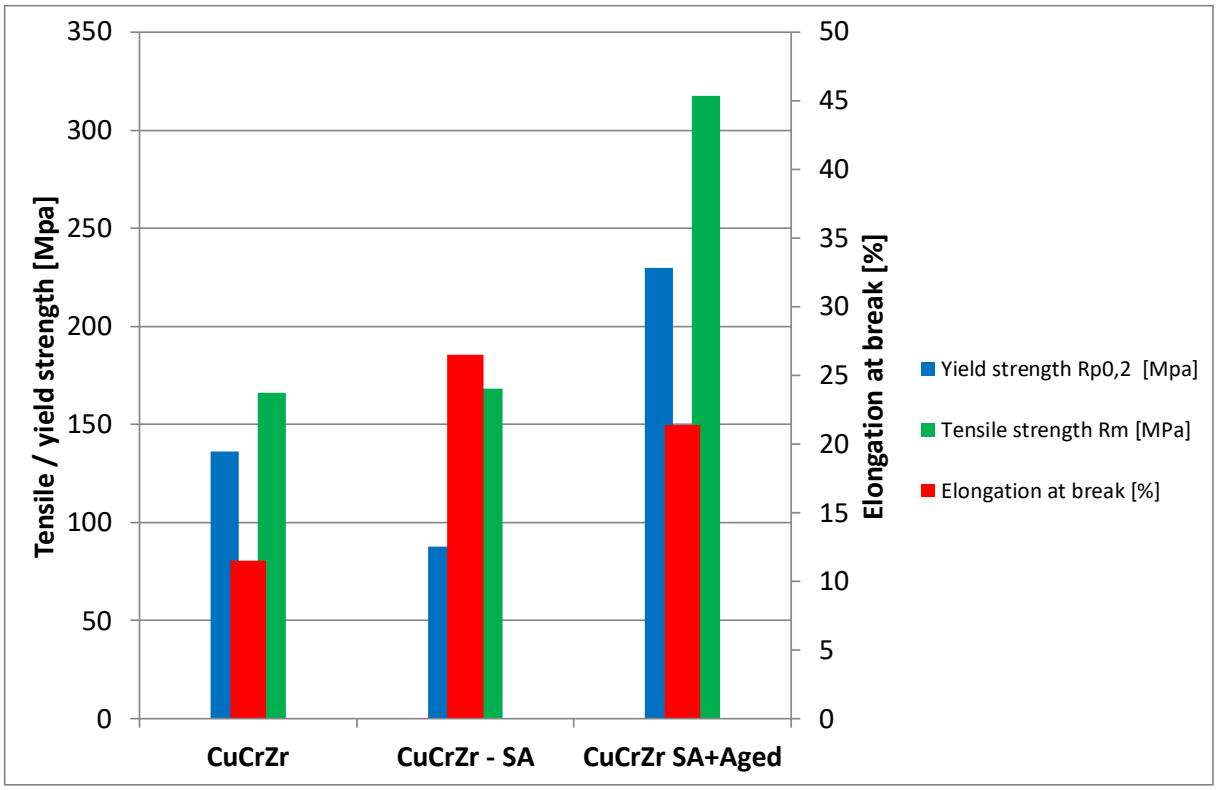

Figure 102: Tensile test results: comparison of the uncoated CuCrZr alloy in all three conditions: as built, after solution annealing, and after solution annealing and aging. Building angle 90°

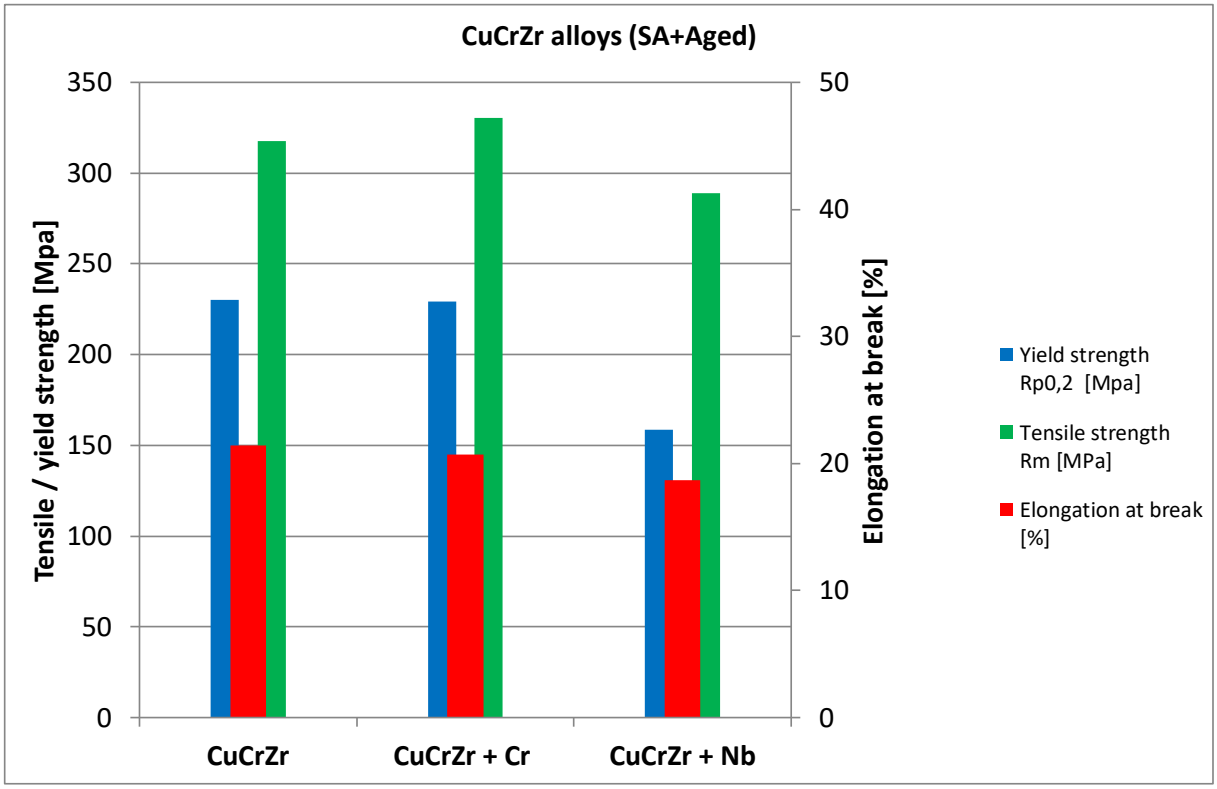

Figure 103: Tensile test results: comparison of the uncoated and coated CuCrZr alloys after solution annealing and aging. Building angle 0° (coated alloys) and 90° (uncoated alloy)

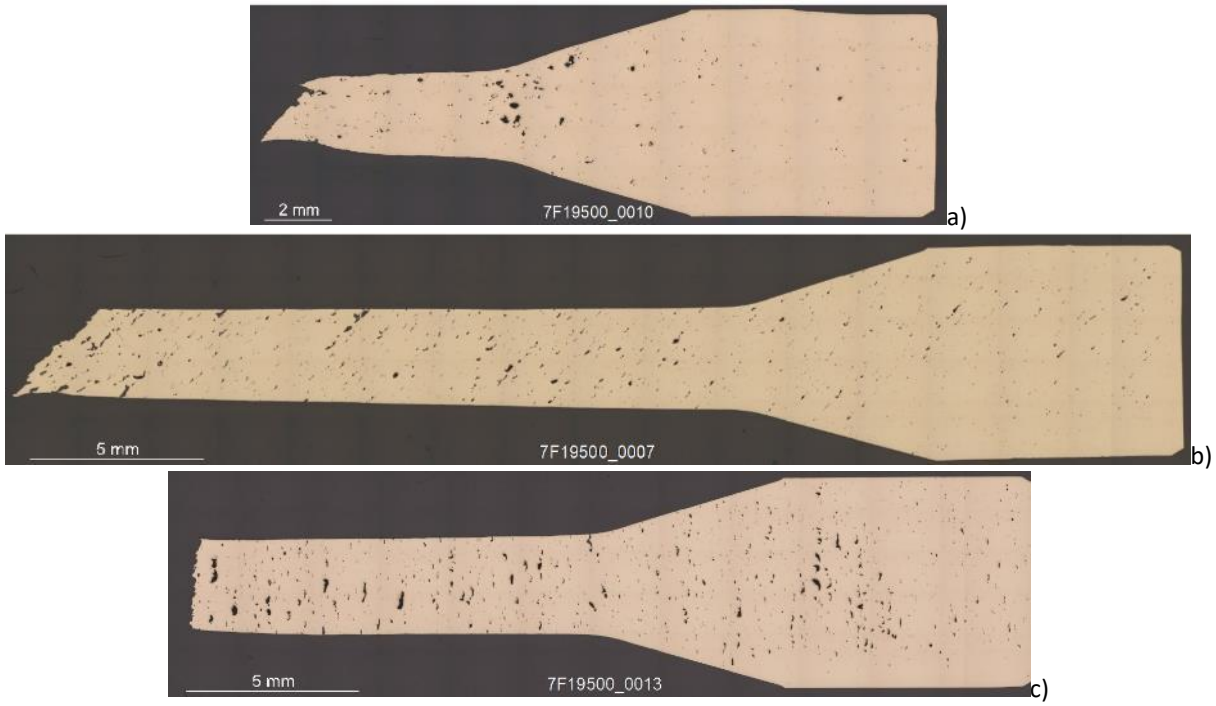

Figure 104: Metallographic investigation on CuCrZr tensile specimens after mechanical test. a) 0° building angle b) 45° building angle c) 90° building angle

Figure 105: LBM process - snapshot after the laser exposure - smoulder deposition on the parts increasing from right to left (according to the gas flow direction)

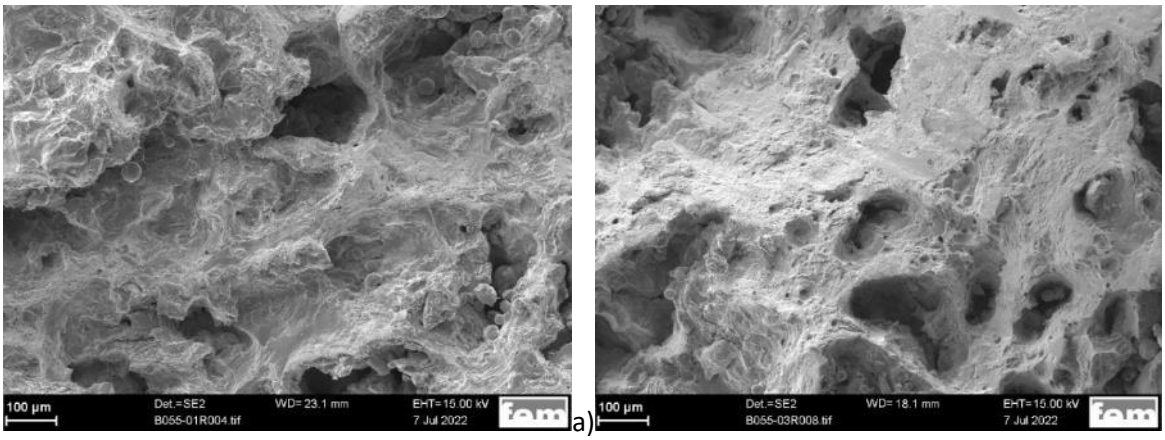

Figure 106: SEM investigation of the fractured surface of two CuNiSiCr + Nb samples after tensile test. a) Sample B055-1 (left position on the building plate) b) Sample B055-3 (right position on the building plate)

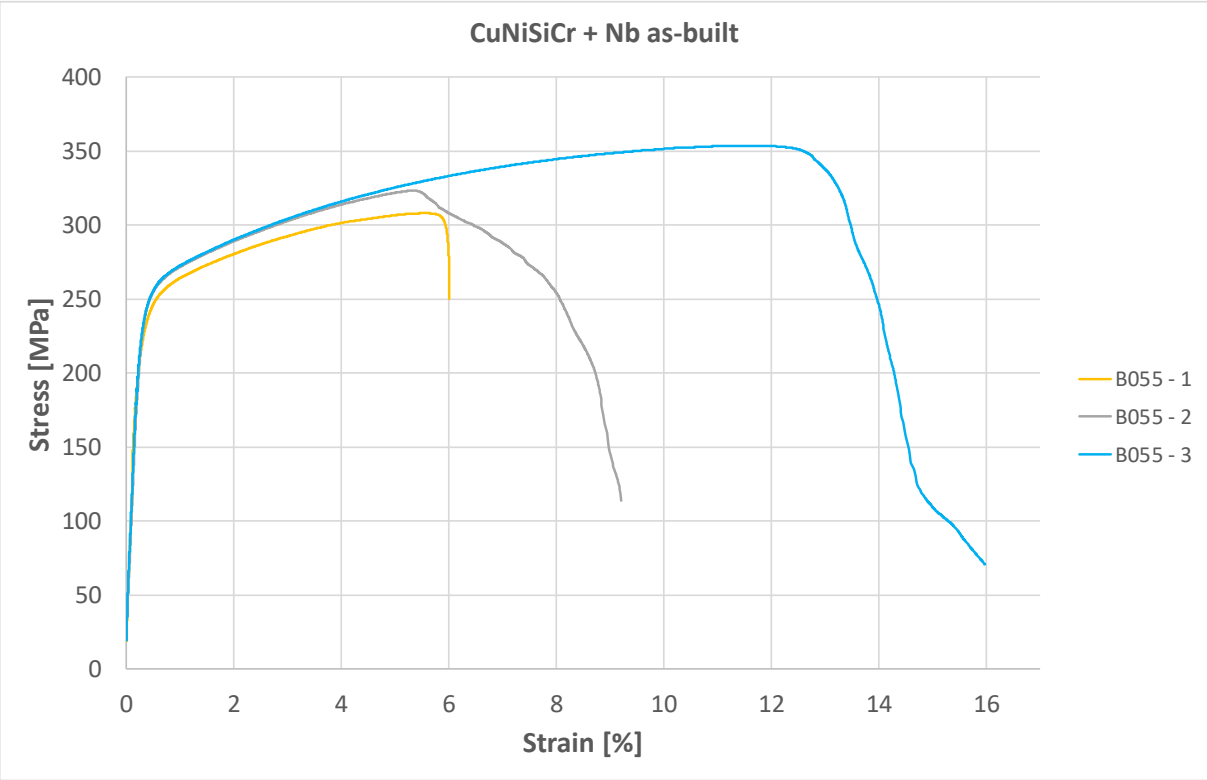

Figure 107: Stress-strain curve for the CuNiSiCr + Nb samples built in the trial B055: Sample B055-1 (left position on the building plate) / Sample B055-2 (middle position on the building plate) / Sample B055-3 (right position on the building plate)

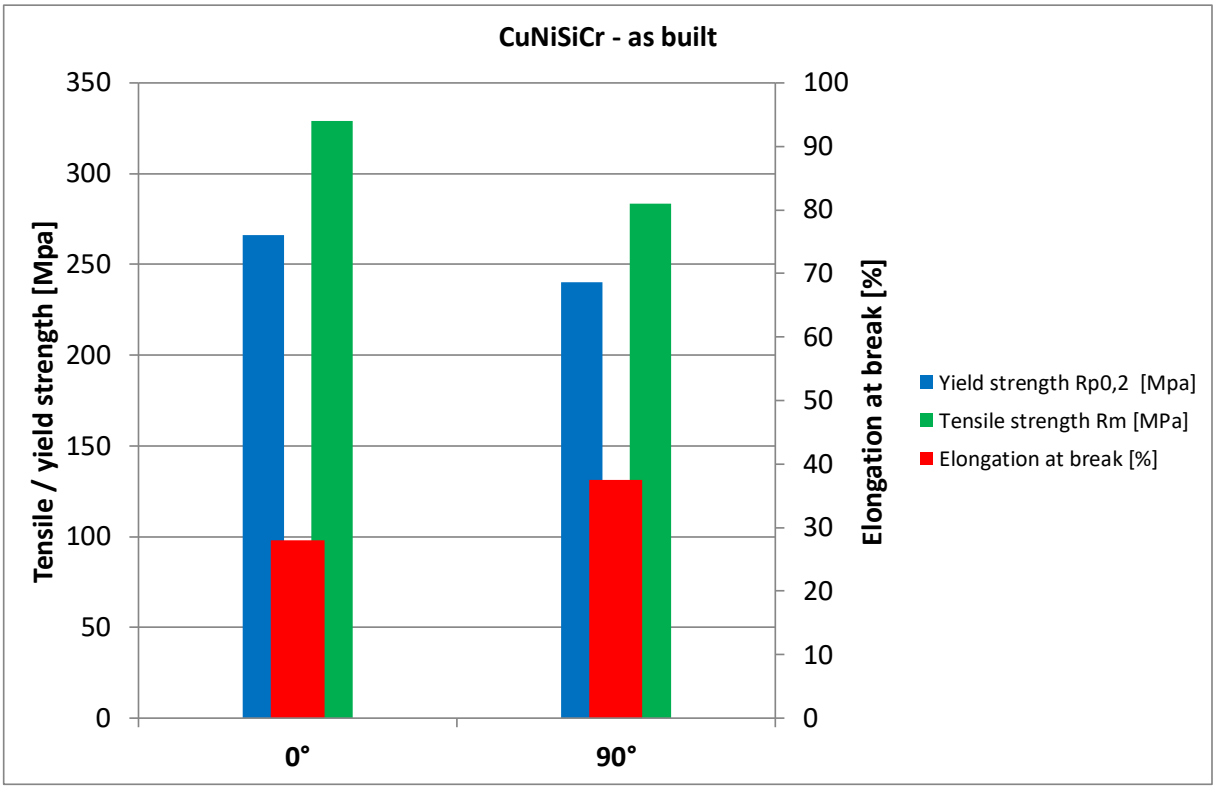

Figure 108: Tensile test results: comparison of the uncoated CuNiSiCr alloy in two building orientations (0° and 90°)

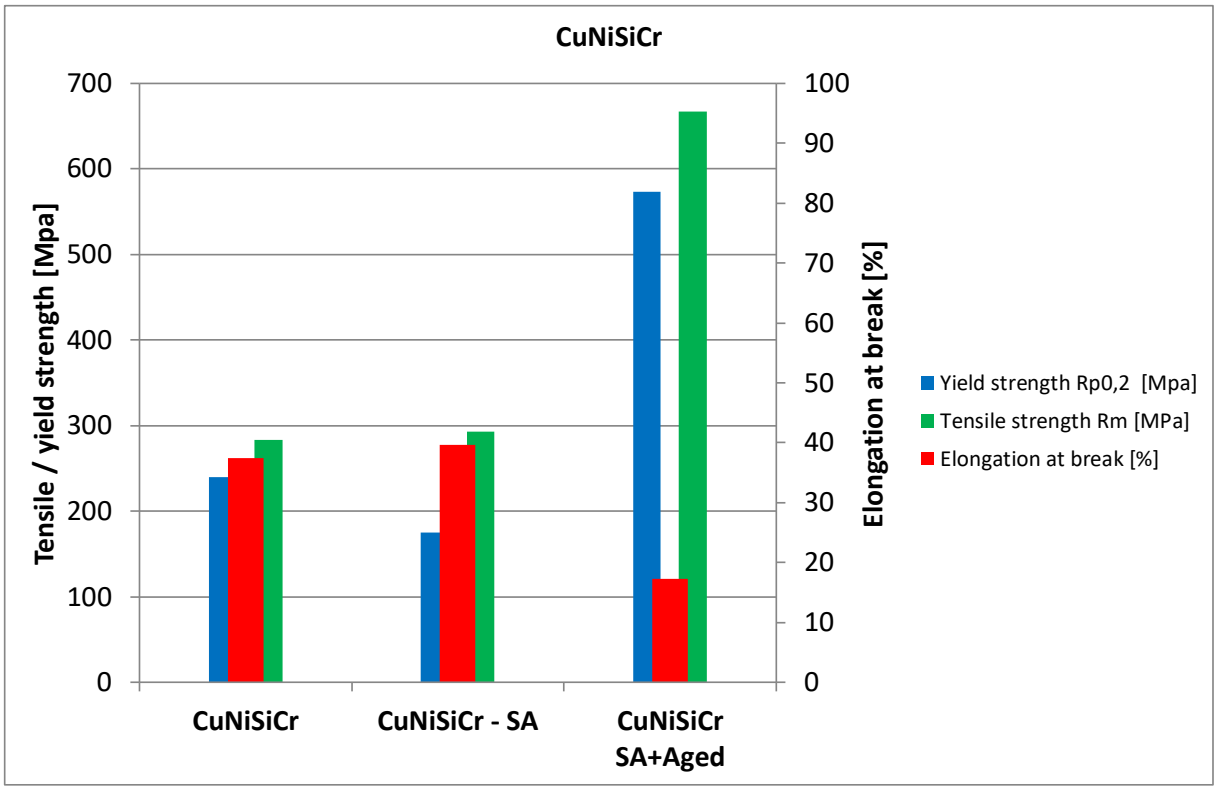

Figure 109: Tensile test results: comparison of the uncoated CuNiSiCr alloy in all three conditions: as built, after solution annealing, and after solution annealing and aging. Building angle 90°.

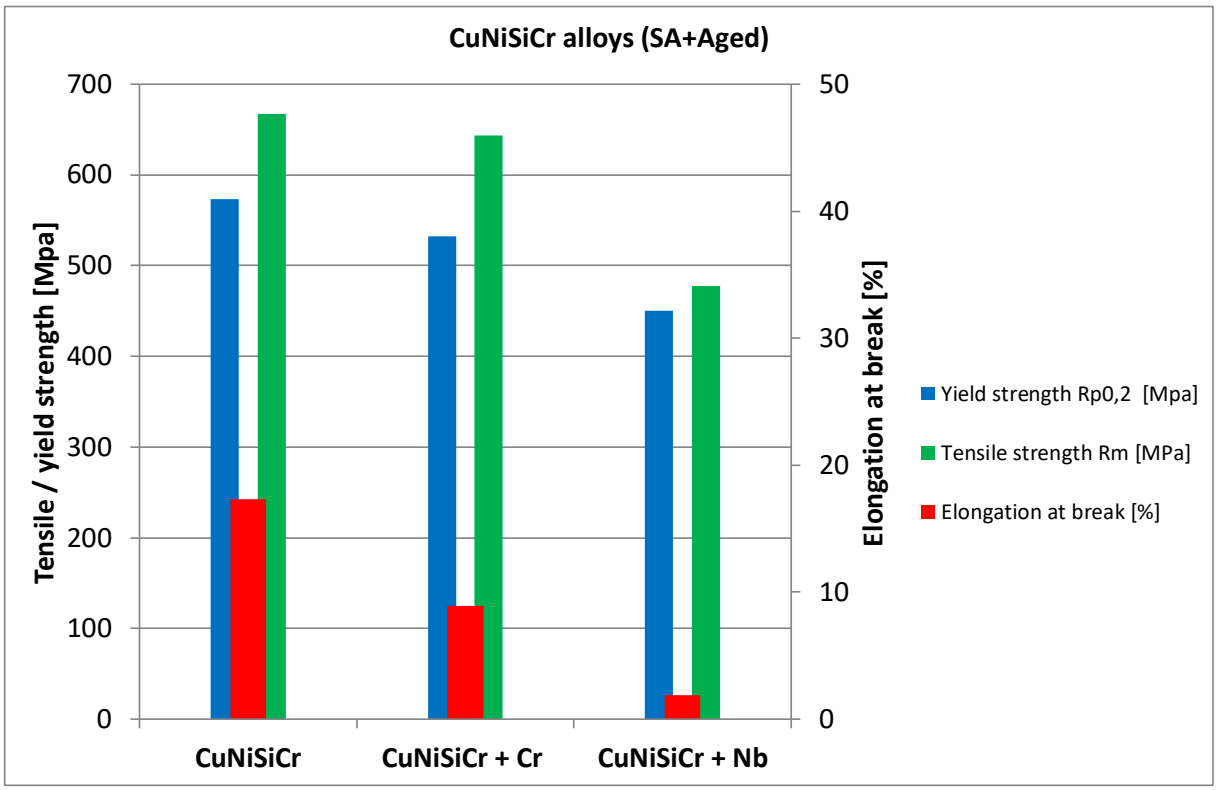

Figure 110: Tensile test results: comparison of the uncoated and coated CuNiSiCr alloys after solution annealing and aging. Building angle 0° (coated alloys) and 90° (uncoated alloy).

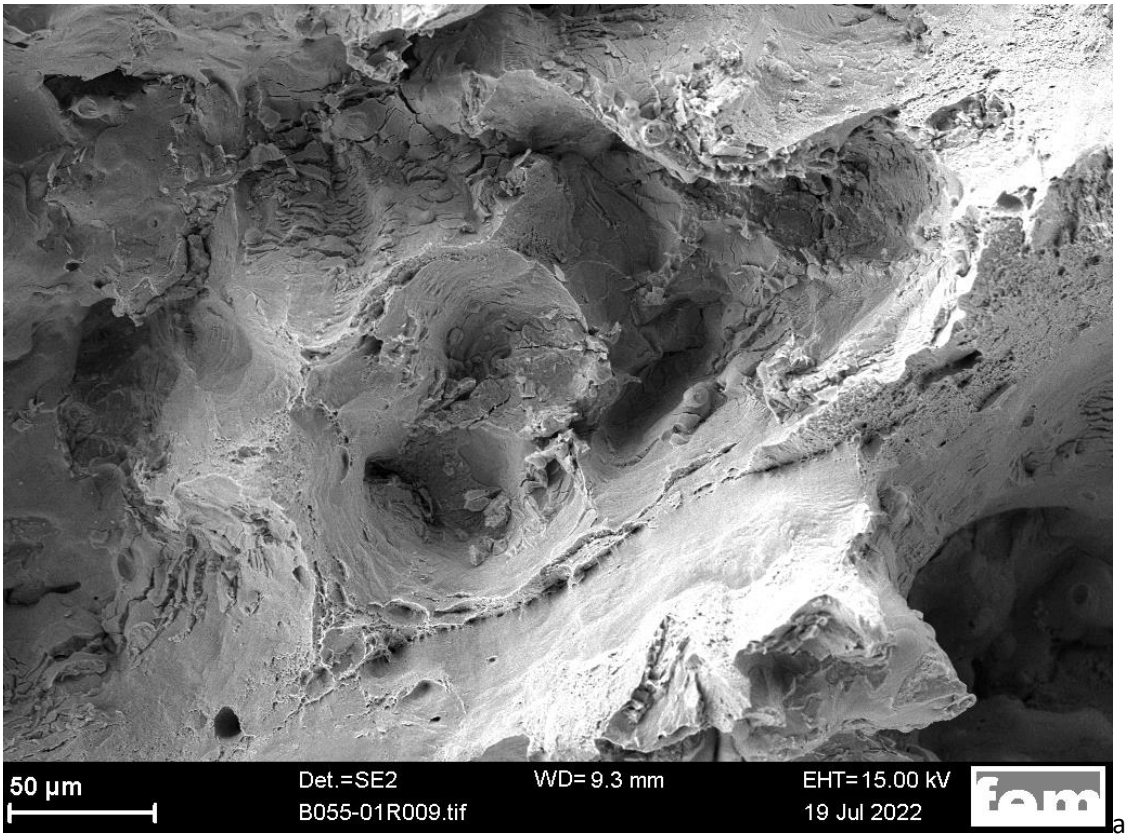

a)

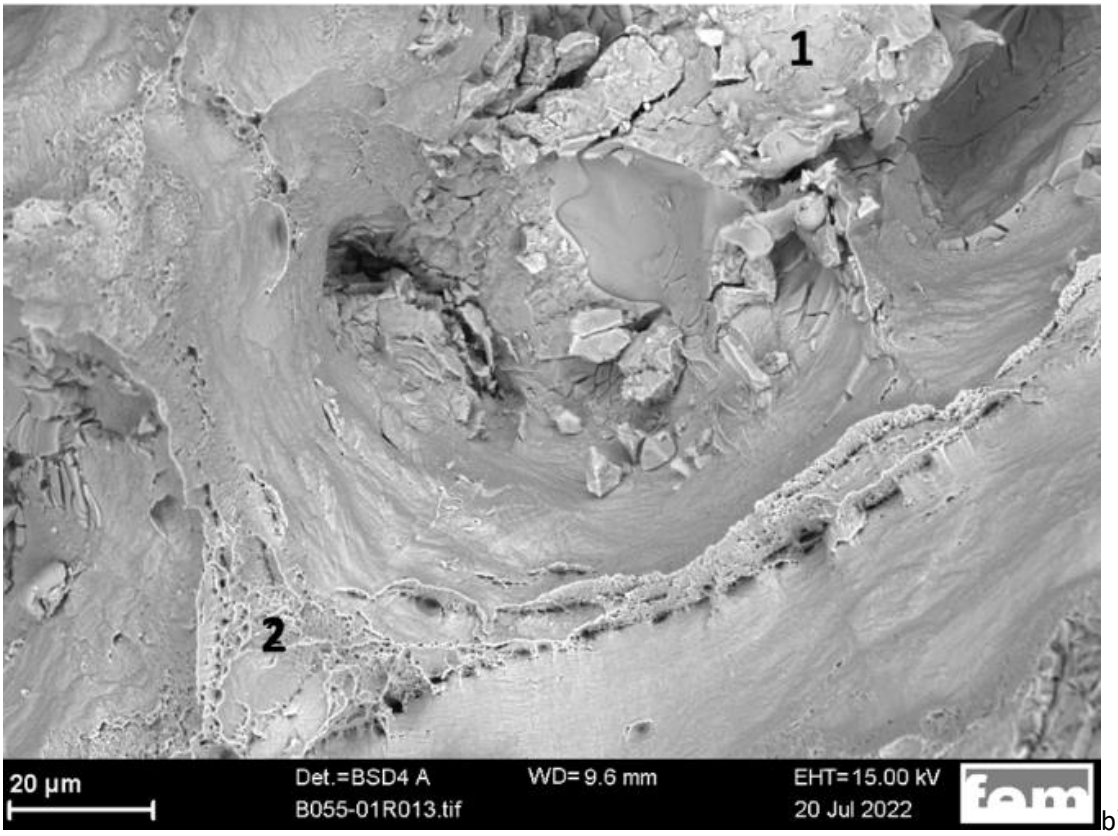

b)

Figure 111: SEM investigation of the fractured surface of a CuNiSiCr + Nb sample (a) - with EDX measurements (b) - point 1: increased amount of Nb and O / point 2: Cu, Ni, Si, Cr, and only reduced amounts of Nb and O

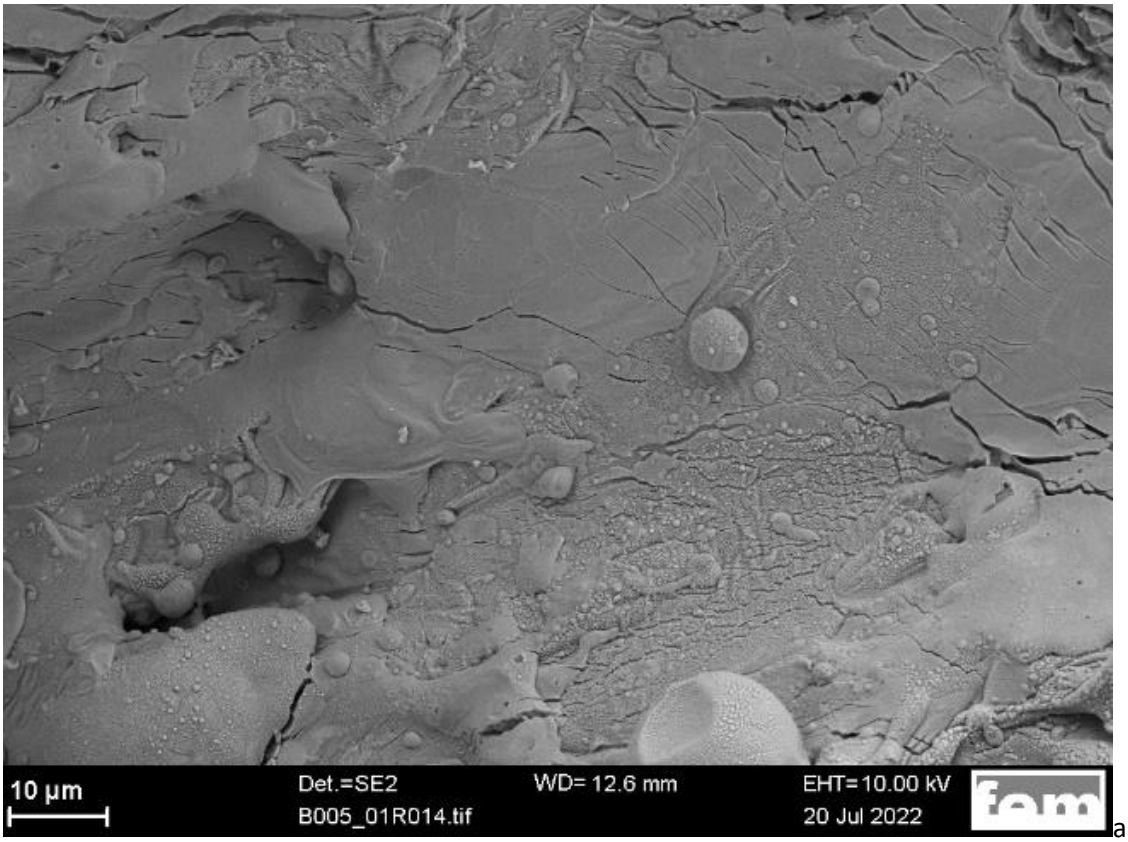

a)

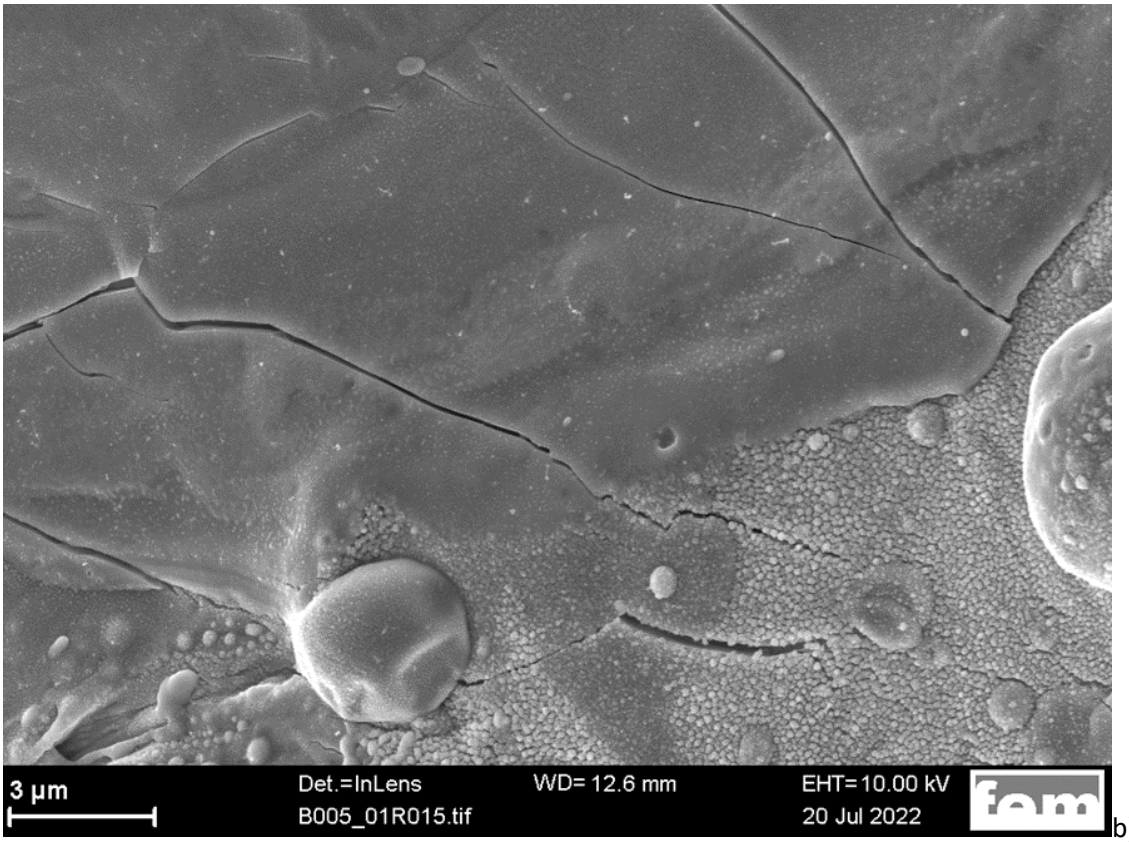

b)

Figure 112: SEM investigation of a lack of fusion defect in the fractured surface of a CuNiSiCr + Nb sample a) overview b) detail of insufficient wetting of the smoulder covered area

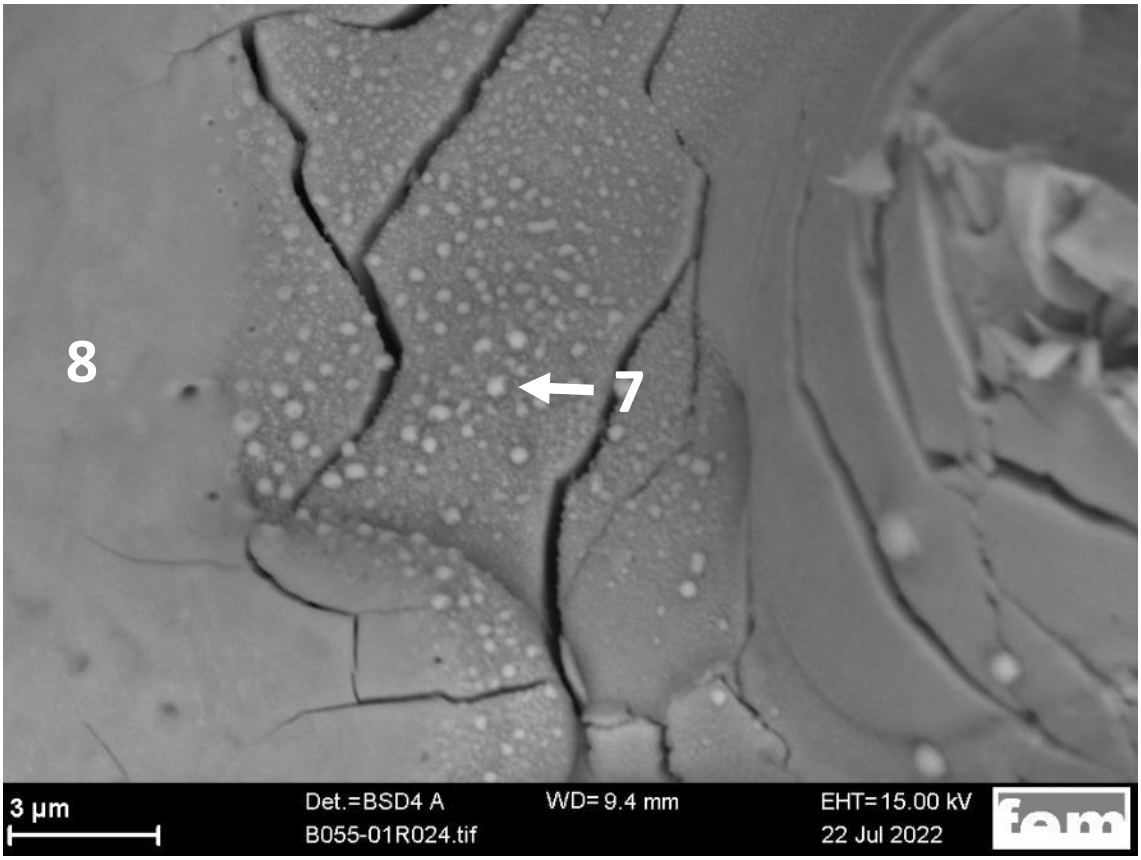

Figure 113: EDX Measurement of a lack of fusion defect. Point 8: Increased content of Nb and O / Point 7: Increased content of Cu, Nb and O

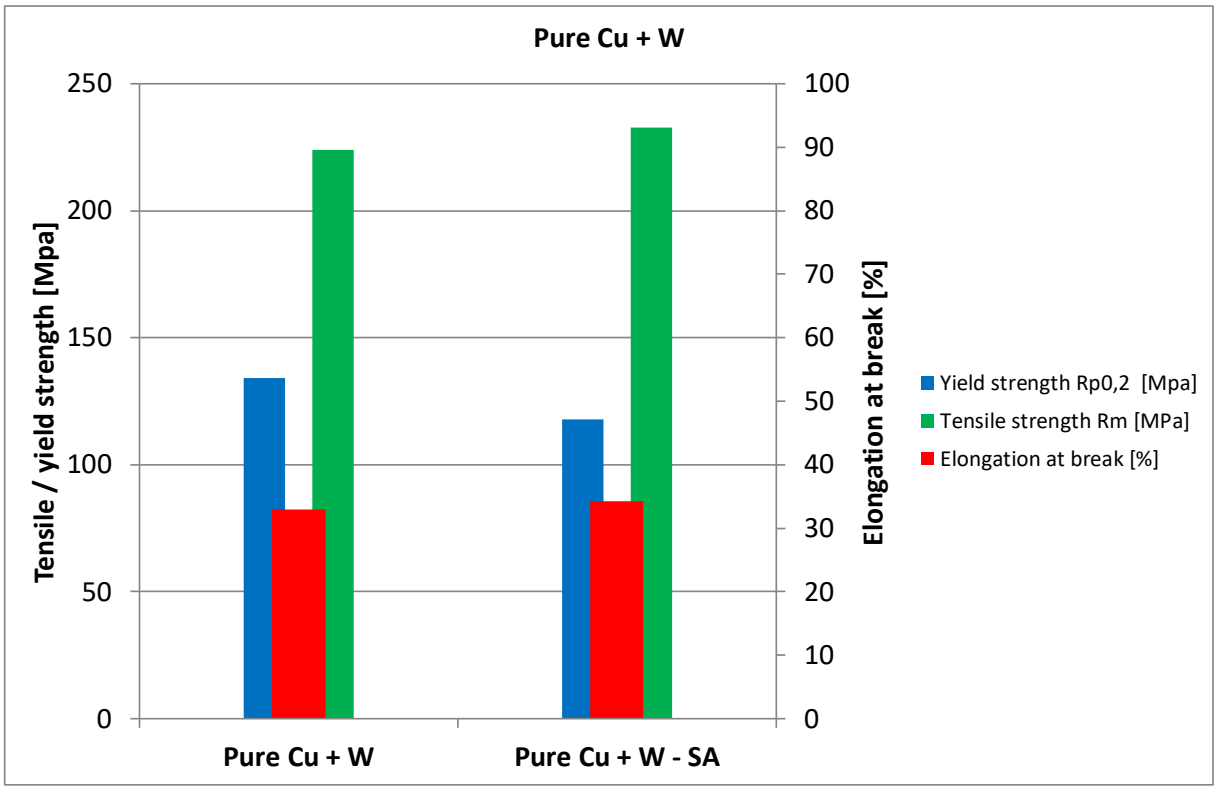

Figure 114: Tensile test results: comparison of the W-coated pure Cu in as-built state and after solution annealing. Building angle 0°.

3.1.5.2 Performed activities – UMSICHT

The Cu-W composite powders generated via the mechanical route and the two-step atomization (see section 3.1.3.1) have been processed via LPBF on a 3D Systems ProX200 system. As test bodies, cubes in different geometries have been generated and investigated after preparing individual micro-sections. The photo series in Figure 114 is exemplary for the used powder (here 3 vol.-% W / mechanical manufacturing route), produced cubes and the resulting microstructure.

After the necessary parameter optimization for the parts manufacturing, dense cubes could be obtained with porosities as low as 0.4 % for the mechanically manufactured Cu-W 3%. Surprisingly, also the powder from the two-step atomization with a remarkably lower coverage of W on Cu could be successfully processed. However, the achieved densities were less than the ones from the mechanical route with remaining porosities down to 1.5 % (Figure 115).

The W particles form clusters inside the compacted matrix which indicate that there is only a weak rearrangement/short movement distances of W inside the Cu melt pool. The tungsten is not melting at the conditions applied.

In a summary of these investigations one can state the following:

- Composite Cu-W powders can be successfully processed via LPBF to form dense parts.
- Quite low energy densities can be applied that are state-of-the-art for many existing manufacturing systems (300 W Laser @ 1065 nm wave length).
- The two-step atomization process has still to be optimized. This process would have remarkable advantages, if compared to the mechanical route, namely
    - More cost efficient do the direct formation during Cu powder production
    - Less risks for picking up impurities (oxygen, milling media)

In total, the results are very promising for being applied in future composite powder production for enhancing the behaviour during LPBF processing as well as for manipulation of parts properties. For the Cu LPBF parts manufacturing they open new potentials.

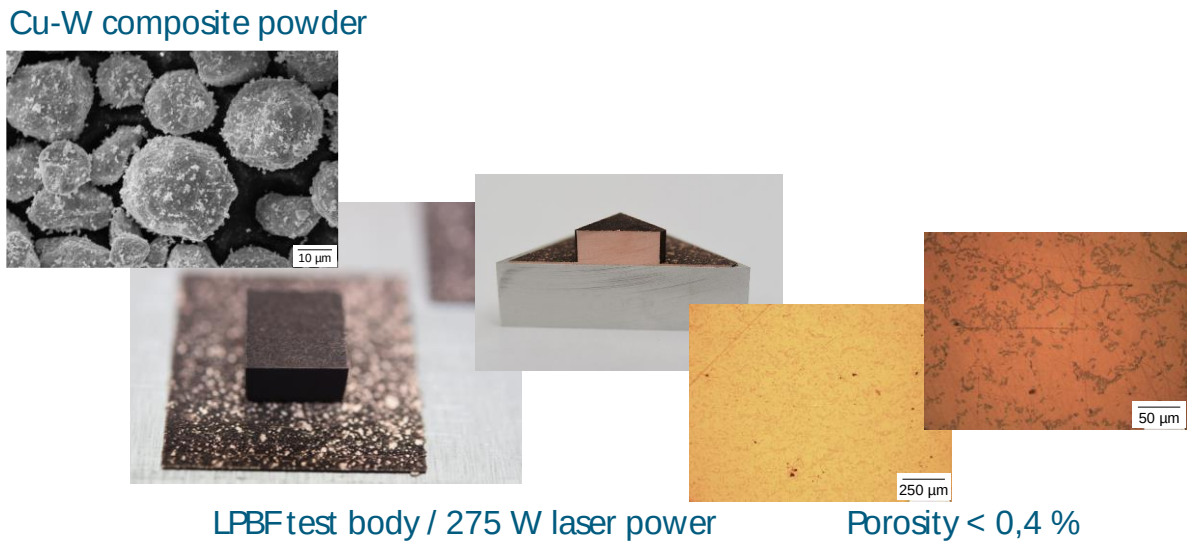

Figure 115: Test body and microsection from a manufactured cube by using mixed/milled Cu with 3 vol.-% W.

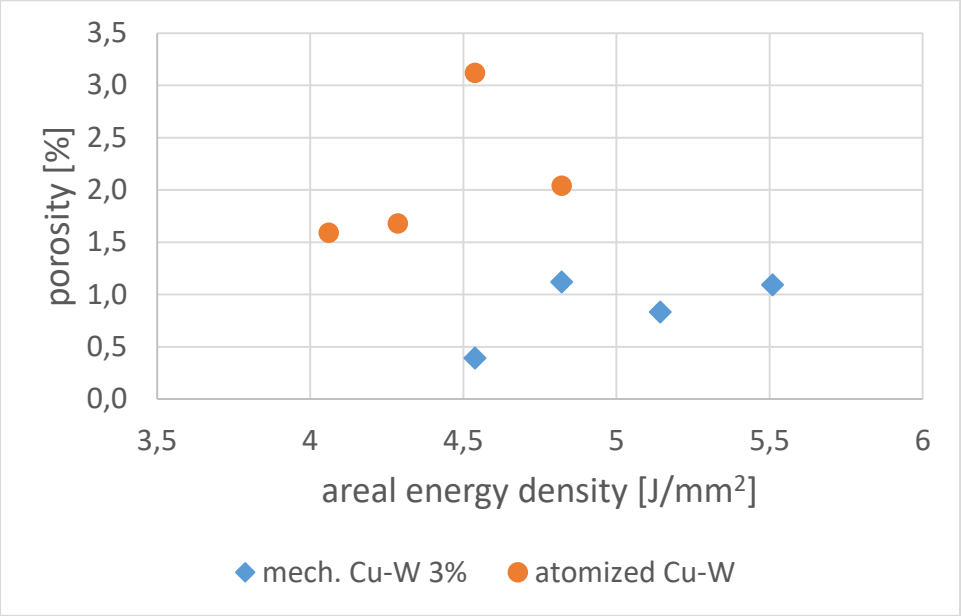

Figure 116: Achieved densities for LPBF manufactured test bodies with milled (3 vol.% W) and with two-step atomized Cu-W (<1.5 vol.-% W) powders

3.1.5.3 Performed activities – Sirris

- Electron Beam Melting (EBM) of pure Cu

Copper printing with EBM required to follow a specific training supplied by Arcam (the equipment supplier). This training aims at improving the understanding the specific beam strategies that can be tuned to obtain the material densification.

Figure 117 shows a comparison between EBM and LBM. The most significant difference is the preheating of the powder to make the cake. This presintered state is obtained by defocusing the beam on each layer. This additional preheat stage at each layer increases significantly the complexity of the process (see Figure 118).

The training had also to address the specific strategy related to the old version of model used in the machine (EBM control 3.2). No cooling phase can be introduced in the layer current profile so the machine is hard to stabilize at low temperature.

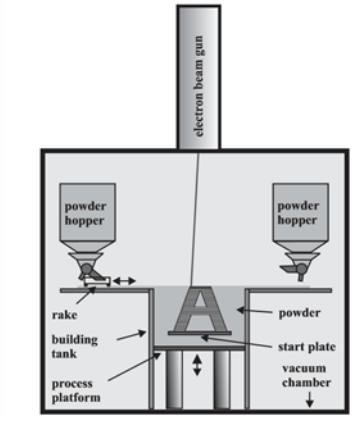

Electron beam powder bed ALM	Laser powder bed based ALM
vacuum	Inert gas: Argon
Electron beam	laser
Powder size ~60 µm	Powder size: ~25 µm
layer: 50-90 µm	Layer: 30 to 60 µm
Presintering of the powder	No presintering
Heating of the last layer (750°C)	Heating through the build plate
Low internal stresses	High internal stresses
Supports strategy : low complexity	Support strategy: High complexity

Figure 117: Characteristics of EBM in comparison to LBM

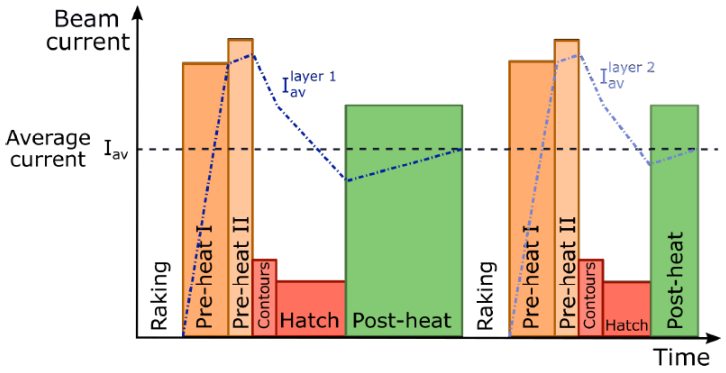

Figure 118: Different stages of the EBM process

Copper powder characterisation

Size distribution

The typical powder for EBM has a grain size ranging from +45µm to -106 µm. In this project, the focus was on a powder with typical grain size: +45-95 µm.

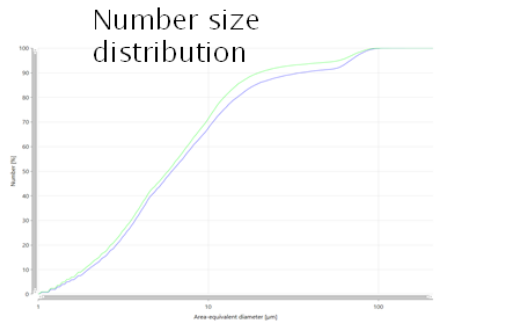

Sample	Nombre de particules	d10 [µm]	d50 [µm]	d90 [µm]
ADD1044_1 (bleu)	18173	1,995	6,123	35,278
ADD1044_2 (vert)	18170	1,858	5,814	19,888

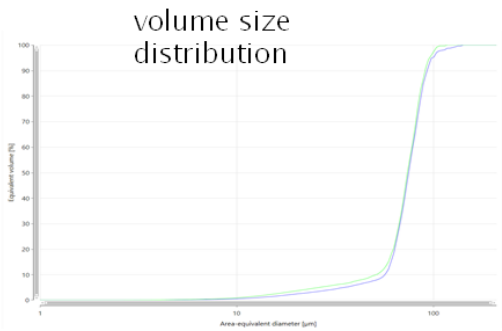

Sample	Nombre de particules	d10 [µm]	d50 [µm]	d90 [µm]
ADD1044_1 (bleu)	18173	56,743	75,962	92,771
ADD1044_2 (vert)	18170	51,636	73,858	90,869

Figure 119: Size distribution of the Cu powder

Density analysis

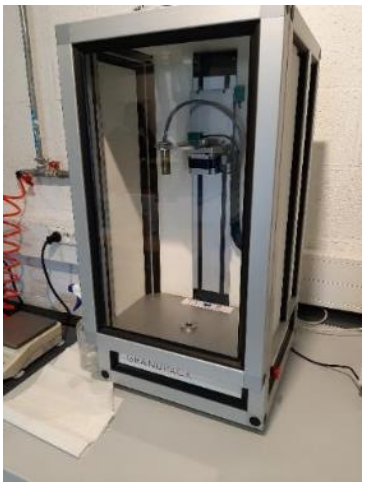

Figure 120: High resolution tapped density analyzer (Granupack)

Table 12: Results obtained with density analyzer Granupack

Sample	ρ[◦]	ρ[n]	n½	H[n]	C[n]	ρ[∞]	τ
ADD1044_200513	3,669	4,162	26,9	1,134	11,8	4,356	42,8
ADD1044_200513_2	3,645	4,171	27,2	1,144	12,6	4,385	46,9
ADD1044_200513_3	3,618	4,177	26,6	1,155	13,4	4,405	47

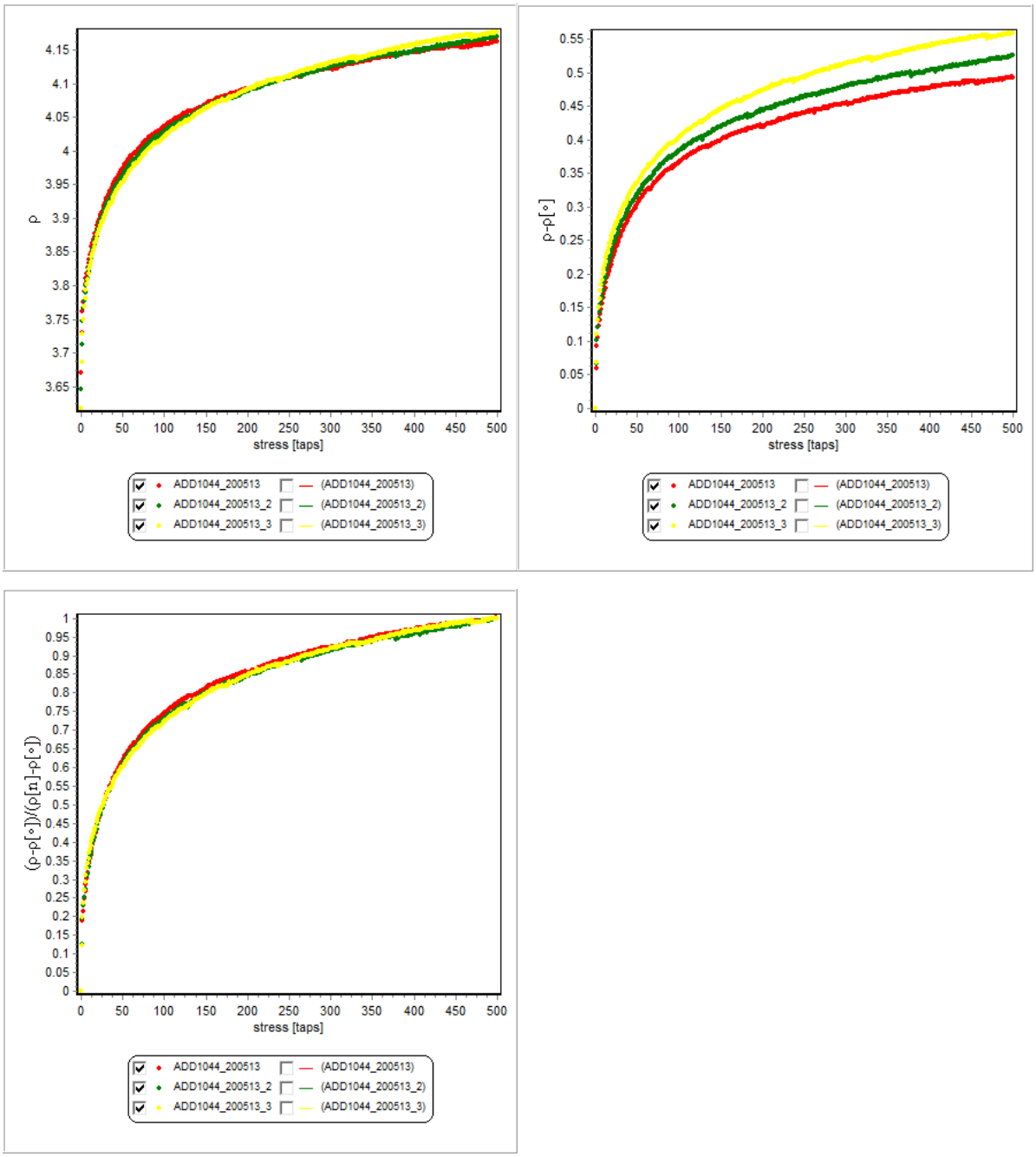

Figure 121: Results obtained with density analyzer Granupack

Hall flowability

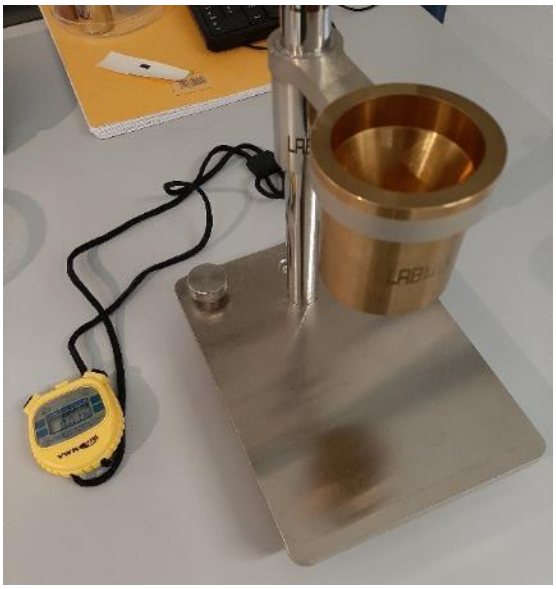

Figure 122: Hall flowmeter

Table 13: Results obtained with the Hall flowmeter

Funnel Type	Mass 1	Time 1	Mass 2	Time 2	Mass 3	Time 3
Diameter 2,5	50,6g	20s	50,5	20s	50,5	19s
Diameter 6,5	50,5g	1s	50,5	1s	50,5	1s

Chemical analysis

Phosphorus and oxygen are very detrimental to conductivity in the material. ICP analysis of the powder was performed (see Table 14).

Table 14: Results of the ICP analysis

	SIRRIS_Cu
P	0.001
N	< 0.001
O	0.188

Conclusion

The powder showed good flowability but a lot of fine particles are present. This large number of satellites is very visible on the SEM pictures of the powder (Figure 123).

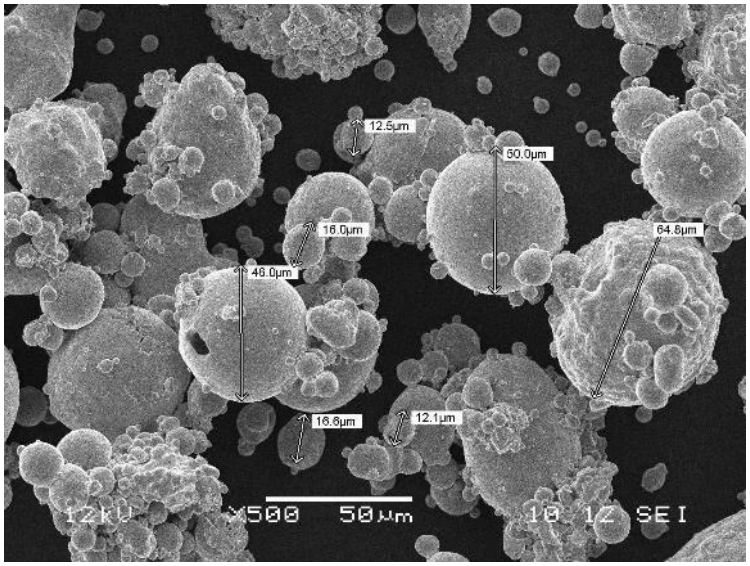

Figure 123: SEM investigation of the Cu powder

Design of experiment

First trials

The first trials aimed at testing the pre-sintering conditions of the powder and a starting point for a design of experiment. The strategy was to use Arcam parameters and a higher presintering temperature to increase the window of stability (Figure 124). Getting the process window right is important to avoid failure of the job. Exploring several process conditions per job is possible provided that none of them induce failure of the manufacturing job. Figure 125 illustrates how swelling will damage the rake and stop the manufacturing. Several attempts were needed before a design of experiment with no swelling was obtained.

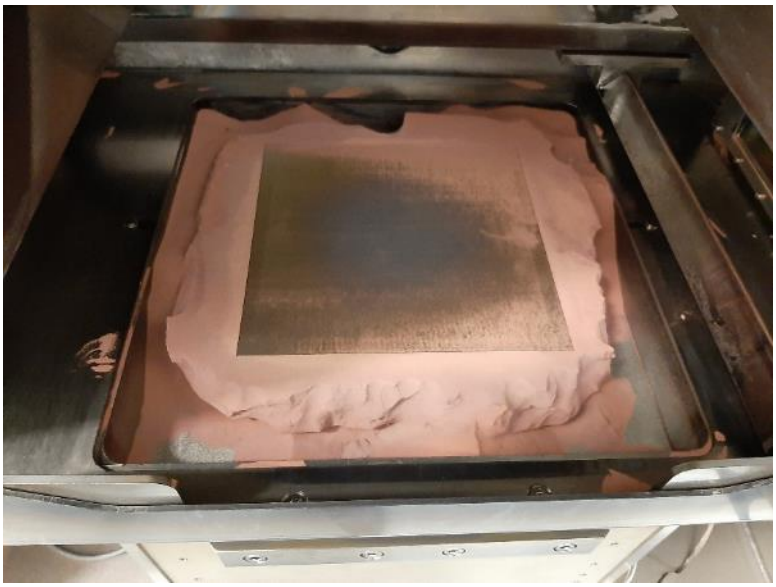

Figure 124: Testing the pre-sintering conditions: powder cake around the build plate

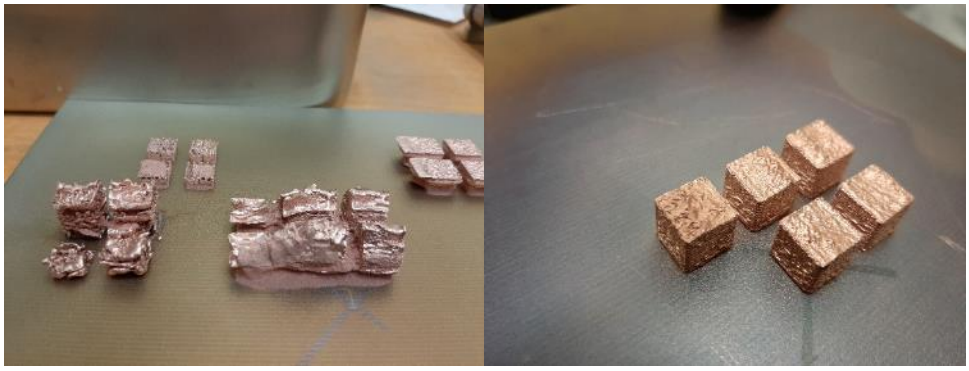

Figure 125: Swelling problem (left) and part without swelling (right)

Final design of experiment:

Table 15: DOE parameter variations

	I_beam [mA]	V_beam [mm/s]	I_Focus [mA]	d_line [mm]	Epaisseur de couche [µm]	T preheat [°C]	densité relative [%]
Plan factoriel complet							
1	8	4000	20	0,1	50	530	[/]
2	16	2500	20	0,1	50	530	[/]
3	16	2500	10	0,1	50	530	95,545
4	16	4000	20	0,1	50	530	[/]
5	16	4000	10	0,1	50	530	91,414
6	8	2500	10	0,1	50	530	92,183
7	8	4000	10	0,1	50	530	94,140
8	8	2500	20	0,1	50	530	[/]
9	12	3250	15	0,1	50	530	93,16
10	14	2875	12,5	0,1	50	530	[/]
Plan de de doehlert 1							
1	11	3289	13,3	0,1	50	440	93,485
2	14	2423	13,3	0,1	50	440	90,968
3	11	2134	10	0,1	50	440	92,343
4	17	3289	13,3	0,1	50	440	91,221
5	17	3866	10	0,1	50	440	90,771
6	11	2711	6,7	0,1	50	440	90,570
7	17	2134	10	0,1	50	440	93,162
8	11	3866	10	0,1	50	440	92,807
9	14	3000	10	0,1	50	440	90,628
10	14	3577	6,7	0,1	50	440	91,923
11	8	3000	10	0,1	50	440	92,990
12	17	2711	6,7	0,1	50	440	94,481
13	20	3000	10	0,1	50	440	90,444
14	14	3000	10	0,1	50	440	90,644
Plan de de doehlert 2							
1	13	2500	5,5	0,1	50	440	93,688
2	14,3	2067	5,5	0,1	50	440	93,428
3	14,3	2356	3,5	0,1	50	440	93,725
4	18	2500	5,5	0,1	50	440	94,178
5	16,8	2067	5,5	0,1	50	440	92,454
6	16,8	2356	3,5	0,1	50	440	94,236
7	16,8	2933	5,5	0,1	50	440	93,946
8	14,3	2933	5,5	0,1	50	440	93,085
9	15,5	2789	3,5	0,1	50	440	94,013
10	16,8	2644	7,5	0,1	50	440	94,090
11	14,3	2644	7,5	0,1	50	440	94,417
12	15,5	2211	7,5	0,1	50	440	93,619
13	15,5	2500	5,5	0,1	50	440	94,200
14	15,5	2500	5,5	0,1	50	440	93,904
Analyse contour (ATTENTION : Problème durant l'impression)							
1	16	2500	10	0,1	50	440	91,560
2	16	2500	10	0,1	50	440	91,310
3	16	2500	10	0,1	50	440	93,250
4	16	2500	10	0,1	50	440	92,900
5	16	2500	10	0,1	50	440	92,580
6	16	2500	10	0,1	50	440	[/]
7	16	2500	10	0,1	50	440	[/]

Trials done at 530°C pre-heating temperature were very hard to stabilize in the machine. The reason is unclear, but the results show optimal density (Figure 126). The next set of trials was done at 440°C and also gave good results (Figure 127). The data is very good in a large range of parameter sets.

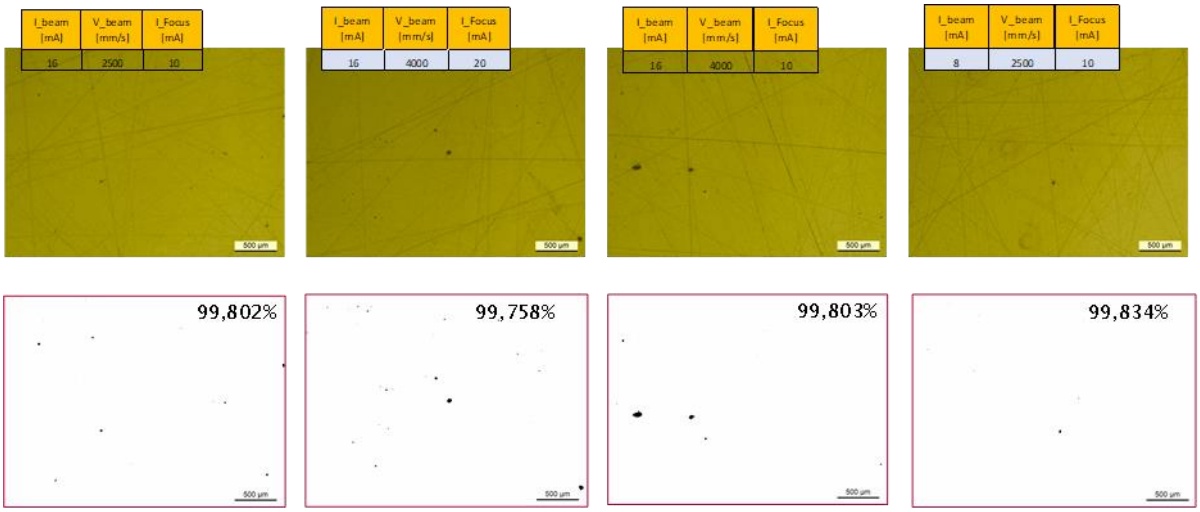

Figure 126: Cross sections of parts built with 530°C pre-heating temperature and corresponding image analysis

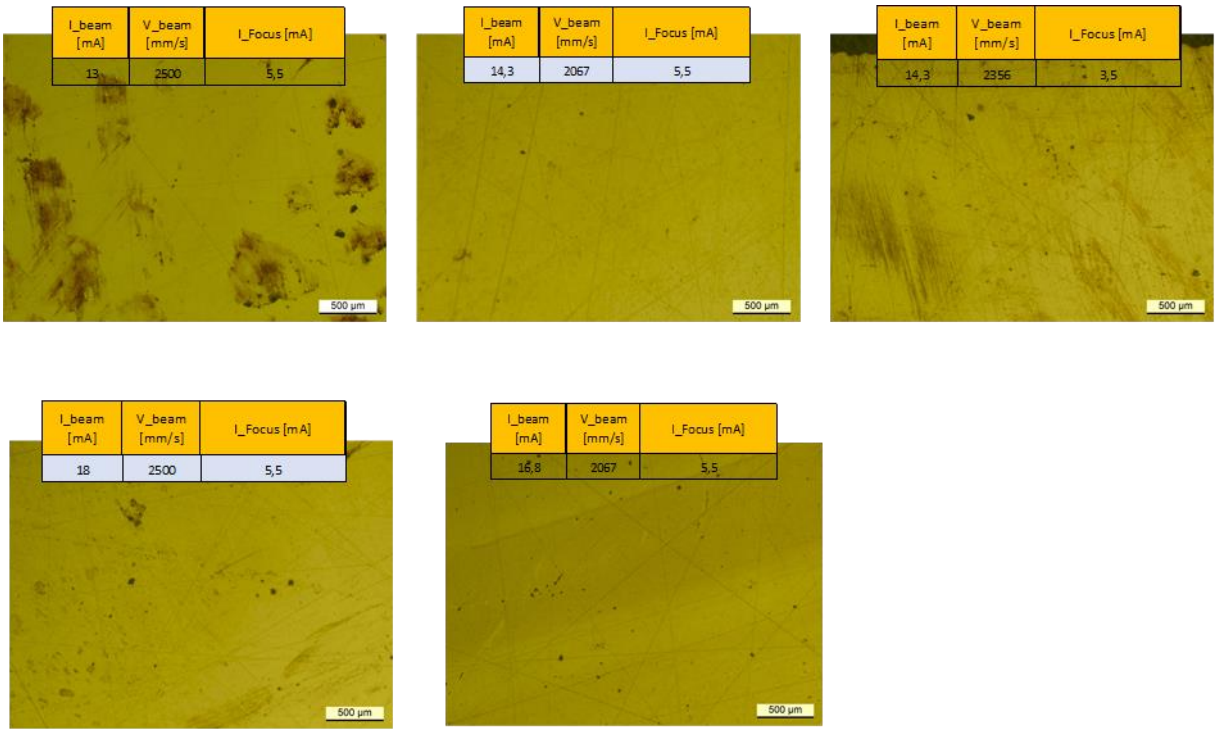

Figure 127: Cross sections of parts built with 440°C pre-heating temperature

Copper demonstrator

The copper demonstrator is a copper winding from an electric motor (Figure 128a). It will serve as an example to show the potential of the technology.

Manufacturing this demonstrator required:

- Developing the cooling strategy to maintain the part close to the target preheat temperature.
- Developing the supporting strategy specific to copper. The material has a very low mechanical resistance and supports are traditionally weaker (less dense).

Several attempts were needed to get the correct supporting dense structure that avoids overheating and swelling that would lead to job failure (Figure 128b - c).

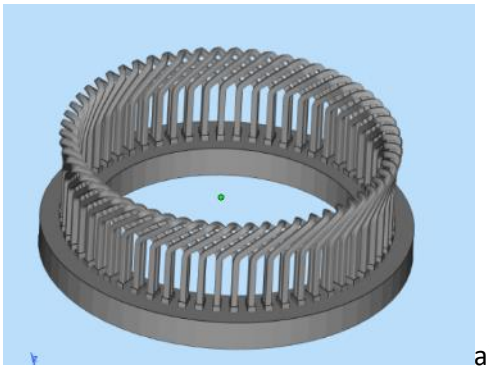
a)
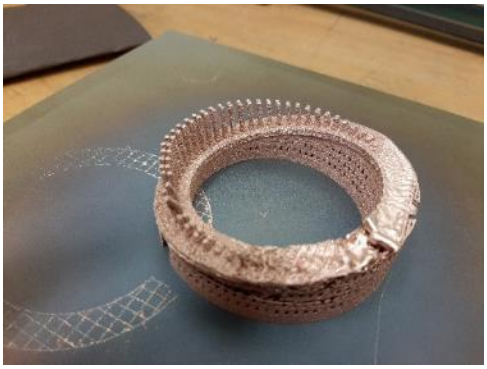
b)
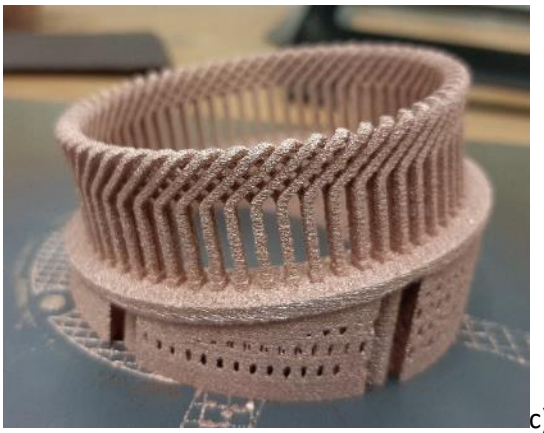
c)

Figure 128: a) geometry of the copper winding b) build fail c) part correctly built

3.1.6 WP5 Dissemination activities

For the performed activities, see Chapter 5 - Dissemination plan.

4 Economic importance of the research topic and of the results for small and medium-sized enterprises (SME)

See also attachment on the results estimation (Ergebniseinschätzung).

Concerning the coating of CuNiSiCr / CuCuCr + Cr/Nb coating: the PVD coating of the alloy powder should additionally increase the Cr/Nb content in the material to be processed. It is very difficult or impossible to produce such alloys homogeneously from insoluble or minimally soluble systems by melting metallurgy. In general, the alloys selected in the project are age-hardenable and should achieve a high hardness with simultaneously high electrical/thermal conductivity through a fine distribution of the insoluble alloying elements. However, according to the evaluation of the results, the achieved properties in the parts produced with treated powders are not superior to those obtained with commercial ones. This is due to the high oxygen content contained in the coated powders, which compromises the physical properties.

The cost of the coating plays an important role in the economic viability of these alloy powders. The increased processability of the coated CuCrZr and CuNiSiCr powders is not sufficient to justify the costly PVD treatment, because such alloys can already be processed with commercial LBM equipment. The formation of finely distributed oxides in the microstructure is however reminiscent of ODS (oxide dispersion strengthened) alloys, which are suitable for high-temperature applications (due to their high creep resistance). The further development of this approach will be pursued in a follow-up project.

On the other hand, the coating of pure Cu with W provided and increased energy absorption and allowed to process the material at a lower laser power (<380 W), while it would normally require a LBM system with a 1000 W laser to obtain 99% density. Such LBM systems have however a larger laser spot (e.g. 70-100 µm) and are not able to build fine and detailed structures like the one manufactured in this project. Pure Cu (due to its instability during LBM processing) is at the moment not industrially widespread as a material for additive manufacturing, and in this respect the cost of the PVD treatment can be justified by the increased processability of the material, and therefore is an interesting innovation for the interested companies.

The results obtained with aluminium open the door to use non weldable aluminium alloys traditionally used as structural elements by a simple coating of the powder. The additional element added will be in small quantities and not fundamentally change the metallurgy of the base alloy.

This means that the alloy can be produced by traditional well established means and tuned later for AM application. Introducing flexibility in the manufacturing chain. Several applications in space and aerostructural parts are possible. This also opens possibilities for recycling existing grades and upscaling the value in a simple way. A patent is under construction based on the detailed results shown in this report.

5 Dissemination plan

5.1 Performed dissemination during the course of the project

Action	Goal	Place / Frame	Date(s)
Project meetings with the SME user committee and the research partners (DE)	Progress report, input from industry, discussion and decisions	fem, Schwäbisch. Gmünd (online).	10.09.2019 16.09.2020 04.05.2021 11.11.2021 17.02.2022
Project presentations at seminars/workshops	Information for industry and public	Online/Ressourcen-effizienzzentrum Bayern (REZ)	29.10.2020 17.03.2021
Project website	Short presentation of the project (goals, structure, partner)	https://www.fem-online.de/en/content/ponamp-project	since September 2019
Presentation at the feminar (internal seminar) at fem	Report on the research project and its results, public discussion	Internal seminar at fem	20.10.2021
User Committee in Wallonia, (BE)	- Presentation of Belgian and German results on Cu and Al powders for Additive Manufacturing - 12 people present including Diarotech, FNH, Euro Heat Pipes, Hoganas, Sonaca and Thales (6 industrialists) - Presentation of the new "MagnetAM" project (Sirris, Cenaero) - Strong interest in the Ponamp results for FNH and EHP. Very excited comments from Mr Skevée (FNH) ("never seen these results on Al powder"). - Preparation of a demonstrator at the request of the consortium - Investigation for patent registration (valorization of Ponamp results)	Videoconference by Materia Nova – Sirris and Umons to wallon partners	26.11.2021

5.2 Dissemination after the project ending

Action	Goal	Place / Frame	Date(s)
Presentation at the Mitgliederversammlung of the fem	Progress report, input from companies, discussion	Mitgliederver-sammlung des **fem**	Annual, 2022
Presentation at the feminar (internal seminar) at fem	Report on the research project and its results, public discussion	Internal seminar at fem	2022/2023
Publication of partial results in the form of annual reports, press releases, lectures etc.	Make industry aware of the project and research results as early as possible.	Internet presence and annual reports of the research institutes	Annual, from 2022
Publication of the final report	Compilation of research results and documentation of material parameters	Internet presence and annual reports of the research institutes	2022
Presentation at scientific conferences	Presentation of results, information, discussion	e.g.: Kupfersymposium	2022/2023
Internet publication of the results	Publication of a summary of the main results	Internet presence and annual reports of the research institutes	2022
Services	Bilateral projects with SMEs		from 2022
Presentation of partial results within the framework of public seminars	Discussion of individual partial results from the WPs with representatives from industry and research	Final Meeting (online) – fem Schwäbisch Gmünd	2022
Publication in journal, e.g.: „Materials Science and Technology“	Publication of results in technical journals	Scientific publication	2022/2023
Final User Committee (Wallonia, BE)	- Presentation of Belgian and German results on Cu and Al powders for Additive Manufacturing - planned participations: Diarotech, FNH, Euro Heat Pipes, Hoganas, Sonaca and Thales - Presentation of final Belgian and German results on Cu and Al powders for Additive Manufacturing.	Videoconference and face-to-face by Materia Nova – Sirris and Umons to wallon partners	15.09.2022

5.3 Estimation on the feasibility of the proposed and updated dissemination plan

The dissemination plan was updated and deviates very little from the planned one. The dissemination activities are realistic. The intended measures during the project course are concluded, and the ones after the project ending have been either already partially performed or they will be shortly.

6 Use of funding

6.1 Necessity and adequacy of the performed work

The work carried out at the research institutes was delayed by the Corona pandemic, when compared to the reviewed and approved application. In order for the research project to be completed in accordance with the proposal, an extension of the duration of the project by six months (until 28.02.2022) for both German research institutes (fem and UMSICHT) was applied for and approved (original end of the project duration on 31.08.2021). A similar project prolongation was applied for by Materia Nova, Uni Mons and Sirris in Belgium and also approved. All the conducted activities were necessary and appropriate to achieve the goals of the research.

6.2 Proposed and used person months

fem person months:

Monat	1	2	3	4	5	6	7	8	9	10	11	12	13	14	15	16	17	18	19	20	21	22	23	24	25	26	27	28	Summe
SOLL																													
HPA_A	0,15	0,15	0,15	0,15	0,45	0,45	0,45	0,45	0,3	0,3	0,3	0,3	0,3	0,3	0,3	0,3	0,3	0,3	0,3	0,3	0,3	0,3	0,3	0,3	0	0	0	0	7,2 MM
HPA_B	0,75	0,75	0,75	0,75	0,6	0,6	0,6	0,6	0,6	0,64	0,7	0,7	0,7	0,7	0,7	0,7	0,45	0,45	0,45	0,45	0,45	0,45	0,45	0,41	0	0	0	0	14,4 MM
Monat	1	2	3	4	5	6	7	8	9	10	11	12	13	14	15	16	17	18	19	20	21	22	23	24	25	26	27	28	Summe
IST																													
HPA_A	0,15	0,15	0,15	0,15	0,45	0,45	0,45	0,45	0,3	0,3	0,3	0,3	0,3	0,3	0,3	0,3	0,3	0,3	0,3	0,3	0,3	0,3	0,3	0,3	0	0	0	0	7,2 MM
HPA_B	0,75	0,75	0,75	0,75	0,6	0,6	0,6	0,6	0,6	0,64	0,7	0,7	0,7	0,7	0,7	0,7	0,45	0,45	0,41	0,25	0,25	0,25	0,25	0,25	0,25	0,25	0,25	0,25	14,4 MM

Fraunhofer UMSICHT person months:

Monat	1	2	3	4	5	6	7	8	9	10	11	12	13	14	15	16	17	18	19	20	21	22	23	24	25	26	27	28	29	30	Summe
SOLL																															
HPA_A	0,7	0,7	0,8	0,9	0,9	1,0	0,8	0,8	0,85	0,8	0,95	1,2	0,9	0,85	0,9	0,8	0,9	1,0	1,0	0,8	0,85	0,96	1,0	1,0	0	0	0	0	0	0	21,36 MM
HPA_B	-	-	-	-	-	-	-	-	-	-	-	-	-	-	-	-	-	-	-	-	-	-	-	-	-	-	-	-	-	-	0 MM
Monat	1	2	3	4	5	6	7	8	9	10	11	12	13	14	15	16	17	18	19	20	21	22	23	24	25	26	27	28	29	30	Summe
IST																															
HPA_A	0,61	1,20	1,45	0,29	0,7	0,62	0,8	1,02	0,99	0,86	0,65	0,22	0,82	0,79	0,99	0,57	0,43	0,65	0,50	0,52	0,36	0,21	0,69	0,66	0,66	0,70	0,82	1,12	0,72	0,94	21,56 MM
HPA_B	-	-	-	-	-	-	-	-	-	-	-	-	-	-	-	-	-	-	-	-	-	-	-	-	-	-	-	-	-	-	0 MM

7 Funding notes and acknowledgments

This work was funded by the public service of Wallonia and by the German Federal Ministry for Economic Affairs and Climate Action based on a decision of the German Bundestag via the AiF-IGF Program, as part of transnational CORNET overall project (No 250 EN). The industrial project partners are acknowledged in particular for their support: KME GmbH and SCHMELZMETALL Deutschland GmbH for providing materials, Reischauer GmbH for processing said materials, Unicorn Engineering GmbH for providing designs, and ECKA Granules Germany GmbH (Kymera International), Arnd Sauter GmbH, BMW Group, Trovus Tech GmbH and Indutherm Gießtechnologie GmbH for their advice and input on the project activities.

8 References

[1] Wohlers Report 2018, Wohlers Associates, Inc, Fort Collins, Colorado, USA, 2018
[2] EUROSTAT, Manufacturing statistics – NACE Rev. 2, data extract from May 2018, (https://ec.europa.eu/eurostat/statistics-explained/index.php), 30.8.2018
[3] J. Gausemeier, …, Thinking ahead the Future of Additive Manufacturing, Heinz Nixdorf Institut, Univ. Paderborn, 2013
[4] Kempen K., Expanding the materials palette for Selective Laser Melting of metals, KU Leuven Arenberg Doctoral School, Faculty of Engineering Science, March 2015
[5] http://www.esabna.com/us/en/education/blog/how-to-avoid-cracking-in-aluminium-alloys.cfm
[6] Herzog D., Seyda V., Wycisk E., Emmelmann C., Additive manufacturing of metals, Acta Materialia 117 (2016), 371-392
[7] Mauduit A., Pillot S., Gransac H., Study of the suitability of aluminium alloys for additive manufacturing by laser powder-bed fusion, U.P.B. Sci. Bull., Series B, Vol. 79, Iss. 4, 2017
[8] Martin J.H., Yahata B.D, Hundley J.M., Mayer J.A., Schaedler T.A., Pollock T.M., 3D printing of high-strength aluminium alloys, Nature, vol 549, 21 September 2017
[9] Skalicky P., Koutny D., Pantelejev L., Palousek D., Processing of Aluminium Alloy EN AW 7075 Using Selective Laser Melting: Initial Study, 58th ICMD 2017, 6 - 8 September 2017, Prague, Czech Republic
[10] Herzog D., Seyda V., Wycisk E., Emmelmann C., Additive manufacturing of metals, Acta Materialia 117 (2016), 371-392
[11] Mauduit A., Pillot S., Gransac H., Study of the suitability of aluminium alloys for additive manufacturing by laser powder-bed fusion, U.P.B. Sci. Bull., Series B, Vol. 79, Iss. 4, 2017
[12] Becker, David, „Selektives Laserschmelzen von Kupfer und Kupferlegierungen“, Dissertation, RWTH Aachen, Apprimus Verlag, Aachen, 1. Auflage (2014)
[13] Ikeshoji, T.-T., Nakamura, K., Yonehara, M., Imai, K., Kyogoku, H.. „Selective Laser Melting of Pure Copper“, (2018) JOM, 70 (3), pp. 396-400
[14] Becker D., Wissenbach K., „Additive manufacturing of copper components” (2017) www.ilt.fraunhofer.de
[15] Matthias A.Lodes, Raf Guschlbauer, CarolinKörner, Process development for the manufacturing of 99.94% pure copper via selective electron beam melting, Materials Letters143 (2015) 298–301
[16] Mahale, Tushar Ramkrishna, Electron Beam Melting of Advanced Materials and Structures, mass customization, mass personalization, Phd dissertation, 2009-12-04, North Carolina State University
[17] D.A. Ramirez, L.E. Murr, S.J. Li , Y.X. Tian , E. Martinez, J.L. Martinez, B.I. Machado, S.M. Gaytan, F. Medina , R.B. Wicker , Open-cellular copper structures fabricated by additive manufacturing using electron beam melting, Materials Science and Engineering: A, Volume 528, Issues 16–17, 25 June 2011, Pages 5379-5386
[18] D.A. Ramirez, L.E. Murr , E. Martinez, D.H. Hernandez, J.L. Martinez, B.I. Machado, F. Medina, P. Frigola, R.B. Wicker, Novel precipitate–microstructural architecture developed in the fabrication of solid copper components by additive manufacturing using electron beam melting, Acta Materialia, Volume 59, Issue 10, June 2011, Pages 4088-4099
[19] Lassner, Erik, Wolf-Dieter Schubert. "The element tungsten." Tungsten. Springer Us, 1999. 1-59.

[20] WHS Sondermetalle, Wolfram-Kupfer - https://www.whs-sondermetalle.de/images/pdf/WCu_Wolfram-Kupfer_web.pdf
[21] Plansee SE, Elektrische Kontakte W-Cu https://www.plansee.com/de/produkte/komponenten/elektrische-kontakte.html
[22] Plansee SE, Elektrische Kontakte Cu-Cr https://www.plansee.com/de/produkte/komponenten/elektrische-kontakte/kupfer-chrom-cucr.html
[23] Botcharova, E., et al. Novel Cu–Nb-wires: Materials Science and Engineering: A 416 (2006) 261-268.
[24] Hangen, U.; Raabe, D. Acta metallurgica et materialia 43 (1995) 4075-4082.
[25] Botcharova, E.; Freudenberger, J.; Schultz, L. Journal of alloys and compounds 365 (2004) 157-163.
[26] Alphysica, Produkte http://www.alphysica.com/index.php/cu-nb.html
[27] IFW Dresden, Institute for metallic materials http://www.ifw-dresden.de/institutes/imw/research/metal-physics/ultra-strong-conductors-for-pulsed-high-field-magnets/cu-nb-alloys/
[28] S. Szemkus et al, Laser additive manufacturing of contact materials, Journal of Materials Processing Tech. 252 (2018) 612–617
[29] Dai, D., Gu, D., 2014. Thermal behavior and densification mechanism during selective laser melting of copper matrix composites: simulation and experiments. Mater. Des. 55, 482–491
[30] Li. R et. al. Selective laser melting W–10 wt.% Cu composite powders, Int J Adv Manuf Technol (2010) 48, 597–605
[31] Gu, D.D., Shen, Y., 2009a. Effects of processing parameters on consolidation and microstructure of W–Cu components by DMLS. J. Alloys Compd. 473, 107–115.
[32] X.L. Jiang, M. Boulos, Induction plasma spheroidization of tungsten and molybdenum powders, Transact. Nonferro. Metals Soc. China (English Edition) 16 (2006) 13–17
[33] Li.R et. al., Fabrication of fine-grained spherical tungsten powder by radio frequency (RF) inductively coupled plasma spheroidization combined with jet milling, Advanced Powder Technology 28 (2017) 3158–3163
[34] Lin-zhi Wang et al. , Properties evolution of additive manufacture used tungsten powders prepared by radio frequency induction plasma, International Journal of Refractory Metals & Hard Materials 67 (2017) 90–97
[35] B. Li, Z. Sun, H. Jin, P. Hu, F. Yuan, Fabrication of homogeneous tungsten porous matrix using spherical tungsten powders prepared by thermal plasma spheroidization process, Int. J. Refract. Meals Hard Mater. 59 (2016) 105–113
[36] CORNET Project OpP3D, 2018, https://www.fem-online.de/en/content/OpP3D
[37] D.V. Sidelev et al. / Surface & Coatings Technology 308 (2016) 168–173)